Development and Characterization of a Regeneratively Amplified Ultrafast Laser System with an All-Glass Stretcher and Compressor

by

Stephen J. Walker

A thesis
presented to the University of Waterloo
in fulfillment of the
thesis requirement for the degree of
Master of Science
in
Physics

Waterloo, Ontario, Canada, 2006

Author's Declaration For Electronic Submission of a Thesis

I hereby declare that I am the sole author of this thesis. This is a true copy of the thesis, including any required final revisions, as accepted by my examiners.

I understand that my thesis may be made electronically available to the public.

Abstract

High-peak power laser systems are defined along with a brief introduction of the technology used in their development and application to the project. A review of concepts surrounding optical pulses, focusing on the particular phenomena involved with the ultrafast, follows. Numerical models involving optical pulses are introduced and verified. An extensive description of the laser system is presented, including models used in its design. Data verifying the correct operation of the laser system is presented and interpreted. A dispersion compensation system, including a functional model, is introduced, and its application to the laser system is analyzed. An introduction to pulse characterization techniques is presented followed by the design and verification of two different characterization devices. Experiments utilizing the dispersion compensation system and pulse characterization devices are presented and the results are interpreted. Conclusions are made regarding the performance of the laser system models and pulse characterization devices, along with suggested improvements for each. The results of the experiments are discussed including suggestions for future work.

Acknowledgements

I would like to acknowledge the assistance of my supervisor, Dr. J. Sanderson, as well as the very helpful explanations about laser systems given to me by Dr. D. Strickland. I would also like to acknowledge Dr. X. Sun for all of his efforts in helping build the laboratory from the ground up and J. B. Macpherson for his helpful discussions about the SPIDER technique.

This thesis would not have been possible if not for the endless support provided by my friends and family. Specifically, I would like to thank Nat for being so rational, Chas for making me laugh and Chantal for keeping me happy.

Table of Contents

List of tables

List of figures

Chapter 1

Introduction

1.1 Background

The production and manipulation of high-peak power pulses of laser light is one of the most enabling technologies developed within the last thirty years. Furthermore the ability to generate ultrafast (generally $< 100fs$ temporal width) pulses with repeatable characteristics has allowed researchers to interact with matter on time-scales similar to those of molecular events such as vibration and dissociation.

The goal of ultrafast laser technology is to produce high-peak powers by containing a large amount of energy in an extremely short period of time.

$$PeakPower = \frac{Energy}{PulseDuration} \tag{1.1}$$

In recent years few-cycle ($< 10fs$) laser pulses, produced through spectral broadening in a hollow fibre [1], have been shown to be ideal tools for investigation of molecular processes [2], [3]. Currently the technology for producing few-cycle laser pulses has allowed for the generation of pulse widths as short as 3.8fs [4].

In general pulse energies of about $100 - 1000\mu J$ and pulse temporal widths of about 25-50 fs have been required to produce few-cycle laser pulses. The required pulses have been, in turn, produced by amplifying broad band low energy (nJ per pulse) seed pulses, produced by a Kerr-lens mode locked (KLM) oscillator, using the chirped pulse amplification (CPA) technique [5].

The damage thresholds of materials making up an amplifier (GW/cm^2) present the greatest limitation to optical pulse amplification. CPA is the most widely used pulse amplification technique because it extends the peak power achievable by an optical amplifier by effectively dealing with the material optical damage thresholds that limit amplification. In a CPA system a seed pulse is stretched in time, or 'chirped', with a dispersive system before amplification takes place, thus reducing the intensity of a pulse inside the amplifier. The amplified chirped pulse is then compressed with a dispersive system capable of reversing the chirp of the pulse.

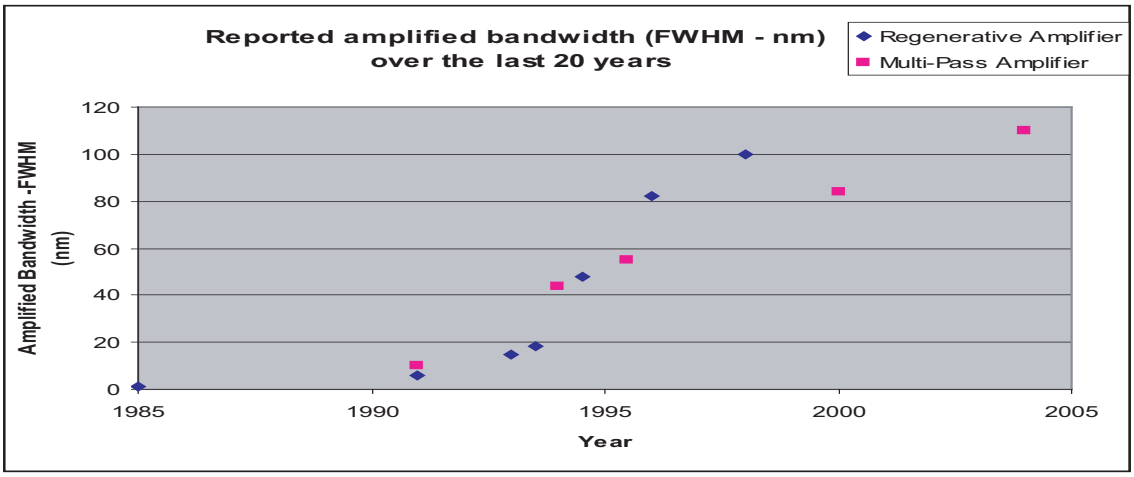

Figure 1.1: Historical single stage amplification bandwidths by amplifier type.

Following the inception of CPA in 1985 a large amount of work went into the development of compact table-top CPA systems capable of producing high peak-powers. Initially the pulse widths produced by CPA systems closely followed the pulse width of the seed pulse. However, as increases in laser technology were made, spurred by the discovery of new lasing material such as Titanium sapphire (Ti:Saph) [6], new limitations were reached.

Today KLM oscillators producing a train of coherent broadband ($> 100nm@800nm$) 10fs pulses at radio frequency repetition rates are commercially available [7]. The spectral bandwidth provided by these oscillator pulses presents a challenge to the design of a CPA system in terms its ability to control chirp and increase energy across the entire bandwidth of the seed pulse.

The last twenty years has seen a steady increase in the amplified bandwidths produced by modest in-lab CPA systems (figure 1.1). Recently, theoretical limitations in the amplified bandwidth capable of being produced in a CPA system have been reached, requiring sophisticated techniques, such as spatially dispersed amplification [8] and spectral filtering [9], to overcome this limit. Consequently these developments have required advances in the technology used by CPA systems to control chirp across a broad bandwidth such as, the introduction of a deformable mirror to control higher order phase [10] and the use of 'chirped' mirrors with designable phase characteristics [11]. In order to aid in compression of the pulses produced by these systems recent developments in pulse characterization techniques such as, spectral phase interferometry for direct electric field reconstruction (SPIDER) [12] and frequency resolved optical gating (FROG) [13], have become essential laboratory tools.

1.2 Project Description

The subject of this thesis is the development and characterization of a regeneratively amplified CPA system capable of producing $< 50fs$, energetic ($> 200\mu J$) laser pulses for the purpose of performing high peak-power laser-matter interaction experiments as well as to serve as the seed pulse for generating few-cycle laser pulses in a hollow fibre system.

The laser system that was built, was developed as an upgrade from a previous kHz repetition rate CPA system producing $> 200fs$ pulses. The goal was to produce $< 50fs$ pulse widths with $> 200\mu J$. To achieve this, a new oscillator system, providing a broad bandwidth ($> 100nm$), to seed the amplification process, was obtained. Next, the amplifier cavity was designed in order that stable amplified pulses could be produced, and with the introduction of spectral filtering techniques, broad amplified bandwidths could be achieved. The employment of dispersion control techniques recently used in; a multi-pass amplifier system to produce 1mJ, 20fs pulses at 1kHz repetition rate [14] and a regenerative amplifier system to produce $8\mu J$, 35fs pulses at 100kHz repetition rate [15], were modeled to determine the feasibility for use in a regenerative amplification system at 1kHz repetition rate.

In order to characterize the pulses produced by the CPA system and aid in compression, two devices were built; an interferometric autocorrelator and SPIDER system, designed with the capability of measuring pulses as short as $5fs$.

In the following chapters, a regeneratively amplified 1kHz repetition rate CPA system without the use of an external stretcher and the capability to produce sufficient band width to give rise to $\sim 16fs$ transform limited pulses, is presented for what is believed to be the first time.

Chapter 2

Review of Concepts

2.1 Theoretical Pulse Description

A pulse of light is defined as a traveling electromagnetic disturbance contained by an amplitude envelope. It is the width of the envelope containing the electromagnetic disturbance that determines whether the pulse is 'fast' or 'slow'. An infinitely slow pulse is described as a continuous wave and has no definable beginning or end (it doesn't look pulse like at all). A continuous wave can be described exactly by it's frequency, ω, and phase, ϕ.

$$\psi = sin(\omega t + \phi) \tag{2.1}$$

An infinitely fast pulse is defined by a delta function and only exists at one point in space a at a given time as shown in equation 2.2.

$$\psi = \delta(x - a) \text{ where } \delta(x - a) = 0 \text{ for } x \neq a \tag{2.2}$$

A Fourier transform (section B.4) of each of these pulses reveals their spectral makeup. The Fourier transform of the continuous wave gives a delta function in frequency space. Similarly the Fourier transform of the fast pulse reveals that a delta function is constructed by an infinitely flat spectrum. This illustrates that in order to produce an electromagnetic pulse a broad spectral bandwidth is absolutely necessary. Consequently, there is a definite relationship for a given pulse shape that exists between the shortest possible temporal width of the pulse and it's spectral bandwidth. For a Gaussian pulse the relationship is:

$$\Delta\tau\Delta\omega = 4ln(2) \tag{2.3}$$

Where $\Delta\tau$ is the full width at half maximum (FWHM)of the temporal envelope of the pulse and $\Delta\omega$ is the FWHM of the spectral envelope of the pulse.

2.1.1 Approximations

To fully describe the vector nature of the electric field that defines a real laser pulse a description of the temporal evolution of the magnitude of the field along three spatial dimensions, $\epsilon(x, y, z, t)$, for each of two field polarizations would be required. For calculations such as the B-integral of the amplifier cavity (see section 2.5.2) a definition of the laser intensity in terms of it's transverse spatial dependencies is necessary [16]. In such cases a simplified formula where the electric field is separable into a transverse distribution $\boldsymbol{F(x,y)}$ and a slowly varying complex amplitude, $\boldsymbol{A(z,t)}$, can be defined:

$$\varepsilon(\mathbf{r}, t) = \frac{1}{2} F(x, y) A(z, t) e^{i(k_0 z - \omega_0 t)} + c.c. \tag{2.4}$$

Often in ultra-fast physics this condition can be relaxed so that only the temporal evolution of the electric field along the direction of propagation for each polarization axis is necessary. This approximation is known as the **scalar approximation** [17]. Linearly polarized light is commonly used allowing for the further simplification of the scalar approximation to a single polarization axis. Generally, descriptions of the pulse in terms of distance along the propagation axis and time can be thought of as equivalent. In what follows, pulse descriptions are given in terms of a time instead of a distance and it is assumed that the reader understands that a plot of the pulse in time is a snapshot of the pulse as it travels from right to left across the page.

2.1.2 Temporal Representation

Under the scalar approximation the field dependence can be written in terms of it's temporal dependence only. Treating the pulse as linearly polarized, which is often the case, the electric field takes the form:

$$\varepsilon(t) = \frac{1}{2} \sqrt{I(t)} e^{i(\omega_0 t - \phi(t))} + c.c. \tag{2.5}$$

Where $\boldsymbol{t}$ is time in the reference frame of the pulse, $\boldsymbol{\omega_0}$ is the central angular frequency of the pulse, $\boldsymbol{I(t)}$ is the time-dependent intensity of the electric field (essentially the complex electric field envelope, discussed below) and $\boldsymbol{\phi(t)}$ is the time-dependent phase of the pulse. It is generally assumed that $\boldsymbol{I(t)}$ and $\boldsymbol{\phi(t)}$ vary much more slowly than the rapidly varying carrier wave $\boldsymbol{e^{i\omega_0 t}}$. Except where necessary for a complete description of the electric field, the carrier wave, complex conjugate (c.c.) and factor of $1/2$ are omitted from descriptions of the electric field as they complicate matters and the important information about the pulse is contained in $\boldsymbol{I(t)}$ and $\boldsymbol{\phi(t)}$ [17]. After these simplifications we can write down the form of the complex amplitude of the electric field:

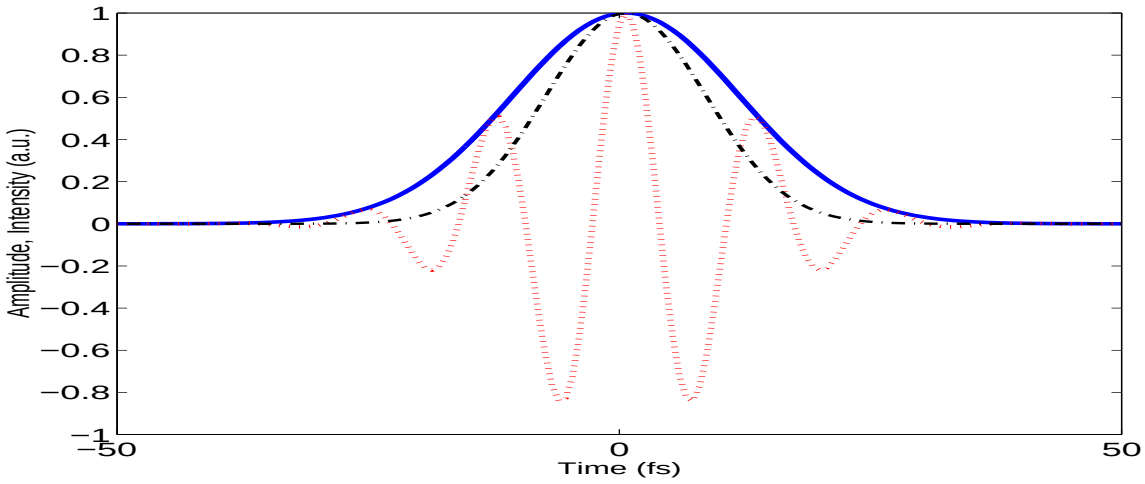

Figure 2.1: The electric field E_t (dotted line), real part of the pulse amplitude $|E_t|$ (solid line) and the pulse Intensity I_t (dash-dot line) of a Gaussian ultra-fast pulse of arbitrary length

$$E_t(t) = |E(t)|e^{-i\phi_t(t)} \tag{2.6}$$

The electric field amplitude can be considered as the envelope that contains the oscillations of the field. The electric field amplitude therefore limits the extent of the pulse in the time domain.

The temporal phase can be expressed as a power series expansion [1] about a central point t_c.

$$\phi_t(t) = \phi_{t0} + \phi_{t1}(t - t_c) + \phi_{t2}(t - t_c)^2 + \dots \tag{2.7}$$

The first term of the temporal phase expansion, ϕ_{t0}, is the absolute temporal phase of the electric field. The absolute phase describes the absolute position of the peaks and valleys of the electric field. The second coefficient, ϕ_{t1}, describes the instantaneous frequency of the electric field while a nonzero third term indicates linear changes in instantaneous frequency across the pulse. Higher order terms in the temporal phase expansion indicate a curvature in the rate of change of instantaneous frequency across the pulse. Higher order terms necessarily indicate a complicated phase profile for the pulse. Pulses that contain only second order changes in their phase have an instantaneous frequency that varies linearly with time.

[1] Note: As with all series expansions agreement can only be expected over a small range near the center of the expansion.

The field amplitude, Intensity and temporal phase are considered real quantities in this field description and have been given the subscript t to distinguish them from the spectral amplitude and phase which will be defined next.

2.1.3 Spectral Representation

An exact pulse description can also be made in the frequency domain (note that ω denotes an angular frequency). Both temporal and spectral descriptions are acceptable for fully describing the electric field of a pulse and transformation between the two domains can easily be performed by application of a Fourier transform. It is often the case, however, that a spectral description of the pulse is easier to work with mathematically when determining the effects of an optical system on a pulse.

The spectral domain analog to equation 2.6 is:

$$E_\omega(\omega) = |E_\omega(\omega)|e^{i\phi_\omega(\omega)} \tag{2.8}$$

Where $|E_\omega|$ is the spectral amplitude with the spectral intensity $|E_\omega|^2 = I_\omega$ being the commonly measured 'power spectrum' retrieved from a spectrometer. The spectral phase is represented by ϕ_ω and describes the phase of each frequency making up the pulse with respect to all other frequencies. The spectral phase is best understood as a power series expansion about a central frequency, ω_0, in analogous fashion to the temporal phase.

$$\phi_\omega(\omega) = \phi_{\omega 0} + \phi_{\omega 1}(\omega - \omega_0) + \phi_{\omega 2}(\omega - \omega_0)^2 + \dots \tag{2.9}$$

where $\phi_{\omega 0}$ represents the absolute spectral phase which describes the phase of the central frequency around which the phase of all other frequencies is relative. The second coefficient, $\phi_{\omega 1}$, represents linear changes in the spectral phase. A nonzero second coefficient indicates a translation of the electric field in time. A non-zero third coefficient of the expansion indicates a curvature in the spectral phase profile. Non-zero values of $\phi_{\omega 2}$ and higher orders ($\phi_{\omega 3}, \phi_{\omega 4}$ etc.) are responsible for longitudinal pulse spreading, also called dispersion.

2.2 Power and Intensity

The instantaneous pulse power (in Watts) is a measure of the energy, per unit time, contained in a pulse. The instantaneous pulse power is derivable from the Poynting theorem [18] and naturally involves an integration over the temporal extent (T) and cross-sectional area (A) of a given pulse.

$$P(t) = \epsilon_0 cn \int_A dS \frac{1}{T} \int_{t-T/2}^{t+T/2} E^2(t')dt' \tag{2.10}$$

where c is the velocity of light in vacuum, n is the index of refraction of the material that the pulse is traveling through, ϵ_0 is the dielectric permittivity.

The pulse intensity, $I(t)$, is a measure of the pulse instantaneous power per unit area. The pulse intensity is of primary concern as it is with high pulse intensities that interesting laser-matter interactions can take place.

2.3 Dispersion

Understanding dispersion is extremely important in the design of a CPA system. The CPA technique involves temporally stretching a mode-locked, but un-energetic oscillator pulse, by passing it through a dispersive system. The energy in the stretched oscillator pulse is subsequently increased in an amplifier system. In the final step the pulse is temporally compressed by reversing all of the accumulated dispersion due to the stretching and amplification stages. The ability to control dispersion is arguably, then, the most important laboratory tool in order to realize a functional CPA system.

2.3.1 Dispersion in Materials

Dispersion is best described as the separation of the frequency components making up a wave due to variations in their velocity. Generally the frequency components making up a wave travel at different velocities when passing through a material. The materials refractive index is a metric used to describe the velocity at which light passes through it. Simplistically this can be written as:

$$v(\omega) = \frac{c}{n(\omega)} \tag{2.11}$$

where $n(\omega)$ is the refractive index of the medium, $v(\omega)$ is the velocity of light in the medium and c is the speed of light in vacuum ($3X10^8 m/s^2$). Generally, the refractive index of a material will vary with frequency, as in figure 2.2. For any non-linear variation in the refractive index with frequency a longitudinal separation of adjacent frequencies will occur as they are made to travel different optical path lengths through the medium. Indeed, even air has a slightly curved index of refraction profile causing pulses of light to stretch longitudinally while passing through it.

Generally, spectral phase is used to determine a materials contribution to system dispersion. The spectral phase gained by each frequency passing through a medium is a function of the refractive index of the medium.

$$\phi(\omega) = \frac{2\pi n(\omega) l}{\lambda} \tag{2.12}$$

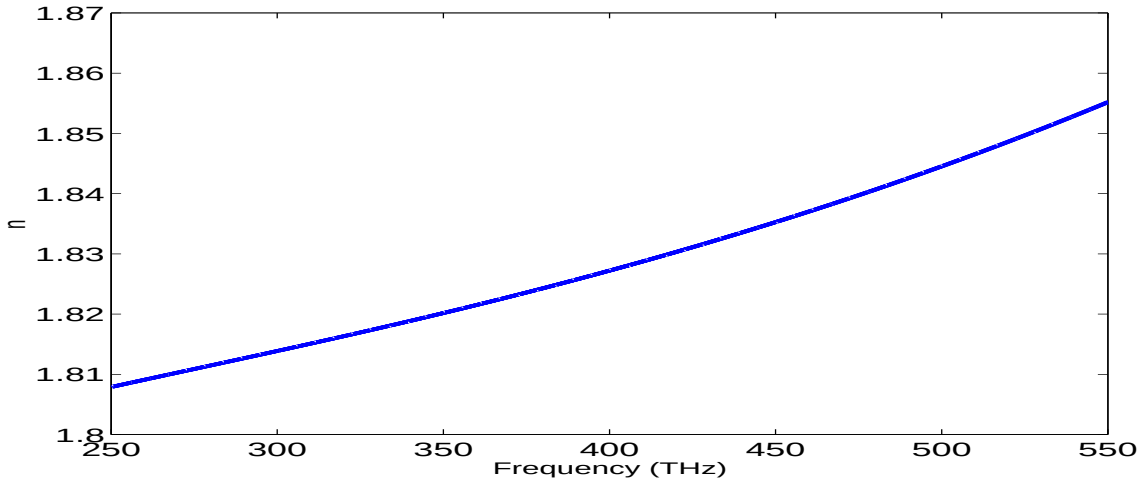

Figure 2.2: Refractive index against frequency for SF57. The strong curvature of it's refractive index with frequency indicates that it is a very dispersive glass

Empirical fits to experimentally measured refractive indices can be used to ensure accurate representation. The phase change experienced by each colour in a pulse passing through any number of materials in an optical system can be determined by a linear summation of the phase changes due to each element in the system.

An alternative to representing the spectral phase in empirical form is to expand the phase in a Taylor series about the central frequency ω_0, similarly to equation 2.9

$$\phi(\omega) = \phi(\omega_0) + \phi'(\omega_0)(\omega - \omega_0) + \frac{1}{2}\phi''(\omega_0)(\omega - \omega_0)^2 + \frac{1}{6}\phi'''(\omega_0)(\omega - \omega_0)^3 + \dots \tag{2.13}$$

Just as in equation 2.9 $\boldsymbol{\phi(\omega_0)}$ is known as the absolute phase and describes the exact phase of the central frequency. When considering dispersion $\boldsymbol{\phi'(\omega_0)}$ is known as the Group Velocity and is the first derivative of the spectral phase with respect to frequency evaluated at the central frequency $\boldsymbol{\omega_0}$. Non-zero values of the Group Velocity describe a linear translation of the pulse in time. The Group Velocity Dispersion (GVD) is represented by $\boldsymbol{\phi''(\omega_0)}$ and is the second derivative of the phase with respect to frequency evaluated at the central frequency. Non-zero GVD values give a parabolic phase profile and are responsible for most of the temporal widening experienced by pulses. Higher orders of dispersion are labeled as: Third Order Dispersion (TOD) - $\boldsymbol{\phi'''(\omega_0)}$, Fourth Order Dispersion (FOD) - $\boldsymbol{\phi''''(\omega_0)}$ and so on ...

Dispersion terms above GVD have a decreasing effect on the shape of a pulse. Generally it is accepted that only GVD and TOD need to be controlled to obtain pulses as short as 150 fs and no more than fourth order need be controlled to obtain

pulses as short as 30 fs.

Reference [19] gives equations for GVD, TOD and FOD due to material dispersion as a function of wavelength.

$$GVD = \frac{d^2\phi_m(\omega)}{d\omega^2} = \frac{\lambda^3 L_m}{2\pi c^2}\frac{d^2 n(\lambda)}{d\lambda^2} \tag{2.14}$$

$$TOD = \frac{d^3\phi_m(\omega)}{d\omega^3} = \frac{\lambda^4 L_m}{4\pi^2 c^3}(3\frac{d^2 n(\lambda)}{d\lambda^2} + \frac{\lambda d^3 n(\lambda)}{d\lambda^3}) \tag{2.15}$$

$$FOD = \frac{d^4\phi_m(\omega)}{d\omega^4} = \frac{\lambda^5 L_m}{8\pi^3 c^4}(12\frac{d^2 n(\lambda)}{d\lambda^2} + 8\lambda\frac{\lambda d^3 n(\lambda)}{d\lambda^3} + \lambda^2\frac{d^4 n(\lambda)}{d\lambda^4}) \tag{2.16}$$

It is convenient to describe the dispersion of an optical system in terms of it's GVD against wavelength. This can be done using equation 2.14 if the index of refraction component in question is known. If the index of refraction is not known a Taylor expansion of the GVD about the central wavelength can be performed as in equation 2.17.

$$GVD(\lambda) = GVD(\lambda_0) + 2\pi c TOD(\lambda_0)(\frac{1}{\lambda} - \frac{1}{\lambda_0}) + 4\pi^2 c^2 FOD(\lambda_0)(\frac{1}{\lambda} - \frac{1}{\lambda_0}) + \dots \tag{2.17}$$

2.3.2 Dispersion from a Prism Pair

Net higher order dispersion can be achieved by taking advantage of the refractive properties of a prism. Fork et al. describe the generation of a net negative GVD [20] using a prism pair arrangement. Further work by Sherriff [21] expanded the calculation by Fork to an arbitrary prism sequence.

In general the GVD produced by a prism pair sequence can be derived from the total optical path length (P) between them:

$$GVD = \frac{d^2\phi_m(\omega)}{d\omega^2} = \frac{\lambda^3}{2\pi c^2}\frac{d^2 P(\lambda)}{d\lambda^2} \tag{2.18}$$

A more intricate formulation giving the dispersion of a double prism pair compressor system, including the positive dispersion due to the prism material, is presented in section .

2.3.3 Dispersion from a Dielectric Stack

Dispersion from a dielectric stack is realized by producing a multi-layered structure with varying refractive index and/or layer thickness [22]. Simply put, chirped

mirrors introduce a frequency dependent group-delay by reflecting incident radiation at different positions within the multi-layer structure. New design techniques [11], have allowed for the development of nearly constant group velocity dispersion over a spectral range of 150THz (650-950nm) as well as large amounts of TOD and FOD dispersion over a bandwidth of 50THz (740-840nm).

2.4 Coherence

In general laser light has a high degree of coherence. In other words the waves making up a pulse of laser light will maintain their phase relationship well while propagating through space. Because of coherence the high degree of dispersion control required to produce ultrafast pulses is achievable within each laser shot.

2.5 Polarization and Non-Linear Processes

Every atom or molecule contains protons and electrons which feel the influence of electrical and magnetic fields. Any observable light induced effects are generally considered to be due to the influence of a propagating light wave on the electron cloud.

The reaction of a material to a light field is described by the material polarization. Quantification of the material polarization becomes important when the electrons in a material are shifted by such an amount from their original positions that the fundamental properties of the material are significantly altered. Such an effect forms the basis for all of non-linear optics.

The material polarization is best described as a power series of the proper description of the electric field (equation 2.5).

$$P = \epsilon_0(\chi^{(1)}\varepsilon + \chi^{(2)}\varepsilon^2 + \chi^{(3)}\varepsilon^3 + ...) \tag{2.19}$$

where ϵ_0 is the vacuum permittivity and $\chi^{(n)}$ is the n-th order component of the electric susceptibility of the medium. Together both variables give a description of the ability of the material to hold on to it's electrons.

2.5.1 Second Harmonic Generation

Truncating equation 2.19 to two terms gives the polarization as a function of the incident electric field and the electric field squared.

$$P = \epsilon_0\chi^{(1)}\varepsilon + \epsilon_0\chi^{(2)}\varepsilon^2 \tag{2.20}$$

Taking a closer look at the $\boldsymbol{\varepsilon^2}$ term using the definition presented in equation 2.5 gives:

$$\varepsilon^2(t) = \frac{1}{4}E^2(t)e^{2i\omega_0 t} + \frac{1}{2}E(t)E^*(t) + \frac{1}{4}E^{*2}(t)e^{-2i\omega_0 t} \tag{2.21}$$

This expression includes terms that oscillate at $\boldsymbol{2\omega_0}$ which is the second harmonic of the fundamental, $\boldsymbol{\omega_0}$. The remaining terms that oscillate at $\boldsymbol{2\omega_0}$ depend on the square of the electric field and above. The magnitude of the second harmonic signal is therefore proportional to the I^2 of the incident radiation.

Negative uni-axial crystals have a non-negligible $\boldsymbol{\chi^{(2)}}$ and are widely used to produce SHG. SHG is used quite frequently to obtain a measurement of the temporal pulse width of an ultrafast pulse (see section 6.4.2).

Phase Matching

To produce efficient SHG, or sum frequency generation, the phase matching condition must be observed. Phase matching is achieved when the wave vectors of the incident radiations satisfies the condition, for type-I SHG:

$$2k_\omega = k_{2\omega} \tag{2.22}$$

and for type-II SHG:

$$k_o(\omega) + k_e(\omega, \theta_m) = k_e(2\omega, \theta_m) \tag{2.23}$$

Where k is the wavevector for the given ray and θ_m is the angle of the incident wave, of fundamental frequency, to the optical axis. Generally nonlinear crystals are cut for a specific wavelength such that the required angle of incidence,θ_m, for phase matching, is the normal to the crystal face.

2.5.2 Nonlinear Phase Shifts

In addition to changes in spectral phase due to the variation of $\boldsymbol{n}$ with frequency, changes to the spectral phase of a pulse can result due to non-linear effects [16]. An interesting result of the non-linear material polarization is a dependence of the mediums index of refraction on intensity of the propagating light wave. Considering the definition of the refractive index of a material [18]:

$$n = (1 + \chi)^{\frac{1}{2}}. \tag{2.24}$$

Manipulation of the polarization expansion 2.19 allows one to write the refractive index as a function of a linear refractive index, n_0, and a nonlinear refractive index, n_2, coupled to the intensity of the incident radiation.

$$n = n_0 + n_2 I \tag{2.25}$$

The dependence of the index of refraction on the intensity of the incident radiation is called the optical Kerr effect. This process is directly responsible for some

of the most fascinating phenomena in nonlinear optics such as self-focusing, self phase modulation and passive mode-locking. However the optical Kerr effect is undesirable during pulse amplification when self-focusing and nonlinear phase shifts due to self-phase modulation in the amplifier medium can lead to optical damage making pulses difficult to compress to the transform limit.

Quantification of the nonlinear phase shift in the time domain due to self-phase modulated can be estimated mathematically [16].

$$\phi_{nl}(\mathbf{r},t) = \frac{2\pi}{\lambda}\int n_2 I(\mathbf{r},t)dz \tag{2.26}$$

The peak value of ϕ_{nl} is known as the B-Integral and corresponds to the nonlinear phase shift at peak intensity of the incident radiation.

Equation 2.26 can be simplified and applied to a complete optical system of $\boldsymbol{n}$ components:

$$B(\mathbf{r},t) = \frac{2\pi}{\lambda_c}\sum_n \frac{I_p^n(r,t)n_2^n Z^n}{A^n} \tag{2.27}$$

Where $\boldsymbol{I_p(r,t)}$ is the intensity of the pulse in component $\boldsymbol{n}$ and $\boldsymbol{Z}$ and n_2 are the length and nonlinear refractive index of component $\boldsymbol{n}$, respectively.

The group delay caused by the nonlinear phase shift can be estimated as [19]:

$$\frac{d\phi}{d\omega} = \frac{B}{\Delta\omega} \tag{2.28}$$

where B is the value of the B-Integral and $\Delta\omega$ is the half-width of the amplified spectrum.

Chapter 3

Pulse Shape Simulation

3.1 Introduction

A computer program, PulseSim.m, designed to simulate the effects of dispersion on an optical pulse, was written in the Matlab programming language. The simulation was written to be used on a standard personal computer (in 2006 this is a 1GHz processor with 256MB of RAM), complete all calculations and return results in under a minute. The simulation produced a temporal profile for a pulse by performing a Fourier transformation (see section B.4) on a given spectral amplitude and phase profile. Figure 3.1 illustrates the flow of operations performed by the pulse shape simulation.

Spectral amplitude information, $|E(\omega)|$, was taken from the square root of a measured power spectrum or simulated with a Lorentzian or Gaussian function. It is noted that measured power spectra had to be transformed from wavelength to frequency space. An appropriate transformation function was used to maintain spectral envelope integrity (see appendix B.3 for a description of the transformation).

A spectral phase profile was built by applying refractive index profiles (appendix A) and material thicknesses, of the material components in an optical system being considered, to equation 2.12. Generally the spectral phase profile, for a complete optical system, was fit to a Taylor expansion about a central frequency and the zeroth and first order phase coefficients removed before simulation took place. As an alternative to using material refractive index profiles the phase coefficients to equation 2.13 could be entered to produce a spectral phase profile.

3.2 Resolution

Computational speed and system resources limited the ultimate precision and temporal resolution of the simulation. The actual mode spacing in frequency space

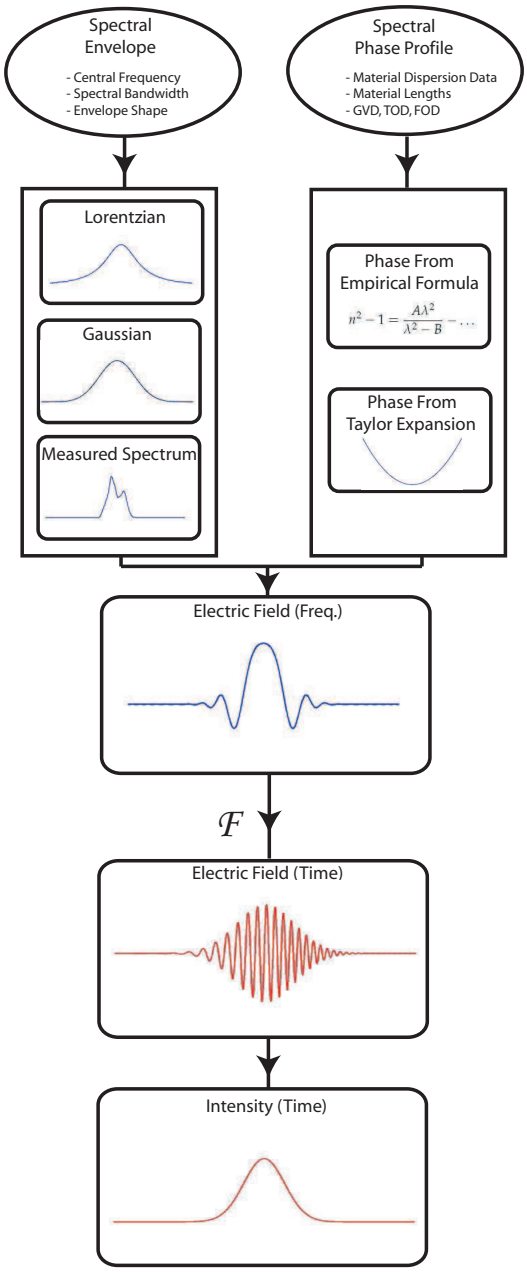

Figure 3.1: Flow of data and operations for the pulse shape simulation

of the pulses being simulated was given by:

$$\Delta f_{mode} = \frac{c}{L} \tag{3.1}$$

where $\boldsymbol{L}$ is the round trip length of the laser cavity producing the pulses. The round trip cavity length of the oscillator system, used in the lab, is 4m giving a frequency mode spacing of 75MHz. The central frequency of the oscillator system was 375 THz and spans from 425THz to 335THz which means that a concise simulation of the the oscillator would require at minimum a mode spacing of $7.5X10^{-5}$ giving 1.2 million modes. As the temporal resolution of the simulation is determined by the range of frequencies used (ranges of 700 THz were generally used), a simulation using 1.2 million modes over the spectral bandwidth would require far too long to complete. A more practical simulation uses a mode spacing of $0.01THz$. Simulations run with these parameters give the best computation time to accuracy ratio. Simulations run at an order of magnitude higher frequency resolution showed no noticeable increase in accuracy.

3.3 Simulation Accuracy

To test the ability of the simulation to return pulse shapes for varying spectral bandwidths, Gaussian spectral envelopes with varying bandwidths and flat spectral phase profiles were simulated. By the time bandwidth product (equation 2.3) the resulting FWHM of the temporal pulse should equal $\frac{4ln2}{\Delta\omega}$, for transform limited pulses. The results, figure 3.2, showed that the simulation was robust enough to accurately construct pulses with a temporal half-width as small as $\boldsymbol{6fs}$ and showed minimal errors in reconstructing pulses as short as $\boldsymbol{2fs}$. This limitation was primarily due to computer memory capabilities.

To test pulse reconstruction accuracy based on spectral phase profile a constant Gaussian spectral amplitude of spectral bandwidth, $\Delta\omega = 50THz$ was given a varying quadratic phase profile. The expected dispersion broadened temporal pulse width, τ_{out} is given by equation 3.2 [23].

$$\tau_{out} = (\tau_p^2 + \Delta\tau_d^2)^{\frac{1}{2}} \tag{3.2}$$

Where $\boldsymbol{\tau_p}$ is the temporal pulse width based on the spectral amplitude envelope alone and $\boldsymbol{\Delta\tau_d}$ is the expected pulse broadening due to dispersion [23]

$$\Delta\tau_d = \frac{d^2\phi_\omega(\omega_0)}{d\omega^2}\Delta\omega = GVD\Delta\omega \tag{3.3}$$

The simulated and theoretical results, shown in figure 3.3, show no noticeable deviation.

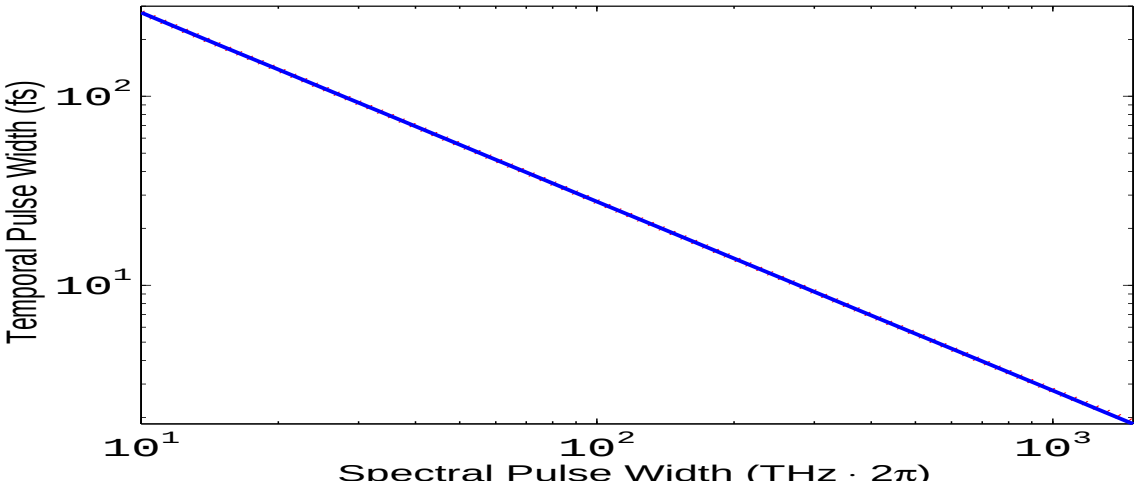

Figure 3.2: Simulated time-bandwidth products compared to theoretical predictions for pulses with a flat phase profile. The theoretical result lies directly on top of the simulated result

The effect of a constant value for the GVD ($10^4 fs^2$) on varying spectral bandwidths was also examined, with the results shown in figure 3.4. The transform limited pulse width is also shown in the figure, and indicates that for small bandwidths, dispersion has a decreasing effect on pulse width. For a GVD of $10^4 fs^2$ significant divergence of the pulse width from transform limit does not take place until the spectral bandwidth has reached a value of about $1.6THz$ or a bandwidth of $4nm$ FWHM for a pulse centered at $800nm$.

The simulation results were used to devise future experiments (section 7.3) and verify experimental measurements. The ability of the simulation to return pulse shapes, based on a spectral phase profile, was used throughout the next three chapters to perform calculations.

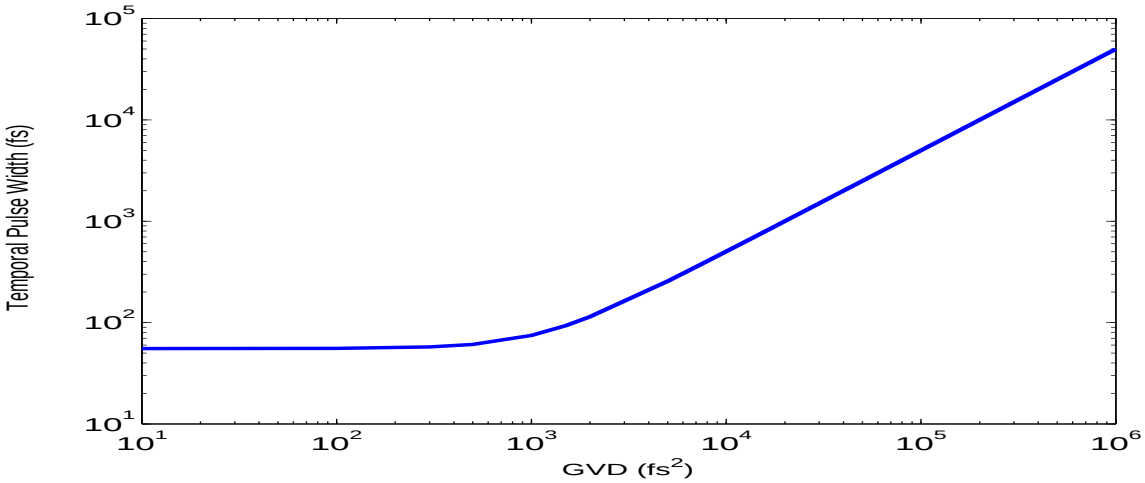

Figure 3.3: Simulated dispersion broadened pulse widths compared to theoretical pulse-widths for pulses with a spectral bandwidth, $\Delta\omega = 50$. The theoretical result lies directly on top of the simulated result

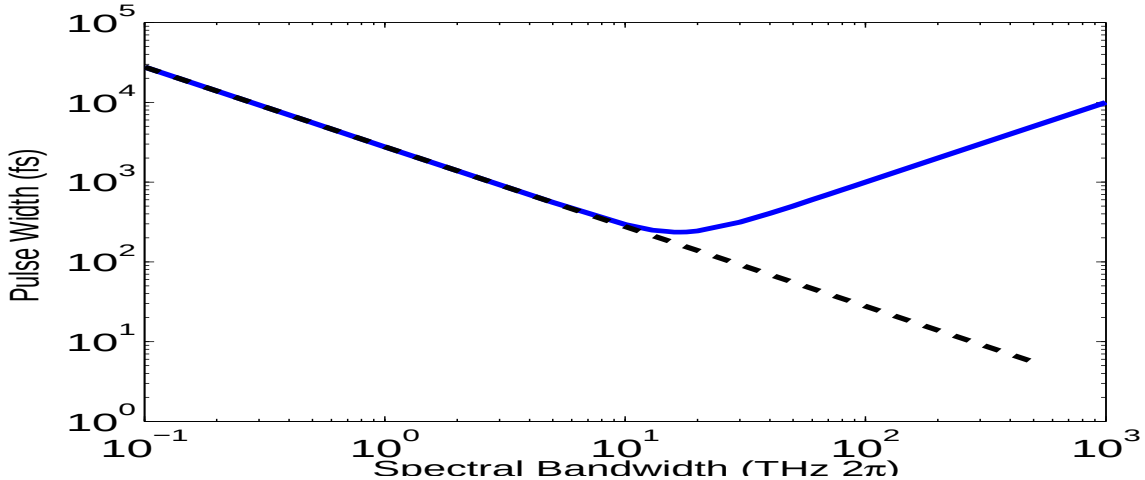

Figure 3.4: Simulated pulse widths against spectral bandwidth assuming a Gaussian spectral distribution with a constant GVD of $10000 fs^2$ (solid line) and transform limited (dashed line)

Chapter 4

Amplification

4.1 Introduction

Both the oscillator and amplifier systems, discussed here, are built around a titanium sapphire (Ti:saph) gain medium [6]. Figure 4.1 illustrates the absorption and emission bands of the Ti^{3+} ion, which is the active lasing medium in Ti:saph. Titanium sapphire has the broadest fluorescence bandwidth of any solid state, gas or liquid lasing medium making it the best choice for the generation of ultrafast laser pulses. The Ti:saph output bandwidth of $230nm$ FWHM centered at **790*nm*** (see figure 4.2) is large enough to support a transform limited pulse of $3fs$ in duration.

The general purpose of an optical amplifier is to increase the energy of a coherent source of radiation, heretofore called a 'seed'. In the case of a Ti:saph based amplifier the energy for amplification is provided by optically pumping the Ti:saph with an outside source in order to excite the electrons within it. When a seed is made to pass through the Ti:saph shortly after optical pumping has taken place, stimulated emission from the gain medium will occur. In the case of a resonant cavity amplifier, such as the regenerative amplifier, discussed later, the seed pulse is passed through the gain medium many times to extract the gain from the Ti:Saph, producing gains of up to 10^8 [19]. An important characteristic of the stimulated radiation from the gain medium is that it is coherent, emitted in phase with the radiation in the seed.

System Layout

The amplifier system that was built, presented below, was modeled after a 1kHz repetition rate CPA system presented in reference [14] in which stretching is performed by a 10cm long glass block of SF57 and pre-compensation of negative dispersion accumulated in the compressor is performed with TOD mirrors. The referenced design produced amplified pulses of $\sim 20fs$ duration and energies of $\sim 1mJ$. Our design varies from the referenced design in that a regenerative am-

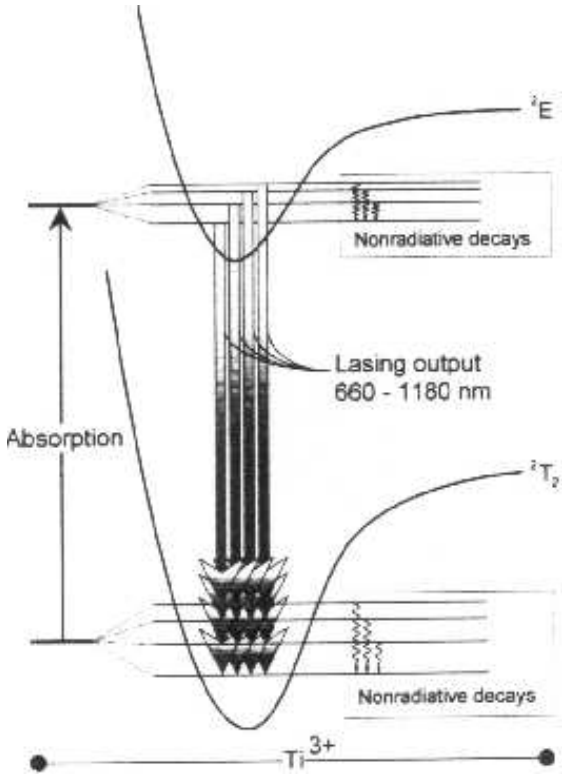

Figure 4.1: An energy level diagram of the absorption and emission bands of the Ti^{3+} ion. The ground state is given as $^2T_2$ and the excited state is given as ^2E

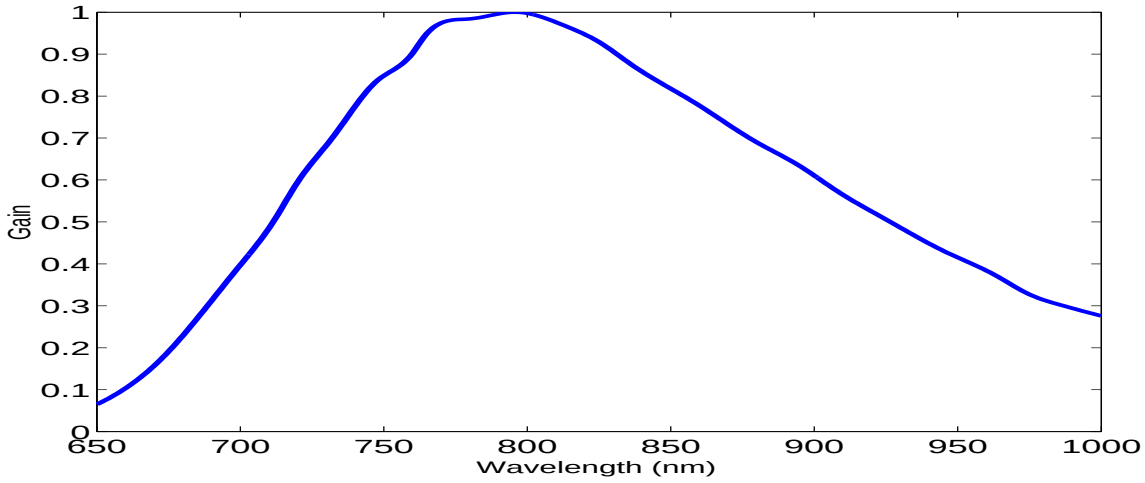

Figure 4.2: Gain spectrum for Titanium Sapphire

plifier system (regen) was used as opposed to a multi-pass amplifier and a large part of the stretching was performed by the glass elements in the regen cavity as opposed to stretching with a glass block before insertion into the amplifier. This change in design was motivated by the ease of setup, excellent amplified pulse spatial profiles, and large amplified bandwidths (using certain techniques) capable of being produced with regens, as discussed below.

In order to design a CPA system capable of producing energetic short pulses the design of the amplifier system must be carefully considered. In order to minimize the risk of damage to the amplifier components and optimize system performance, certain crucial characteristics of the amplifier system were determined and mod-

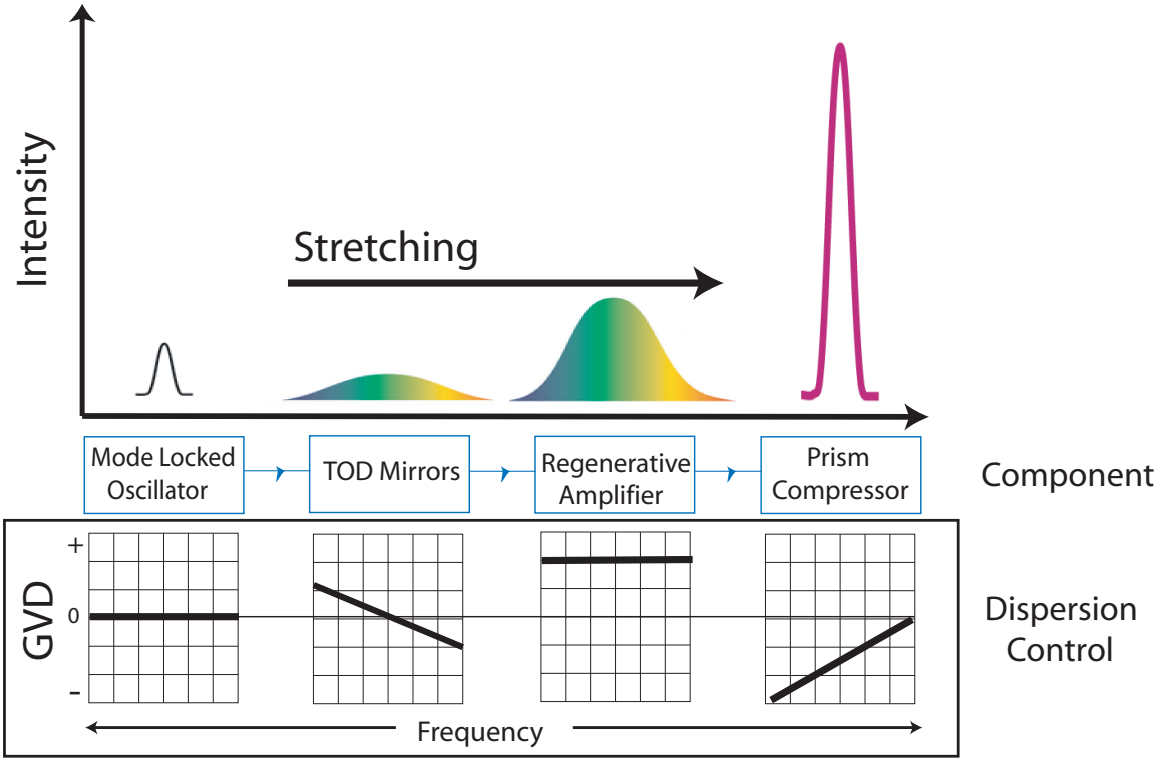

Figure 4.3: A flow chart showing the steps in the CPA process for the designed system. The initial pulse is a broadband mode-locked oscillator pulse which is stretched by third order dispersion (TOD) mirrors and the optical material in the amplifier system. The TOD mirrors are used to pre-compensate for negative third order dispersion in the compressor system. Above each listed step, the height of the pulse gives a relative indication of the pulse intensity and the horizontal scale gives a relative indication of the pulse width during that part of the process. Below each component a relative indication of the GVD against wavelength, provided by the corresponding part of the process, is indicated.

eled. The characteristics as determined can be broken down into four groups:

1. **Cavity Design**

   A simulation of the cavity stability was performed and the components inside the amplifier cavity were located. A geometry for the amplifier was chosen and the system was setup as a Q-switched laser.

2. **Spectral Transfer Function**

   In order to optimize the bandwidth of the pulses emitted from the amplifier, and thus minimize the possible pulse width after compression, a careful study of the spectral transfer function of the amplifier system, including the effects of gain in the amplifier, was performed. A spectral filtering technique called regenerative pulse shaping was used to maximize the amplified bandwidth.

3. **System Dispersion**

   The total system dispersion was modeled such that a simulated shape and temporal width of the pulse inside the amplifier could be estimated. This information was used to aid in designing the dispersive system that was used to compress the pulse after amplification, as discussed in section 5.

4. **Peak Internal Intensity**

   The intensity of the pulse within the amplifier was estimated using simulated pulse widths, obtained from calculations of the system dispersion, the mode size within amplifier, obtained from the cavity model, and estimates for the energy of pulses inside the amplifier.

The following sections detail the calculations and experimental work performed for each of the listed groups in sequential order.

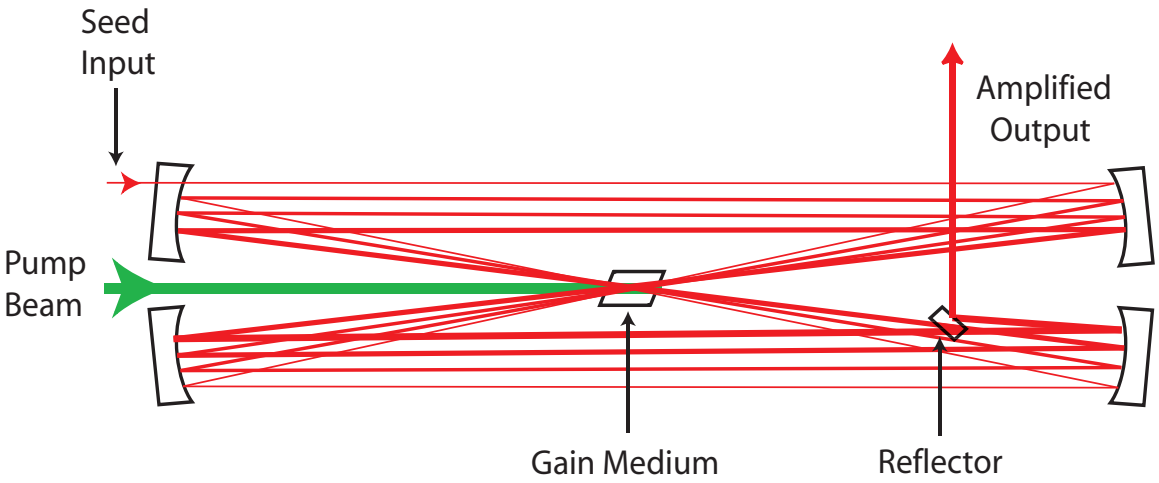

Figure 4.4: A bow-tie, or X, multi-pass amplifier scheme

4.2 Cavity Design

Of the many variant techniques of pulsed laser amplification there are two main categories into which all other techniques can be grouped. Each method, Multi-pass and Regenerative amplification, has it's advantages and disadvantages although neither technique stands out as a clearly accepted better method.

A brief review of the main variants of amplifier geometry is first presented in order that the reader better understand the nature of the amplifier system that was built. A description of the experimental procedure used in regenerative amplification, the chosen method for amplification, follows. Lastly the results of the cavity design model are presented and discussed.

4.2.1 Multi-Pass Amplifier

In a multi-pass amplifier, the seed is generally inserted into, directed through and extracted from the amplifier by reflection off many mirrors [19].

Although the arrangement for a multi-pass amplifier has many variants, each one has in common the fact that the optical path is not a resonator. An advantage of the multi-pass design due to the non-resonant optical path is the suppression of amplified spontaneous emission (ASE). However, a disadvantage of the multi-pass scheme is an inferior spatial mode as compared to amplifiers with resonant cavities. Furthermore, the intricate path that the seed takes in a multi-pass amplifier makes alignment more complex than that of a regenerative amplifier.

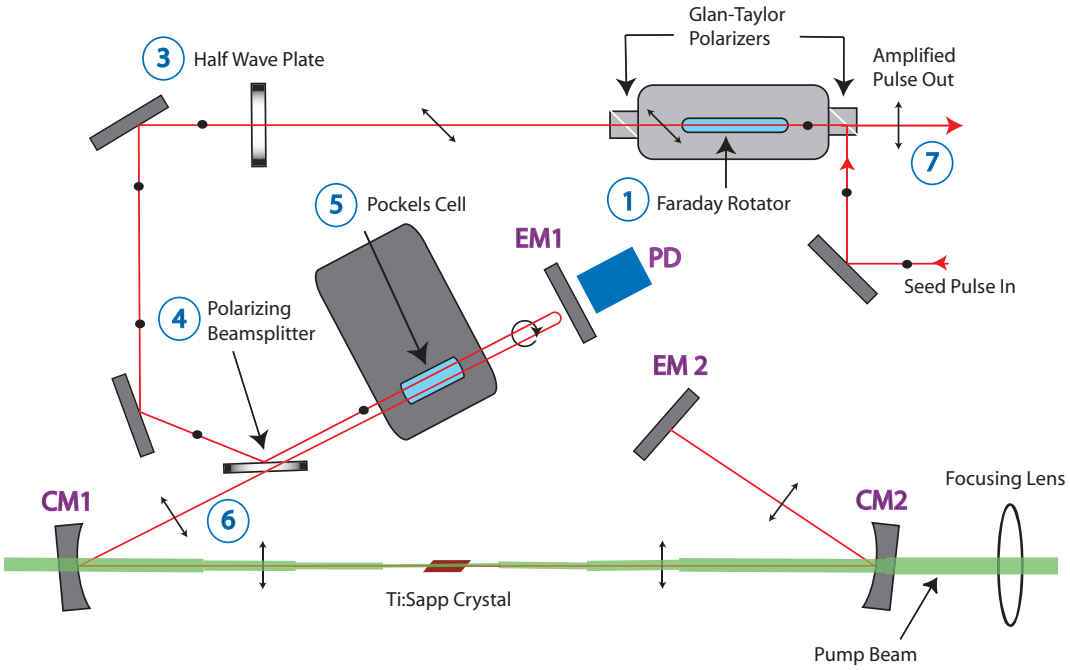

Figure 4.5: An illustration of a pulse being switched into (or out of) the regenerative amplifier. The polarization state of a propagating pulse is shown as a filled circle (vertical polarization), arrows perpendicular to the direction of propagation (horizontal polarization), arrows diagonal to the direction of propagation (diagonally polarized) or a circular arrow (circularly polarized).

4.2.2 Regenerative Amplifier

A regenerative amplifier (regen) is a resonant cavity which means that it will operate as a Q-switched laser without the insertion of a seed pulse. Advantages of a regen over a multi-pass amplifier technique include a simple alignment procedure and a good amplified beam profile due to the resonant cavity structure of the amplifier.

In order to amplify a pulse with the regen, a seed pulse must be switched into the regen cavity. Consequently the amplified pulse must also be switched out of the resonant cavity. Switching pulses in and out of the cavity is performed by polarization gating.

Polarization Gating

Seed pulses are switched into the regen cavity by using optics that control the polarization state of the seed pulse and other optics that selectively transmit or reflect light depending on it's polarization.

The steps involved in polarization gating are described with reference to figure 4.5 which illustrates the regen setup in the lab.

1. A seed pulse with vertical polarization passes through a polarizer that selectively reflects radiation with vertical polarization and transmits horizontal polarization.

2. Transmission through the Faraday rotator (Conoptics 713 Series Optical Isolator) results in a linear rotation of the polarization by 45^o counter clock-wise (CCW). Due to the magneto-optical 'Faraday effect' the direction of the polarization rotation of light passing through the Faraday rotator depends on the direction of propagation. A pulse traveling in the opposite direction would have it's polarization rotated 45^o clock-wise (CW). The seed pulse exits the Faraday rotator through a polarizer rotated to 45^o.

3. A **1/2λ** plate (Special Optics 8-9012-1/2), a polarization rotator without handedness, is used to rotate the polarization of the seed by 45^o CW, back to vertical polarization.

4. The seed is reflected at Brewster angle (70^o)by a polarizing beamsplitter (Alpine Research Optics PL6020) that selectively reflects vertically and transmits horizontally polarized light, respectively.

5. The vertical polarization of the seed is rotated by 90^o with two trips through a Pockels Cell (Medox) (operating as a $1/4\lambda$ plate). The Pockels cell induces the Pockels effect causing a dielectric (DKDP, QX1020 crystal) to change it's birefringence under the influence of a linear external electric field. By applying an electric field of appropriate strength the Pockels cell can be made to act as a $1/4\lambda$ or $1/2\lambda$ plate.

6. The horizontally polarized pulse is transmitted through the polarizing beamsplitter and makes a round trip through the regen cavity. On two more trips through the Pockels cell the seed polarization is rotated back to vertical and is ejected from the cavity. However, the seed can be trapped inside the cavity if the Pockels cell is made to act as a $1/2\lambda$ plate while the seed is propagating through the laser cavity. The seed pulse can later be switched out of the laser cavity by causing the Pockels cell to act as a $1/4\lambda$ plate.

7. A seed or amplified pulse switched out of the regen cavity will have vertical polarization. When the pulse travels through the $1/2\lambda$ plate it will have it's polarization rotated by 45^o CW. Due to the direction of propagation through the Faraday rotator the pulse will have it's polarization rotated 45^o CW again, resulting in horizontal polarization and transmission through the polarizer at the end of the Faraday rotator.

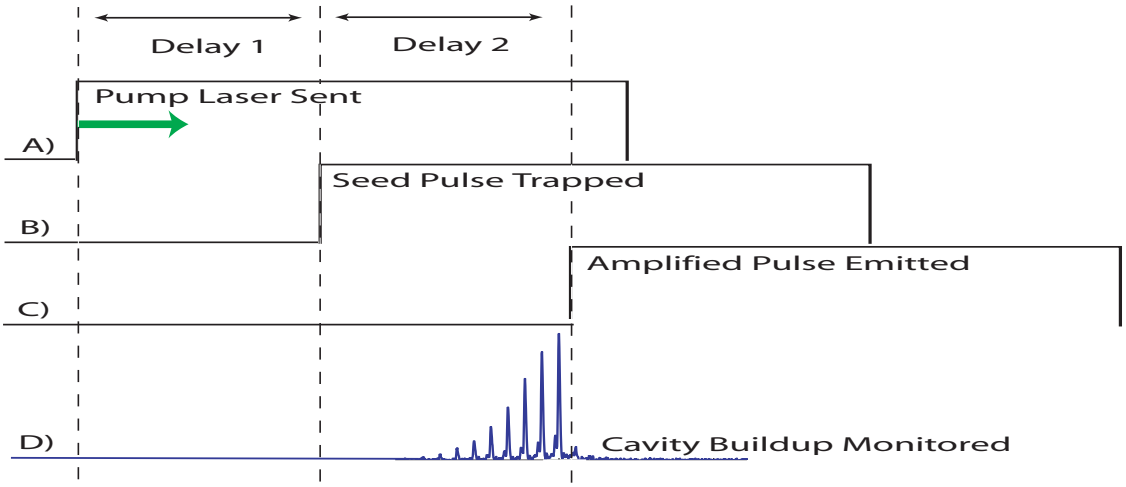

Figure 4.6: The steps involved in timing amplification starting with; A) A kHz clock signal from the Pockels cell triggers the Pump laser, sending a pulse with$\sim 7mJ$ at $527nm$ to the Ti:saph in the regen, B) Delay control one sets the time between sending the pump laser and trapping a seed pulse in the regen cavity, C) Delay control two sets the time between trapping and releasing a pulse from the cavity. D) The cavity buildup is monitored with a photodiode in order that the timing controls can be set to emit an amplified pulse from the cavity at peak gain.

Timing

In order to amplify a pulse efficiently, a seed pulse must be trapped inside the regen at an appropriate time after the Ti:saph has been optically pumped. This is performed by manipulating timing controls on the Pockels cell and pump beam controller.

The Pockels cell uses a radio frequency (RF) driver capable of producing and switching a multi kV signal at kHz repetition rates with ns precision. The repetition rate of the Pockels cell high-voltage switching is set by a clock signal derived by measuring the modelocked pulse-train emitted from the oscillator with a fast photodiode (Thor Labs DET210). The repetition rate of the modelocked pulse-train (75MHz) is divided internally to produce a 1 kHz clock signal. Two delay settings on the Pockels cell driver with a temporal resolution of 2ns each, control when high voltage steps are applied after each 1kHz clock signal.

The timing procedure is described with reference to figure 4.6. First (A, in the figure), the 1kHz clock signal from the Pockels cell driver is sent to the q-switched pump laser (Quantronix Falcon Nd:YLF lamp pumped laser, up to $10W$ @$527nm$). Next (B, in the figure), the first delay control on the Pockels cell sets the time after the first 1kHz signal that the Pockels cell is made to act as a $1/2\lambda$ plate, trapping a pulse inside the cavity. With an appropriate time set between sending a pulse

from the pump laser to the gain medium and trapping a seed pulse in the cavity, optimal amplification, and suppression of ASE, for a given pump power, can be achieved. Finally, delay two is set (C, in the figure) such that peak amplification, monitored with the photodiode described above (D, in the figure), and emission of the pulse from the cavity take place during the same round trip in the regen.

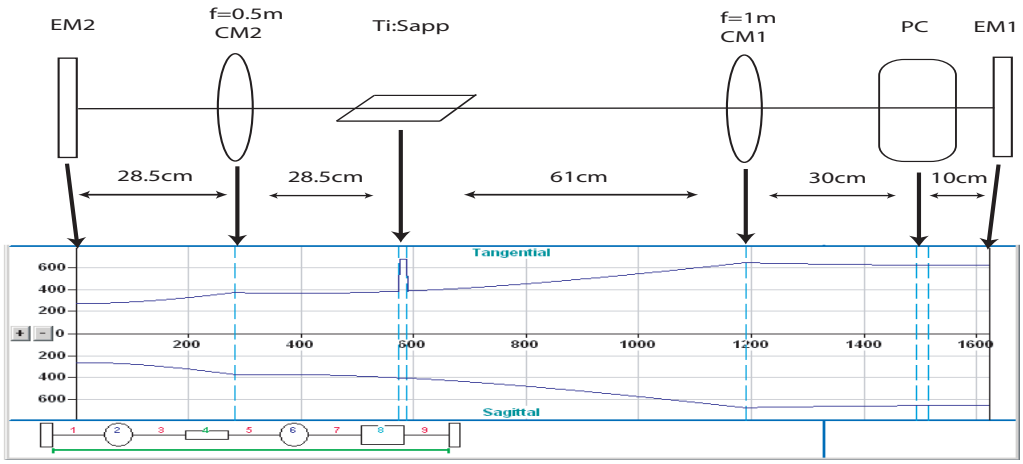

Figure 4.7: The simulated mode size inside the regen cavity based on a Gaussian beam propagation simulation. The positions between each element in the cavity, for a simulated stability of 0.9, are also shown.

4.2.3 Cavity Stability

In order to guarantee a stable laser it is necessary to design the laser cavity such that rays sent into the cavity, parallel to it's axis, experience minimal divergence from the initial trajectory after repeated reflections through the cavity. Mathematically the cavity stability is a function of the focal lengths of the lenses or mirrors used inside the cavity and the distances between the optical elements in the laser cavity. A laser cavity is considered stable if it's stability value is between 0 and 1.

In order to locate the amplifier components and ensure a stable laser cavity a simulation of the cavity stability as a function of component position was performed by Dr. Xiaoming Sun. The software package WinLase 1.0 was used for this purpose. WinLase simulated the propagation of a Gaussian beam through a laser cavity defined in terms of the relative position, surface curvature and refractive index (for transparent materials) of each optical element. The simulation produced results for both cavity stability as a function of element position and the mode size within each element in the cavity.

For the setup shown in 4.7 the stability of the laser was simulated to be 0.9. The mode size in the Ti:saph crystal was simulated to be $\sim 400\mu$m in radius, which is near the generally accepted mode size of 300μm used in many regen cavities.

The total length of the regen cavity, determined after modeling, was 3.2 m which equates to a round trip time of $\sim 10.7ns$. The mode-locked oscillator, which seeds the regen has a cavity length of 4 m which equates to a round-trip time of $\sim 13.3ns$. Because of the difference in round trip times there is no chance that two pulses, separated by the round trip time of the oscillator, can both be in the regen

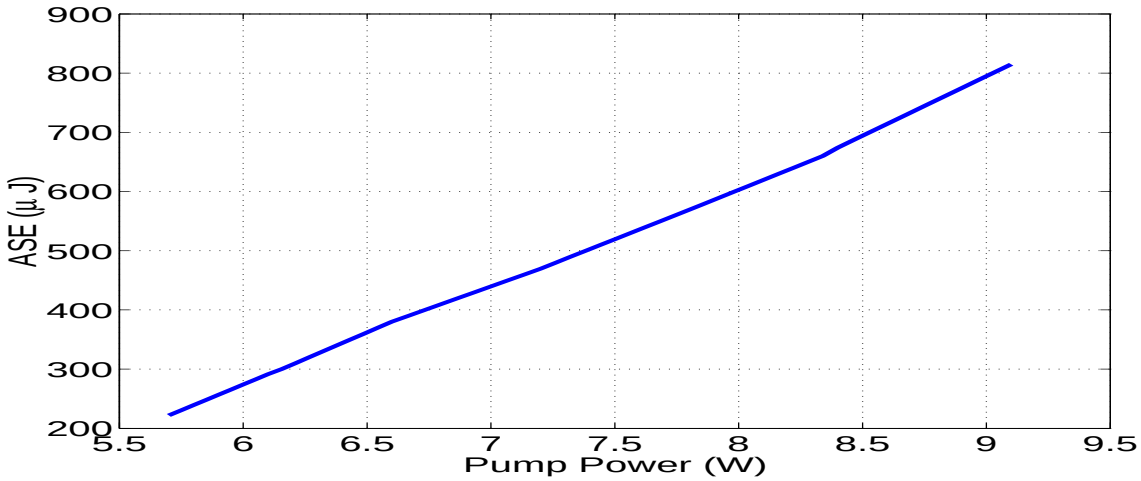

Figure 4.8: ASE energy output from the regen vs. pump power

cavity at the same time.

An X-folded arrangement was chosen for the amplifier geometry, providing a small footprint on the optical table. The laser was setup, as described above, and tested in ASE mode (without a seed pulse) and was shown to provide good output energy vs pump power as shown in figure 4.8. In order to provide sufficient amplified bandwidth the spectral transfer function of the regen was next considered.

4.3 Spectral Transfer Function

For maximum extraction efficiency an amplifier must be run above the saturation fluence of the gain medium [24] ($1J/cm^2$ for Ti:saph). Considering the damage threshold of the optical coatings of most dielectric mirrors ($5J/cm^2 X \tau_p^{\frac{1}{2}}$ where τ_p is pulse duration in ***ns***), this requires the seed pulse to be on the order of 300ps. This is far wider than the pulse width in most amplifier systems [25], indicating that maximum extraction efficiency is not usually obtained. Maximum amplification efficiency, however, is not the goal of this system; instead we seek to obtain as short a pulse as possible, which requires the capability to produce wide amplified bandwidths.

In order to develop an amplifier system capable of producing wide amplified bandwidths a careful study of the limiting phenomena must be done.

If gain saturation is neglected temporally varying amplification effects can be ignored allowing for a treatment of the output pulse intensity in terms of spectral intensities only [26].

$$I_{out}(\omega) = I_{in}(\omega)G(\omega)^p T(\omega)^p \tag{4.1}$$

Where $G(\omega)^p$, is the frequency-dependent gain, $I_{in}(\omega)$, the spectral intensity of the seed, and $I_{out}(\omega)$ the spectral intensity of the amplified pulse. The transfer function of the optics in the amplifier is given by $T(\omega)$ and is discussed below.

4.3.1 Measured Optical Transfer Function

The relative transmission, of the optics in the stretching and amplifying parts of the CPA system, were measured using a broadband CCD grating spectrometer (Special Order from Lighting Sciences Canada), in order that the terms $I_{in}(\omega)$ and $T(\omega)$ in equation 4.1 could be quantified.

The measured relative transmission of the TOD mirror (Serial #$M224$, Femtolasers Inc.) setup (78 reflections) is shown in figure 4.9, including the input and output spectra. The TOD mirrors were quoted for near 100% reflectivity over the range of 750 to 850 nm. Despite this, best efforts in the alignment of the TOD mirrors produced spectra that showed a weaker reflectivity than expected in the region from 750 to 800nm. However, this was not considered to be a serious issue as the massive gain in the amplifier, and the spectral filtering technique that was used, would be seen to provide broad-bandwidth amplified spectra as long as some seed light, across the bandwidth, was inserted into the regen.

The measured relative transmission of the Faraday rotator is shown in figure 4.10. The results indicated that the Faraday rotator provided a broad transmission range from 710 to 900nm. These results were consistent with the quoted transmission profile provided by Conoptics Inc.

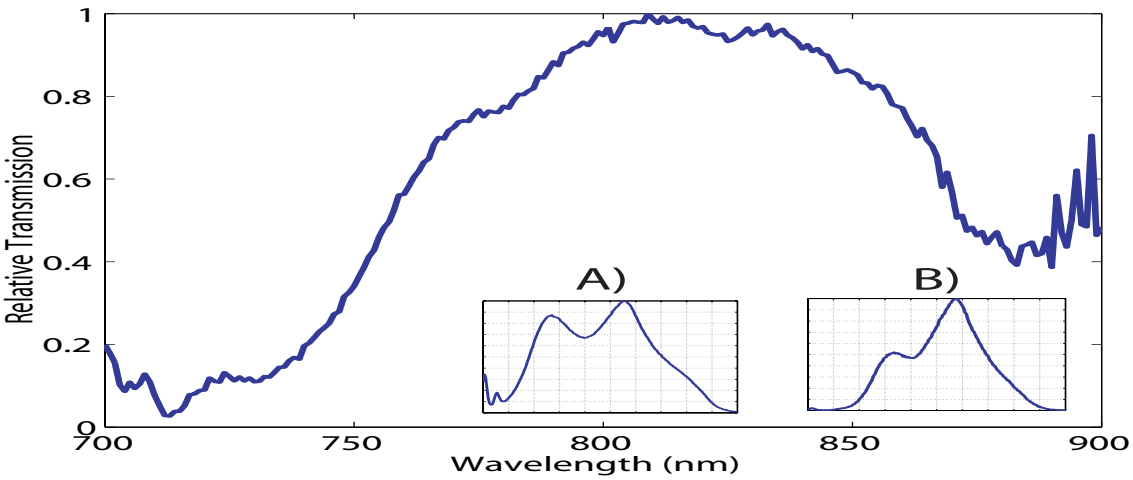

Figure 4.9: Relative transmission of the TOD mirror system, setup for 78 reflections of the oscillator pulses. The insert shows A) the input spectrum and B) the output spectrum.

High damage threshold cavity (HDTC) mirrors (Special Order from Femtolasers), were obtained in order to replace older cavity mirrors, with a narrow reflectivity spectrum, used in the previous laser design. The new HDTC mirrors (EM1,EM2,CM1 and CM2 in figure 4.5) were specified to be highly reflective over the wavelength region of the oscillator. The spectral transfer function of the laser cavity was measured, as a complete system, by sending pulses directly from the oscillator through the regen cavity so that, on average, the spectral transfer function due to 1 round trip in the regen was measured. The measured spectral transfer function is shown in figure 4.11. The result shows that the laser cavity provides broad spectral transmission from $\sim$ 720 to 850nm.

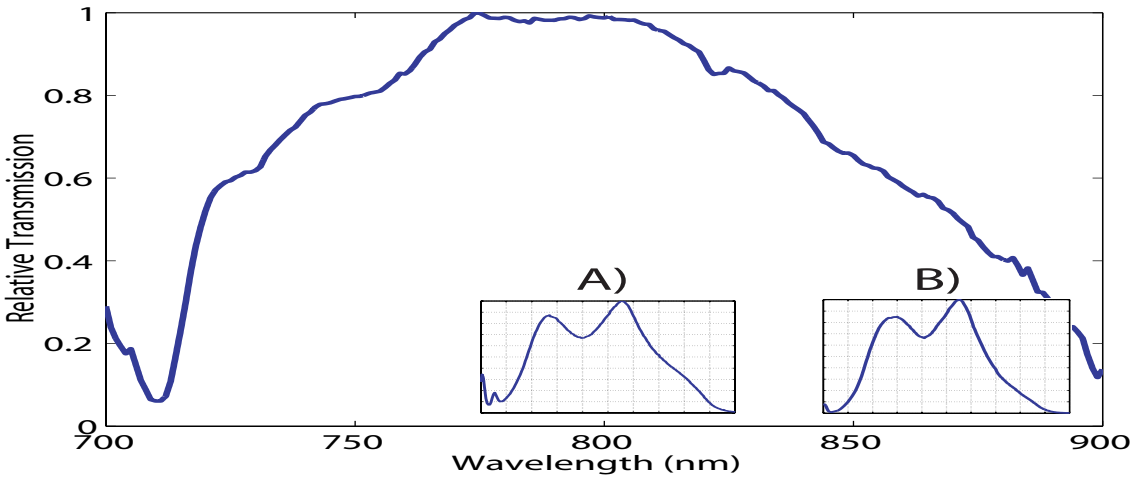

Figure 4.10: Relative transmission of the Faraday Rotator. The insert shows, A) the input spectrum and B) the output spectrum.

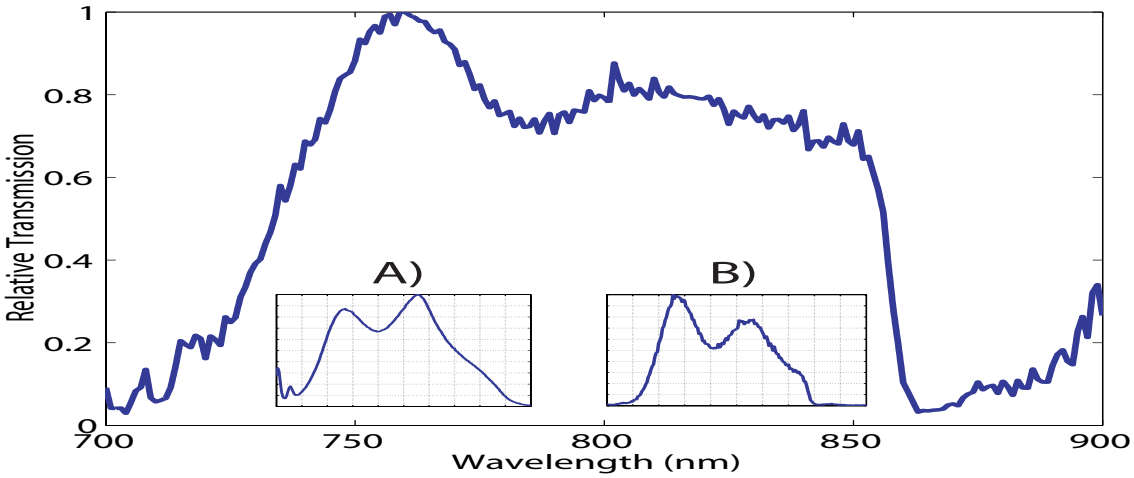

Figure 4.11: Relative transmission of the regen cavity including the HDTC mirrors, polarizing beamsplitter, Pockels cell and Ti:saph crystal. The insert shows A) the input spectrum and B) the output spectrum.

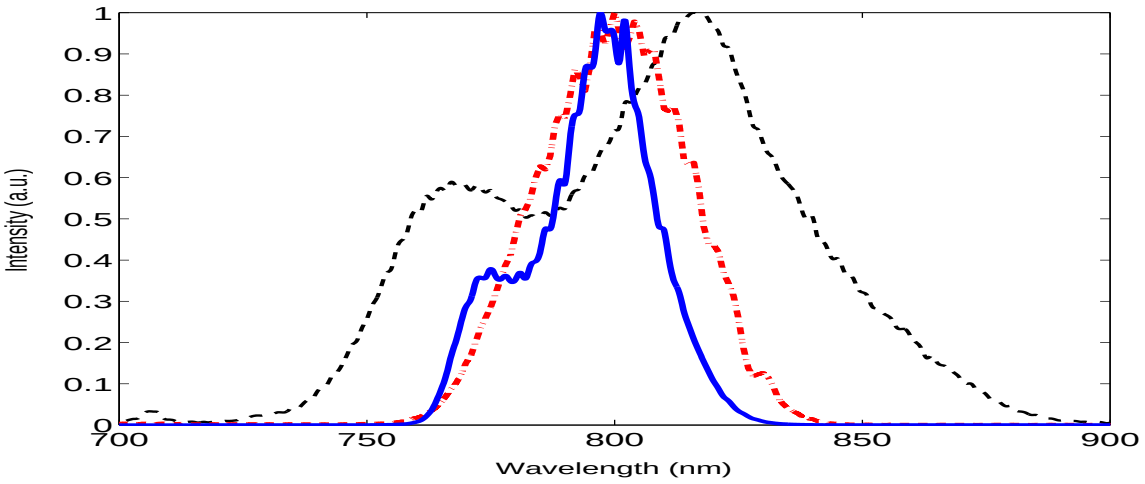

Figure 4.12: Simulated (solid line) and measured (dash-dot line) effects of the gain spectrum on amplified spectral bandwidths with a broad input spectrum (dashed line), 23 round trips in the amplifier and an amplifier transfer function of unity

4.3.2 Gain Narrowing

Generally, short pulses ($< 40fs$) from an amplifier are not easily realized as most gain materials, including Ti:saph, have a frequency dependent gain profile. In regen systems, a net gain of $> 10^7$ is common, requiring many passes through the gain medium ($10 - 30passes$). The frequency dependent gain profile naturally leads to a reduction in the amplified bandwidth. In fact, given a gain of 10^7 in Ti:saph, for a seed pulse with an infinitely broad input spectrum the amplified pulse bandwidth will be reduced to $\sim 45nm$ FWHM [25]. This process is called gain narrowing.

Gain narrowing produces two undesired effects. Firstly, it reduces the overall width of a broadband stretched pulse as it propagates within the amplifier. Equation 3.3 and figure 3.4 show that for a sufficiently stretched pulse the pulse width is directly proportional to it's spectral bandwidth. Wide pulse widths are desirable inside the laser cavity during amplification in order to reduce the intensity of the pulse and subsequently the potential for damage or non-linear phase shifts. Secondly, as can be seen from equation 2.3 gain narrowing increases the transform limited pulse width after re-compression. As short as possible transform limited pulse is desired after re-compression as this will provide for more intense laser pulses for experimental use.

The effects of gain narrowing for a given seed spectrum and gain profile can be simulated using equation 4.1, as shown in figure 4.12.

Spectral Filtering

To counteract gain narrowing a number of techniques have been proposed [9] [27] that involve the introduction of frequency dependent losses, at the peak of the gain profile, within the amplifier cavity. A successful method, called regenerative pulse shaping [9], involves the insertion of two thin film (3μm) etalons into the amplifier cavity. Barty et al. showed that this technique could be used to selectively amplify the wings of the spectrum, and produce sufficient amplified bandwidth to produce $15fs$ bandwidth limited pulses.

By changing the angle that the etalons made with the optical axis of the laser cavity, the spectral transmission profile of the etalons can be changed. When the etalon thickness is made to be an even multiple of $1/4\lambda$ destructive interference takes place between the front and rear surface reflections of the etalon. For an etalon thickness of an odd multiple of $1/4\lambda$ constructive interference takes place between front and rear surface reflections in the etalon.

The authors of [28] give a mathematical expression for the spectral transmission, $\boldsymbol{T(\omega)}$, in air for an etalon of thickness $\boldsymbol{d}$ with an index of refraction $\boldsymbol{n}$, reflectivity $\boldsymbol{R}$, and angle $\boldsymbol{\theta}$.

$$T(\omega) = \frac{1-R}{(1+R^2-2Rcos(2\omega t_0))^{\frac{1}{2}}} \tag{4.2}$$

where the equivalent vacuum passage time, t_0, is given by:

$$t_0 = \frac{nd}{c}\frac{1}{\cos(\arcsin(\frac{\sin\theta}{n}))} \tag{4.3}$$

4.3.3 Broadened Amplified Bandwidths

In order to counteract the effects of gain narrowing two nitrocellulose un-coated thin-film etalons , of nominal thickness 2μm (Melles-Griot 03-BPL-003), were placed into the amplifier cavity on rotatable mounts so that the optical angle of incidence, on each etalon, could be made to vary thus adjusting the angle $\boldsymbol{\theta}$ in equation 4.3 and subsequently the spectral transmission function of the etalons.

It was found that, for two etalons at angles of 7^o and 15^o respectively, an amplified spectrum capable of producing $< 20fs$ FWHM pulses could be produced as shown in figures 4.13 and 4.15. The simulated amplified spectrum, using equations 4.1 and 4.2 with the etalons at angles of 7^o and 15^o, is also shown in figure 4.13.

The measured spectrum from figure 4.13 was determined to be optimal in light of the bandwidth limited pulse shape obtainable with such a spectrum, as shown in figure 4.15, compared to the bandwidth limited pulse shape obtainable using separately measured amplified bandwidths shown in figure 4.14. The oscillating

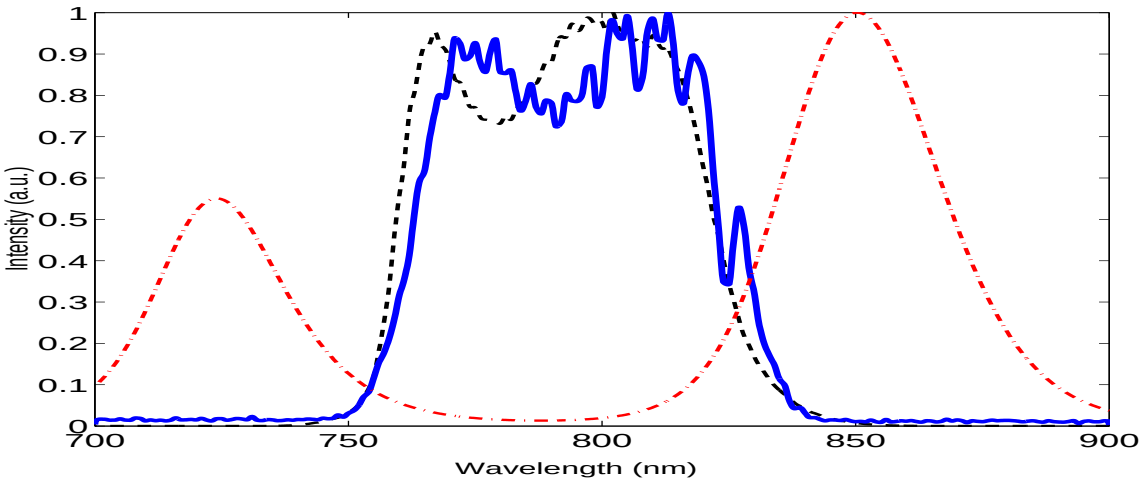

Figure 4.13: Simulated (dashed line) and measured (solid line) amplified spectra for 23 round trips in the amplifier with nominally 2μm thick etalons placed in the regen cavity at incident angles of 7^0 and 15^0 respectively. The simulated transmission spectra of the etalons for 23 round trips is also shown (dash-dot line)

features in the spectrum are described later and thought to be due to a reflection taking place in the amplifier.

It was found that occasional tuning of the etalons was required. This was thought be due to the thickness of the filters varying over time as material was eroded from the surface of the etalons by the amplified laser pulses. However in addition to providing plenty of extra amplified bandwidth the etalons proved to be advantageous in that by reducing the single pass gain in the laser a given laser pulse required more round trips in the regen, for a given pump power, in order to reach maximum gain. This was seen as advantageous as more round trips in the amplifier provided more material dispersion and thus longer pulse widths and lower intensities inside the amplifier as discussed below.

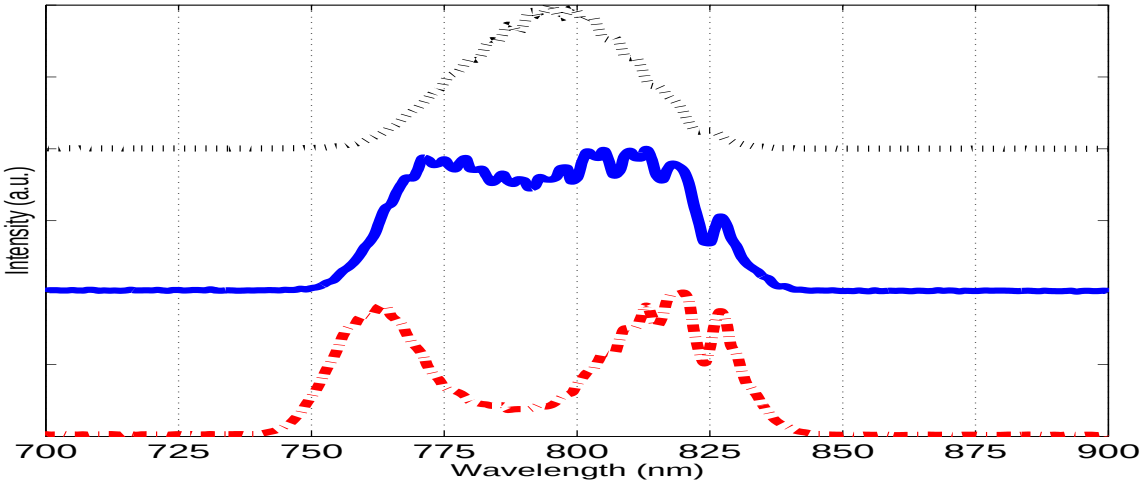

Figure 4.14: Measured spectra corresponding to the spectrum out of the amplifier with; no spectral filter (dotted line), intra-cavity etalons at angles of 7^o and 15^o (solid line) and the broadest spectrum obtainable using the intra-cavity etalons (dash-dot line).

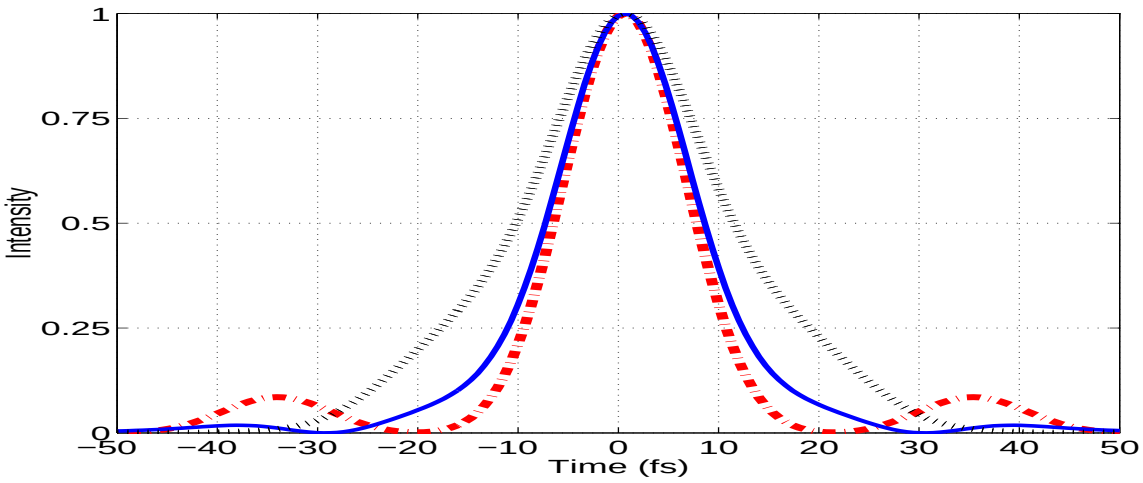

Figure 4.15: Simulated transform limited pulse shapes given spectra from the amplifier with; no spectral filtering (dotted line, 38nm FWHM spectrum), and spectrally filtered amplified spectra with FWHM's of 62nm FWHM (solid line) and 80nm (dash-dot line) from figure 4.14. The effect of the shape of the spectrum on the pulse shape is particularly apparent in the case of the very wide spectrum where significant side peaks can be seen.

4.4 System Dispersion

In order to determine the spectral phase accumulated by a propagating pulse in the CPA system, the dispersive properties (see section 2.3) of each of the optical components in the system must be determined. The components of the designed CPA system can be subdivided into reflective and transparent optical components.

The dispersive properties of each transparent optical component can be determined from the refractive index of the component over the spectral region of interest (with the exception of the intra-cavity etalons). Refractive index data was obtained from a variety of sources as described in appendix A. Where necessary, refractive index data was determined by fitting to supplied curves.

The dispersion imparted by each reflective optical component was determined from group delay (GD) or group-velocity dispersion (GVD) profiles acquired from the respective manufacturer of the optical component. Where not presented below, the dispersion information for each reflective element is summarized in appendix A.2.

A simulation, 'DispRegenElements.m', was written using the MatLab programming language in order to determine the dispersion accumulated by pulses traveling through the TOD mirror system and the dispersive elements in the regen. The simulation was designed with the capability to use the refractive index data and/or dispersion profiles for all of the optical elements in the system, as described above. The simulation returned both phase as a function of wavelength and GVD as a function of wavelength, for the optical system being considered. However, to appreciate the relative amount of dispersion due to each of the components in the system, dispersions are presented here, where appropriate, in tabular format, in terms of GVD, TOD and FOD at a central wavelength.

4.4.1 Amplifier Dispersion

For the designed CPA system a majority of the pulse stretching took place inside the regen. Each round trip in the regen adds system dispersion as the seed pulse travels through more material. The target number of round trips for the amplifier presented here was initially set to 23. This was based on the number of trips required to deplete the cavity gain while running the regen pump laser at a reasonable power level($\sim 7W$).

The dispersion accumulated by a pulse on insertion into (or emission from) the regen system traveling from points M1 to EM1 in figure 4.16 is summarized in table 4.1.

Round trips in the regen were measured by monitoring the leakage signal through an end mirror (EM1 in figure 4.16) in the regen as described in section 4.2.2. Round trips were defined as the path from end mirror EM1, through the regen cavity, and back to EM1. The dispersion accumulated by a pulse per round trip in the regen

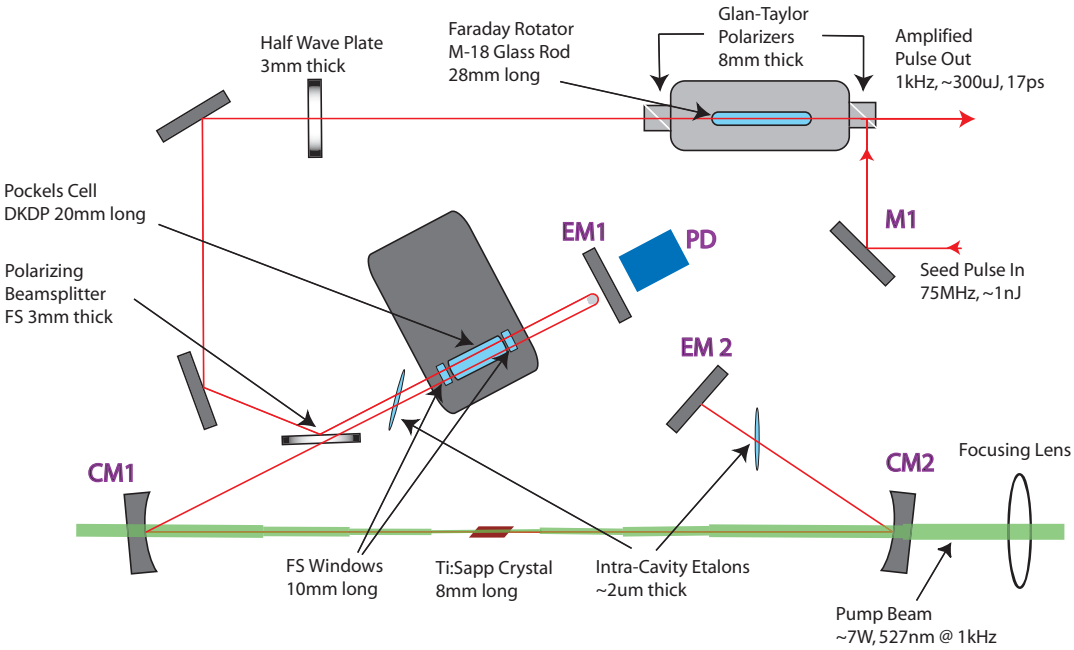

Figure 4.16: An illustration of the regenerative amplifier cavity indicating the optical material of significance and corresponding thicknesses in the regen. The cavity end mirrors are EM1 and EM2, the curved cavity mirrors are CM1 and CM2. The photodiode, PD, monitors the cavity buildup. The point of insertion into the amplifier system is M1.

Optical Element	Length (mm)	GVD $(10^3 fs^2)$	TOD $(10^3 fs^3)$	FOD $(10^3 fs^4)$
Faraday Rotator (M-18)	28	2.5	0.36	0.89
Faraday Rotator (Polarizers)	16	1.2	0.85	−0.15
Pockels Cell (KD*P)	20	0.71	0.81	0.5
Pockels Cell Windows (Fused Silica)	10.2	0.37	0.28	-0.12
Totals		4.8	2.3	1.1

Table 4.1: Total dispersion accumulated traveling from points M1 to EM1 in figure 4.16

Optical Element	Length (mm)	Total GVD ($10^3 fs^2$)	Total TOD ($10^3 fs^3$)	Total FOD ($10^3 fs^4$)
Polz. Beam Splitter (BK7 Glass)	.08	0.37	0.27	-0.08
Pockels Cell (KD*P)	40	1.4	1.6	1.0
Pockels Cell Windows (Fused Silica)	20.3	0.73	0.56	-0.23
Ti:saph	16	0.73	0.53	-0.18
Totals		3.3	3.0	0.5

Table 4.2: Accumulated dispersion per round trip in the regen

Source	GVD ($10^3 fs^2$)	TOD ($10^3 fs^3$)	FOD ($10^3 fs^4$)
FemtoLasers Specs	0.1 $\pm$0.02	2.4$\pm$0.6	20$\pm$2
Fit to Data	0.12	2.27	17.65

Table 4.3: Dispersion per reflection off of TOD mirrors quoted by Femtolasers and as determined from a fit to measured data, provided for one of the mirrors.

cavity is presented in table 4.2.

4.4.2 Third Order Dispersion Mirrors

The TOD mirrors, dispersive dielectric stacks, were designed to provide a large amount of third order dispersion over a broad bandwidth (720nm-880nm). Figure 4.18 gives a plot of the measured GVD vs. Wavelength, provided by FemtoLasers, for a single reflection from a TOD mirror (Serial # $M224$). The properties of mirrors produced in each batch are variable and the manufacturers quoted tolerances are given in table A.2.

4.4.3 Intra-Cavity Etalons

In order to determine the dispersion due to thin-film etalons placed inside a regen cavity a procedure as outlined by Barty et. al. [29] was used. First the regen was setup with the etalons angled correctly to provide the desired spectral output (figure 4.13). One etalon was then removed and the pump power decreased so that many round trips in the regen were required in order to produce a measurable ASE output spectrum. This guaranteed that amplification only took place at

the resonant peak of the etalon and therefore could be determined with a spectral measurement. This process was then repeated to measure the resonant peak of the second etalon.

Using the measured angles of incidence (7^o and 15^o respectively), the measured resonant peaks (772nm and 818nm respectively) and a reflectivity of 4%, over the spectral region of interest, the effective thickness of each etalon was determined. This was done by inserting an equation for the etalon transmission as a function of frequency and thickness (equations 4.2 and 4.3) into the amplifier spectral transfer function (equation 4.1) and adjusting the etalon thickness in order to fit a simulated spectrum to each measured resonant peak spectrum. The simulated spectra fit the measured resonant peaks well using thicknesses of 1.93μm and 1.79μm respectively, which also matches well with the etalon manufacturers quoted etalon thickness value of $\leq 2\mu$m. The simulated and measured resonant peaks for each etalon is shown in figure 4.17.

Given the thickness of each etalon a calculation of the group delay due to each etalon follows from reference [28]:

$$GD(\omega) = t_0 \frac{1 - R^2}{1 + R^2 + 2R\cos(2\omega t_0)} \tag{4.4}$$

Where t_0 is the equivalent vacuum passage time from equation 4.2, R is the reflectivity of the etalon and GD is the frequency dependent group delay.

The corresponding GVD profile for both etalons for 23 round trips in the regen is shown in figure 4.18. It is noted that the same procedure was performed using the values given in reference [29] and a good match with the results was obtained.

4.4.4 Other System Dispersion

The dispersion due to other elements in the CPA system such as the HDTC mirrors in the regen cavity as well as the many beam steering mirrors and beamsplitters in the optical path were considered and included into the dispersion simulations. The dispersion due to the HDTC mirrors was significant due to the many round trips in the regen. A GVD profile for the HDTC mirrors (obtained from FemtoLasers) is shown in figure 4.18.

4.4.5 Total Dispersion

The total dispersion for the amplifier system, including 50 reflections on TOD mirrors, is shown in figure 4.4.5. The TOD mirrors were used to compensate for the negative third order dispersion produced by the prism compressor presented in section 5. The value of 50 TOD mirror reflections is based on results provided by the prism compressor simulation.

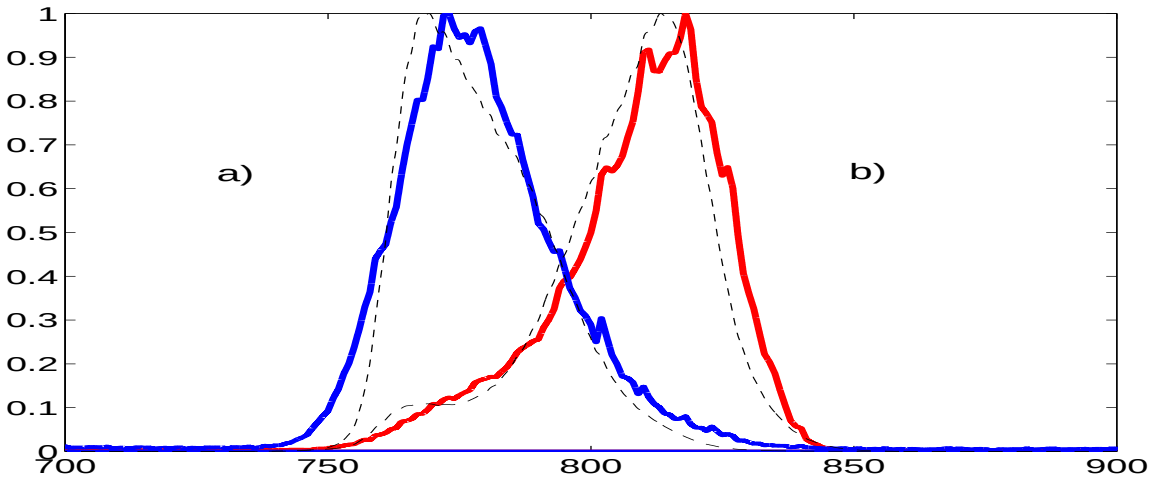

Figure 4.17: Measured (solid lines) and calculated (dashed lines) spectra from the regen using intra-cavity etalons tuned to a) 7^o and b) 15^o. The calculated spectra are based on etalon thicknesses of a) 1.93μm and b) 1.79μm

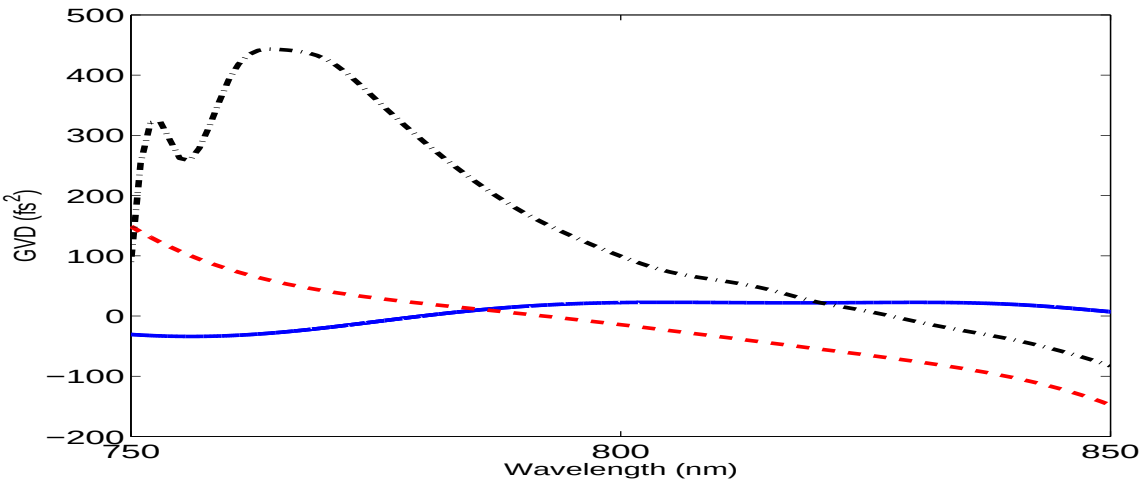

Figure 4.18: Calculated GVD accumulated by the pulse for one round trip in the regen as a result of the intra-cavity etalons (solid line) and the high damage threshold cavity mirrors (dashed line) or for one reflection from a TOD mirror (dashed-dot line).

	Total GVD ($10^3 fs^2$)	Total TOD ($10^3 fs^3$)	Total FOD ($10^3 fs^4$)
Other Dispersions	2.2	1.1	-0.2
TOD Mirrors (50 Ref)	5.0	120	1000
Regen 23 Round Trips (full system)	85	73	14
Totals	92	194	1013.8

Table 4.4: Total dispersion accumulated by an amplified pulse on exiting the regen system after 23 round trips and 50 reflections from TOD mirrors.

4.5 Peak Internal Intensity

4.5.1 Estimate of Pulse Energies Inside the Regen

The energy of ASE from the regen, both before and after transmission through the rotator, was measured and a transmission of 80% was determined. In addition to this, the polarizing beamsplitter in the regen (Alpine Research Optics PL6020) is quoted for a reflectance, for vertically polarized light, of 75%. Therefore, the energy of seed pulse being amplified inside the regen was estimated by measuring the energy of the emitted pulse after the Faraday rotator and dividing by a factor of 0.6.

For 23 round trips in the amplifier (Pump power $\sim 7W$), with the intra-cavity etalons in position to provide a broad spectrum, amplified pulse energies measured after the Faraday rotator had a maximum of $\sim 300\mu J$. This gives a pulse energy of $\sim 500\mu J$ during the last round trip in the amplifier.

4.5.2 Simulation of Pulse Widths Inside the Regen

Simulated pulse widths (using the PulseSim.m and DispRegenElements.m simulations) for pulses taking 16 and 23 round trips in the amplifier, including 50 reflections on TOD mirrors, are shown in figure 4.19. The difference in the FWHM between the two simulated pulse shapes (12.5ps and 17ps respectively) indicates that the pulse width increases by $\sim 640fs$ per round trip in the regen.

4.5.3 Calculation of the Cavity B-Integral

The estimates for pulse energies and widths, described above, were used to calculate the intensity within the amplifier cavity and the associated B-integral of the

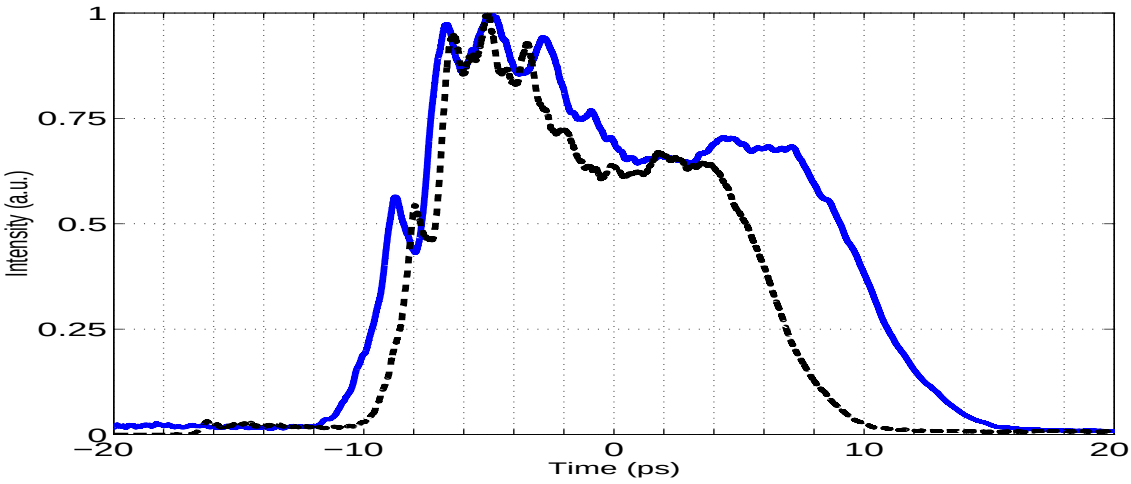

Figure 4.19: Simulated pulse widths for 16 (dashed line) and 23 (solid line) round trips in the amplifier and 40 reflections off of TOD mirrors. The pulse shapes were simulated using 62nm FWHM spectrum in figure 4.14

Component	Beam Radius(μm)	Length(mm)	$n_2(cm^2/W)$
Polarizing Beam Splitter	650	8.4	$3.0X10^{-}16$
Pockels Cell (DKDP)	620	40	$3.0X10^{-}16$
Ti:saph	400	16	$2.5X10^{-}16$
Pockels Cell Windows (Fused Silica)	620	20.3	$3.0X10^{-}16$

Table 4.5: Mode size of the amplified pulse inside each amplifier component and each components length and nonlinear coefficient

amplifier.

The B-Integral was calculated as described in section 2.5.2. The information necessary to complete this calculation included the lengths of the materials used, the nonlinear index of refraction of each material in the regen [25], [30] and the mode size and peak laser power inside each material.

The total calculated B-integral accumulated by the amplified pulse during the last seven round trips is 2.9 as summarized in table 4.5.3. This is just below the upper limit of 3 suggested in [16] (after which point, non-linear phase shifts make pulse compression complicated).

The variation in group delay across the amplified pulse due to non-linear phase shifts was estimated using equation 2.28 [19]. Using the measured spectral width of 29THz (60nm FWHM centered at 800nm) the group delay across the pulse due to a B-integral of 3 is calculated as 16.4 fs.

Round Trip	FWHM (ps)	Energy (μ J)	Peak Power W X 10^6	B-Integral
17	13.2	100	0.8	0.15
18	13.8	180	1.3	0.26
19	14.4	270	1.8	0.37
20	15.1	333	2.2	0.44
21	15.7	423	2.7	0.54
22	16.3	474	2.9	0.58
23	17	500	2.9	0.59
Total				2.9

Table 4.6: Simulated pulse widths of amplified pulses for a given number of cavity round trips completed. The calculated energy, peak power and corresponding b-integral during the given round trip are also shown.

Estimate of Pulse Intensities Producing Damage

Reference [19] gives a damage threshold of $5J/cm^2\tau_p^{\frac{1}{2}}$ where the pulse duration, τ_p, is measured in nanoseconds for a typical optical coating or multilayer dielectric mirror. Therefore for a $10ps$ pulse an estimated damage threshold for optical materials in the regen is estimated as $0.5J/cm^2$. Based on a maximum energy within the amplifier of $500\mu J$ and a minimum mode size of 250μm a maximum energy density inside the regen of $\sim 0.25J/cm^2$ is calculated. Therefore damage to optical elements in the regen should be improbable. However, damage is occasionally observed to take place to the optical elements in the regen and is likely due to a number of factors. For instance, dust migrating into the regen cavity can increase the chance of damage.

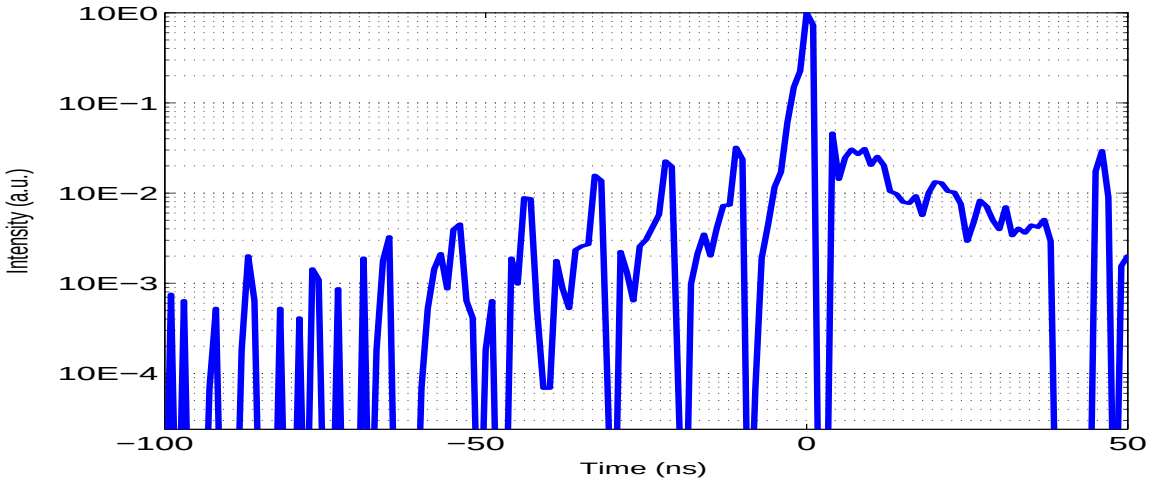

Figure 4.20: A time averaged acquisition of an amplified pulse emerging from the regen. Pre-pulses can be clearly seen to the left of the main pulse.

4.6 Regen Output Characteristics

4.6.1 Pre-Pulses

A known issue with Regenerative amplifiers is the generation of amplified pre-pulses. Pre-pulses are generated due to limitations of the Regen Q-switch. Figure 4.20 shows the temporal landscape around an amplified pulse emitted from the Regen. The pulses shown travel from right to left across the page so the small peaks to the left of the pulse are pre-pulses. A contrast ratio of 30:1 was measured between the peak amplified pulse and next most intense pre-pulse. The dip in the pulse intensity to the right of the amplified pulse is deemed to be associated with ringing in the photo-diode used to measure the pulse intensity. It is noted that a post-pulse is far less damaging to future experiments as the physics to be studied usually occur during interaction with the laser peak power.

4.6.2 Beam Profiles and Divergence

The transverse profile of a laser is necessary information when designing optical systems to manipulate the beam profile. For instance optimal focusing with parabolic mirrors is obtained for laser beams with Gaussian beam profiles.

The beam profile of the amplified pulses emerging from the regen was measured by stepping a slit ($\sim$ 1mm wide) transversely across the pulse and measuring the average energy transmitted through the slit. Beam profiles in both the horizontal and vertical direction were measured and are shown in figure 4.21 showing

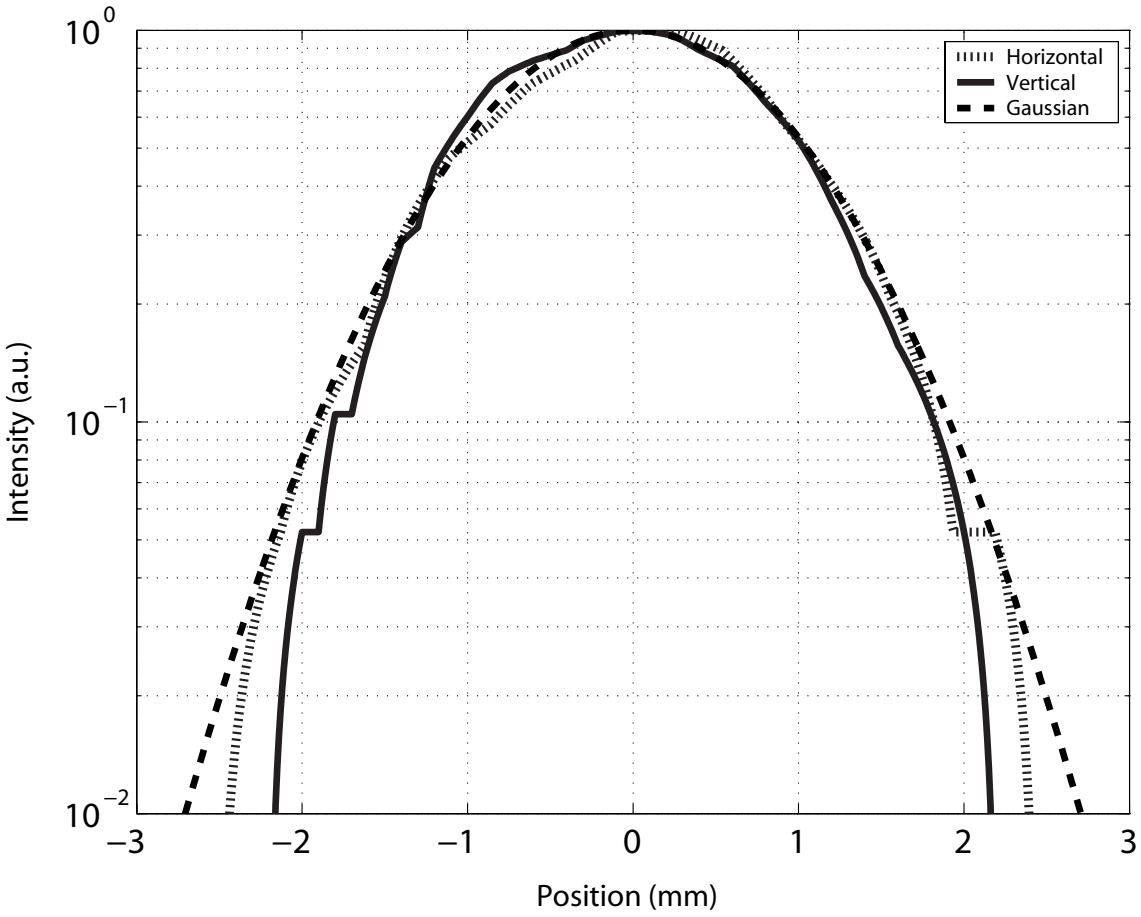

Figure 4.21: Vertical (solid line) and horizontal (dotted line) beam profiles for pulses emitted from the regen. A Gaussian (dashed line) with a similar width is shown as comparison.

a near Guassian shape. As a comparison, the beam profile of the oscillator pulses, showing a strong ellipticity, is shown in figure 4.22.

The divergence of pulses out of the amplifier was determined by measuring the beam profile of pulses emitted from the regen at two positions, separated by a distance of 2 meters. Using the $1/e^2$ intensity points, of the measured beam profiles, the divergence of pulses emerging from the regen was calculated to be $0.025 mrad$.

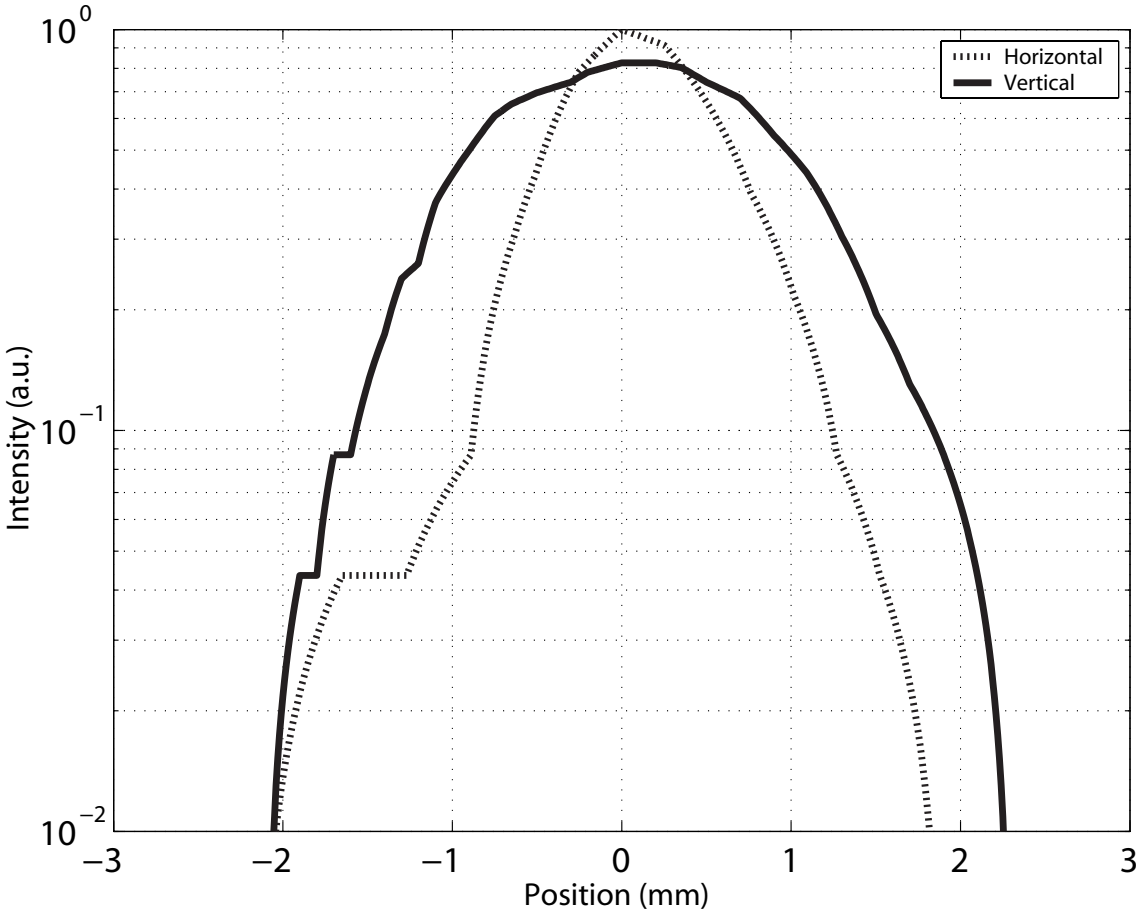

Figure 4.22: Vertical (solid line) and horizontal (dotted line) beam profiles for seed pulses sent into the regen.

Chapter 5

Dispersion Compensation

5.1 Introduction

Many CPA systems use stretching and compression systems built with diffraction gratings [5]. The use of diffraction gratings provides large amounts of dispersion within a relatively small space. Alternatively to grating based systems, pulse stretching can be achieved by taking advantage of the positive dispersion inherent in most optical materials (2.3.1). In order to compress a pulse however, an optical system that produces a net negative dispersion equal in magnitude to the positive dispersion, acquired during the stretching and amplification stages, is required. Prism based compressors are the only practical alternative to grating based compressors capable of providing the large negative dispersions required.

A distinct disadvantage of prism pair compressors is the amount of dispersion that they are capable of producing ($\sim$10 to 100 times less than grating compressors) thus limiting the amount that a pulse can be stretched before amplification. However prism-pair compressors generally have a higher throughput ($\sim$ 85%) than grating based compressors ($\sim$ 60%). In addition to which grating based systems are more susceptible to damage and more difficult to maintain than prism-pairs.

5.2 Theoretical Description of the Prism Pair Compressor

In section 2.3.2 a general formulation derived by Fork et al. for calculating the GVD resulting from a dispersive prism pair arrangement, given the optical path length $P(\lambda)$, is presented. Due to the large bandwidths of present day ultrafast laser systems a calculation of the GVD over the entire spectrum of the pulse is required in order to ensure optimal dispersion compensation can be achieved. The authors of [31] expand on the formulation of Fork et al. to give a general expression for the GVD as a function of wavelength (including the positive dispersion due to

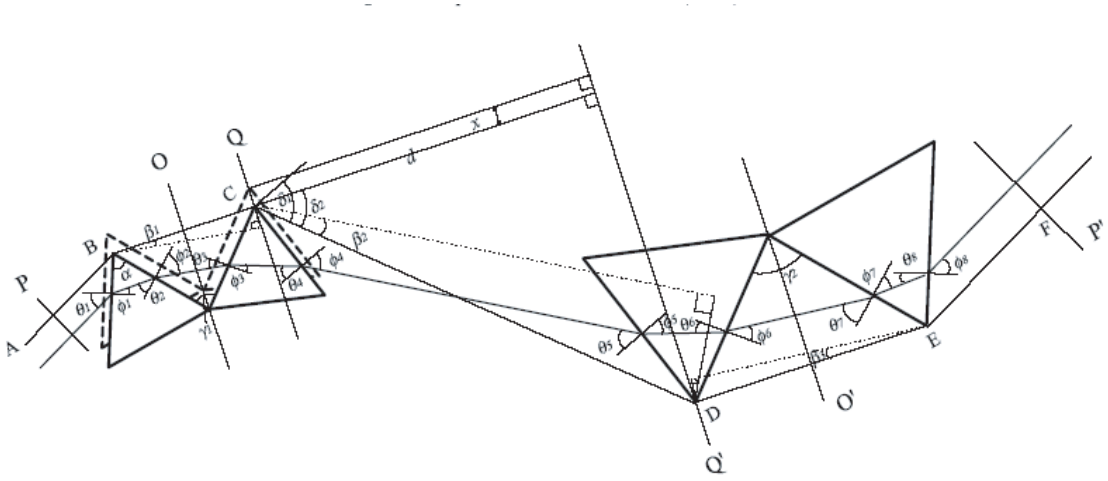

Figure 5.1: The double prism compressor as presented in reference [31]

the prism material and the effect of insertion of the prism pairs) for a pair of double prisms cut with an arbitrary apex angle, α.

$$\frac{d^2P(\lambda)}{d\lambda^2} =$$
$$(BC+DE)\{\frac{d^2\phi_2(\lambda)}{d\lambda^2}\sin[\theta_1-\phi_2(\lambda)]-[\frac{d\phi_2(\lambda)}{d\lambda}]^2\cos[\theta_1-\phi_2(\lambda)]\}+$$
$$CD\{\frac{d^2\phi_4(\lambda)}{d\lambda^2}\sin[\delta_1-\phi_4(\lambda)]-[\frac{d\phi_4(\lambda)}{d\lambda}]^2\cos[\delta_1-\phi_4(\lambda)]\} \tag{5.1}$$

Where the angles ϕ and θ are angles made by the incident light with the prism face normals as indicated in figure 5.1, and are derived using Snell's law. The lengths $\boldsymbol{BC}$, $\boldsymbol{CD}$ and $\boldsymbol{DE}$, in the diagram, are a function of the prism sizes and angles of separation. For Brewster cut prisms, an angle of $\boldsymbol{2\theta_B}$ is set between the prisms in each pair. The angle δ_2 is the angle made between the apexes $\boldsymbol{C}$ and $\boldsymbol{D}$ with respect to the perpendicular line, of length $\boldsymbol{d}$, between plane $\boldsymbol{Q}$, starting at apex $\boldsymbol{C}$, and the parallel plane $\boldsymbol{Q'}$. The length $\boldsymbol{l_2}$ is related to the angle δ_2 and the distance $\boldsymbol{d}$:

$$\cos(\delta_2) = \frac{d}{l_2} \tag{5.2}$$

The 'principal arrangement' of the compressor system is defined as the arrangement of minimum deviation, where the incident light travels along a path $\boldsymbol{ABCDEF}$. In the principal arrangement, the angle δ_2 reduces to $2\theta_1 - \alpha$. This situation is highly unrealistic as it would require the incident beam size to be infinitely

small. In addition to which, only the central wavelength would pass through the system in this arrangement as longer wavelengths would diverge above the apex of prism 2 and shorter wavelengths would diverge below the apex of prism 3. In order to account for this the authors of reference [31] include an additional parameter for the angle δ_2 for a given translation of, distance x, of a set of prisms along the axis O or O':

$$\delta_2 = 2\theta_1 - \alpha \rightarrow \arctan\left(\frac{(d\tan(2\theta_1 - \alpha) + x)}{d}\right) \tag{5.3}$$

Insertion of the first set of prisms away from the principle arrangement determines the maximum wavelength that can pass through the system while insertion of the second set of prisms away from the principle arrangement determines the minimum wavelength that can pass through the system. It is important to note that in order to compress pulses with large bandwidths increasingly large insertion distances, away from the principle arrangement, are required in order to pass the entire bandwidth of the pulse. This increases the amount of total material dispersion (positive dispersion) produced by the system and hence ultimately puts an limit on the negative dispersion that a given prism compressor system can produce over a given bandwidth.

5.3 Prism Pair Compressor Simulation

A simulation, PrismComp.xmcd, was written in the MathCad programming language by Dr. Xiaoming Sun, utilizing the mathematical model presented above. The simulation was written in order to determine a prism compressor arrangement suitable for compensating dispersion from the amplifier system. A dispersion equation for the prism glass (LakN16), the length of the prism faces (55 mm and 90 mm) and apex angle (Brewster cut for 800nm) were used in order to represent the prism compressor used in the laboratory. The simulation accepted as free parameters the perpendicular distance, d, between the pairs of prisms and the maximum and minimum wavelengths to be passed by the prism compressor, related to the insertion parameter x in equation 5.3.

Simulated dispersion profiles (GVD as a function of λ) for pulses emerging from the amplifier, as discussed in section , and the functionality to add or remove dispersion due to a variable number of TOD mirror reflections, was integrated into the prism compressor simulation so that a total dispersion profile for pulses emerging from the compressor could be determined with each run of the simulation.

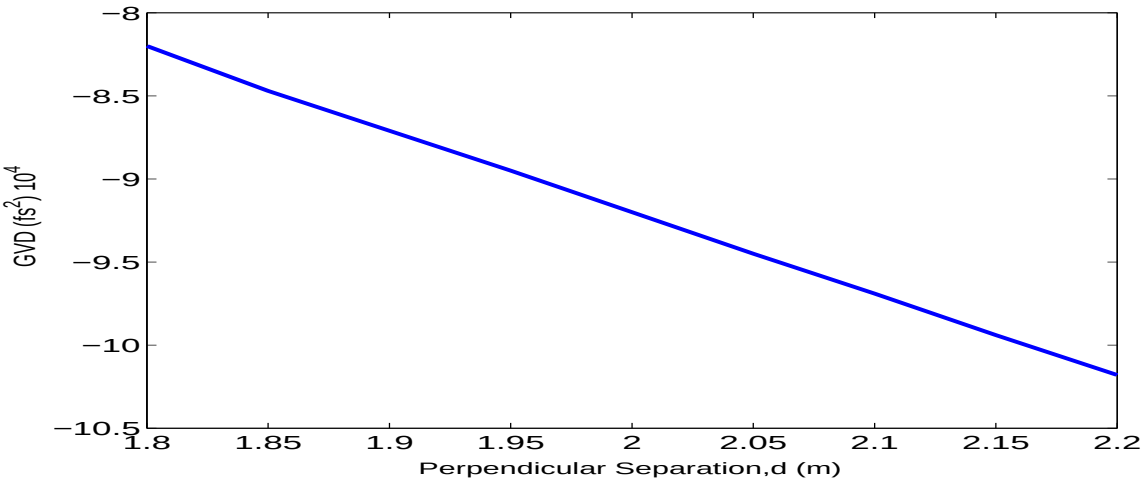

Figure 5.2: The GVD provided by the prism compressor for variations in perpendicular separation d with constant insertion parameters $\lambda_{min} = 740nm$ and $\lambda_{max} = 4000nm$

5.3.1 Simulation Results

As a first estimate of the dispersive capabilities of the compressor, values of $\sim -25fs^2/mm$ per mm of separation and $\sim -720fs^2/mm$ ($\sim -430Fs^2/nm$) of insertion of the last pair of prisms (P34 in figure 5.8) were determined using the simulation. The change in GVD, at a central wavelength ($800nm$), as a function of prism separation and minimum wavelengths passed by the last set of prism, are summarized in figures 5.2 and 5.3 respectively.

In a first step to determine the configuration of the prism compressor required to compensate for the dispersion of pulses emerging from the regen, a minimum wavelength of 740nm and a maximum wavelength of 850nm were used as input parameters. Simulation results suggested that a prism separation of d = 1.75m was required to compensate for the dispersion from the regen and TOD mirrors. Setting up the compressor in this configuration revealed that the first two prisms required ~2.2cm (or $\boldsymbol{\lambda_{max} = 4000nm}$) of insertion in order to facilitate the passage of the entire beam through the prism compressor apparatus. The added insertion was required due to the non-zero divergence, and finite beam size of pulses emerging from the regen [1]

Using the insertion parameters of λ_{min} = 740nm and λ_{max} = 4000nm a prism compressor configuration with a perpendicular distance d=2m was determined to

[1] The effects of non-zero beam divergence on the system dispersion could be investigated by simulating the dispersion for two different trajectories, separated by the largest angle, within the cone of light making up the incident radiation. Similarly the effect of non-zero beam size on system dispersion could be investigated

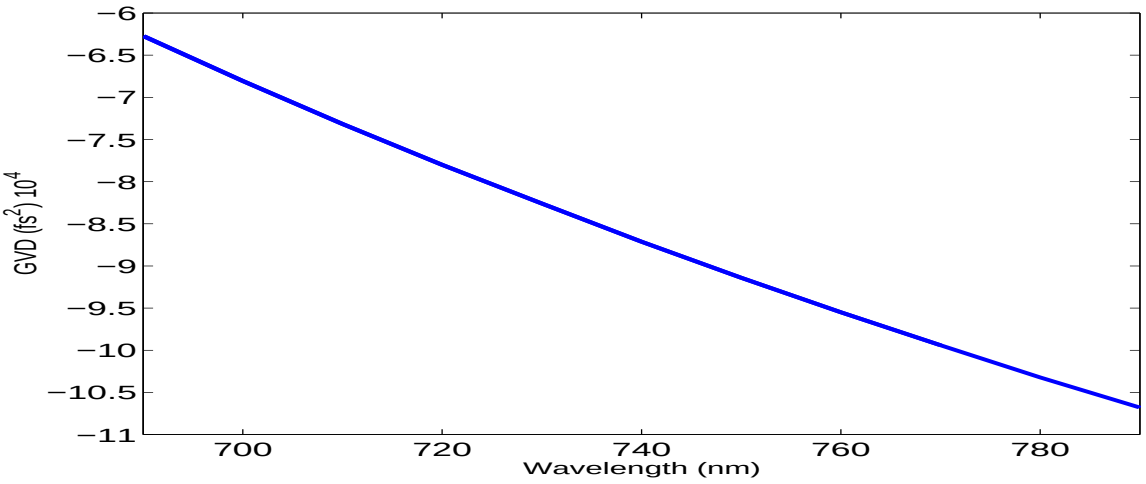

Figure 5.3: The GVD provided by the prism compressor for variations in the insertion parameter λ_{min} with constant insertion parameter $\lambda_{max} = 4000nm$ and perpendicular separation $d = 2m$

give a nearly flat GVD profile over the spectral region of the pulses emitted from the regen as summarized in figures 5.4 and 5.5. The expected compressed pulse shape was simulated using the simulated GVD profile and measured spectrum shown in figure 5.5 and produced an expected pulse width of $< 30fs$ FWHM as shown in figure 5.6. The bandwidth limited pulse width for the given spectrum was simulated to be $\sim 16fs$ FWHM.

A beam profile for the pulses exiting the compressor under these conditions is shown in figure 5.7

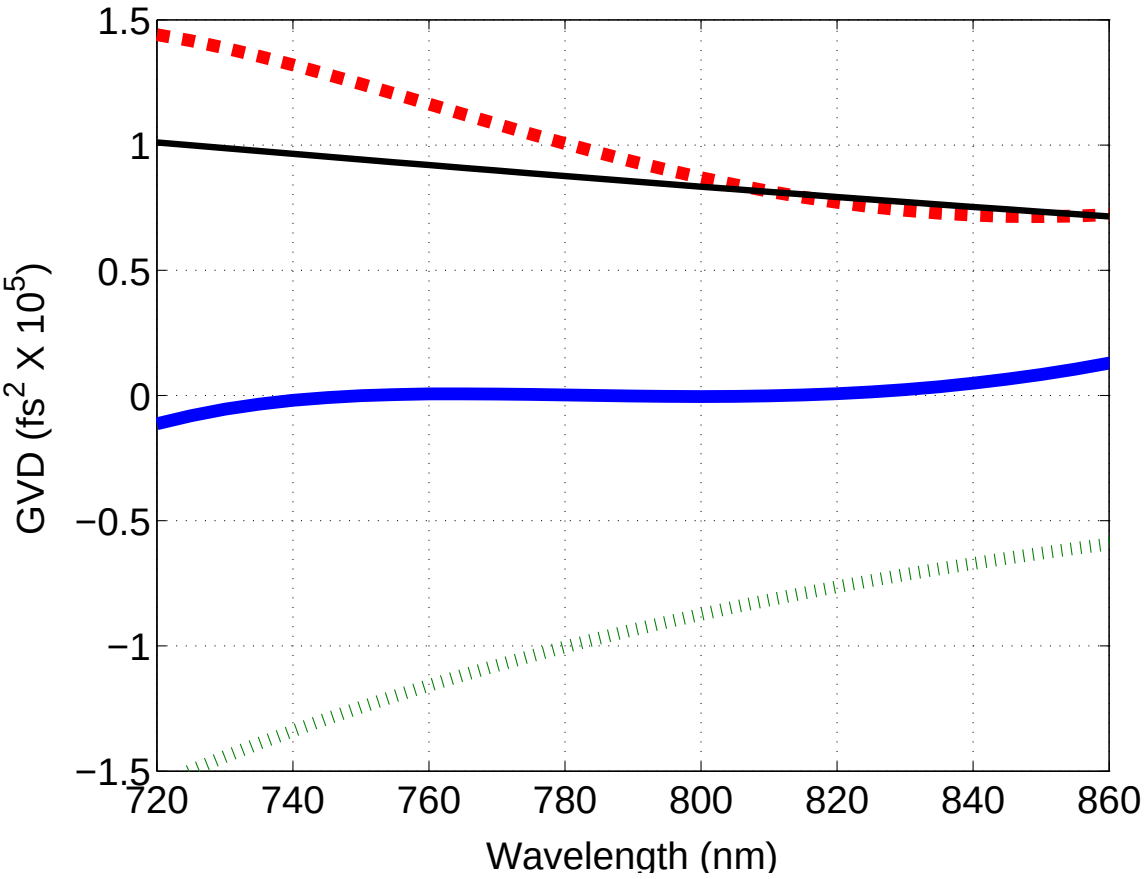

Figure 5.4: Prism compressor simulation results showing the total amount of dispersion due to 50 reflections from the TOD mirrors and 23 round trips in the regen (dashed line), the total dispersion from the prism compressor using the insertion parameters λ_{min} = 740nm and λ_{max} = 4000nm and a separation of 2 meters (dotted line) and the total system dispersion on exiting the compressor (thick solid line). The GVD profile for 23 round trips in the regen alone (thin solid line), without TOD mirror dispersion, is shown illustrating the need for the extra TOD dispersion.

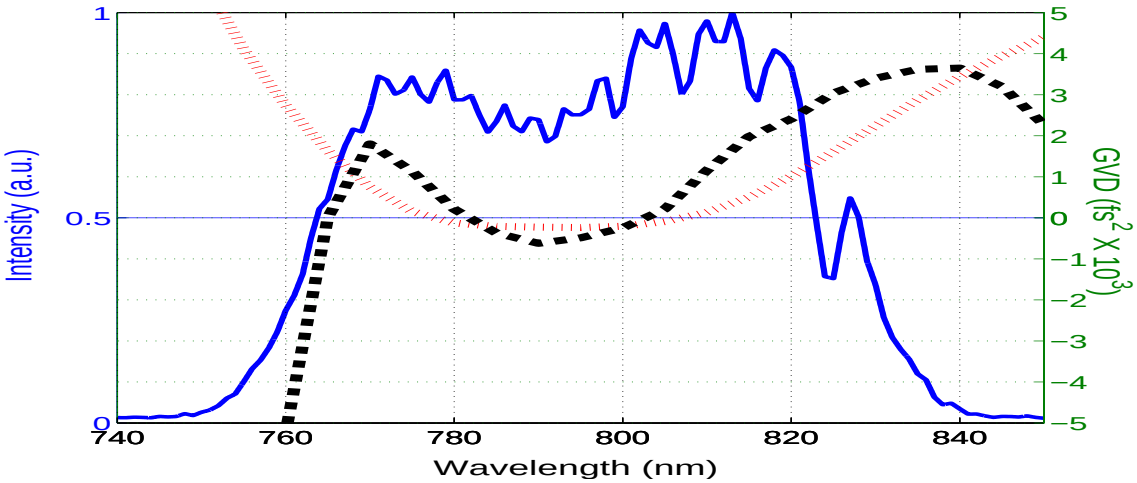

Figure 5.5: The simulated dispersion compensated GVD profile where the TOD mirror GVD profile was represented by the manufacturers average specifications (dotted line) and a measured GVD curve, provided by the manufacturer, for a standard TOD mirror (dashed line). The spectrum from the regen is also shown (solid line)

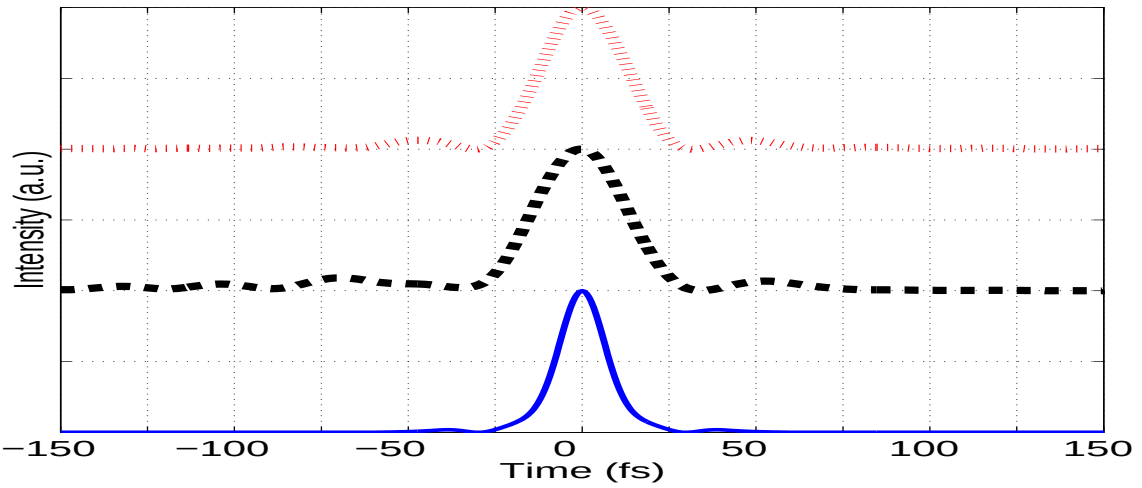

Figure 5.6: Simulated pulse shapes given the GVD profiles and measured spectrum from figure 5.5 (where the line types correspond) and the bandwidth limited pulse shape (solid line). The simulated pulse shapes using the prism compressor GVD profiles both have a FWHM of $< 30fs$ while the BWL pulse has a FWHM of $\sim$16fs

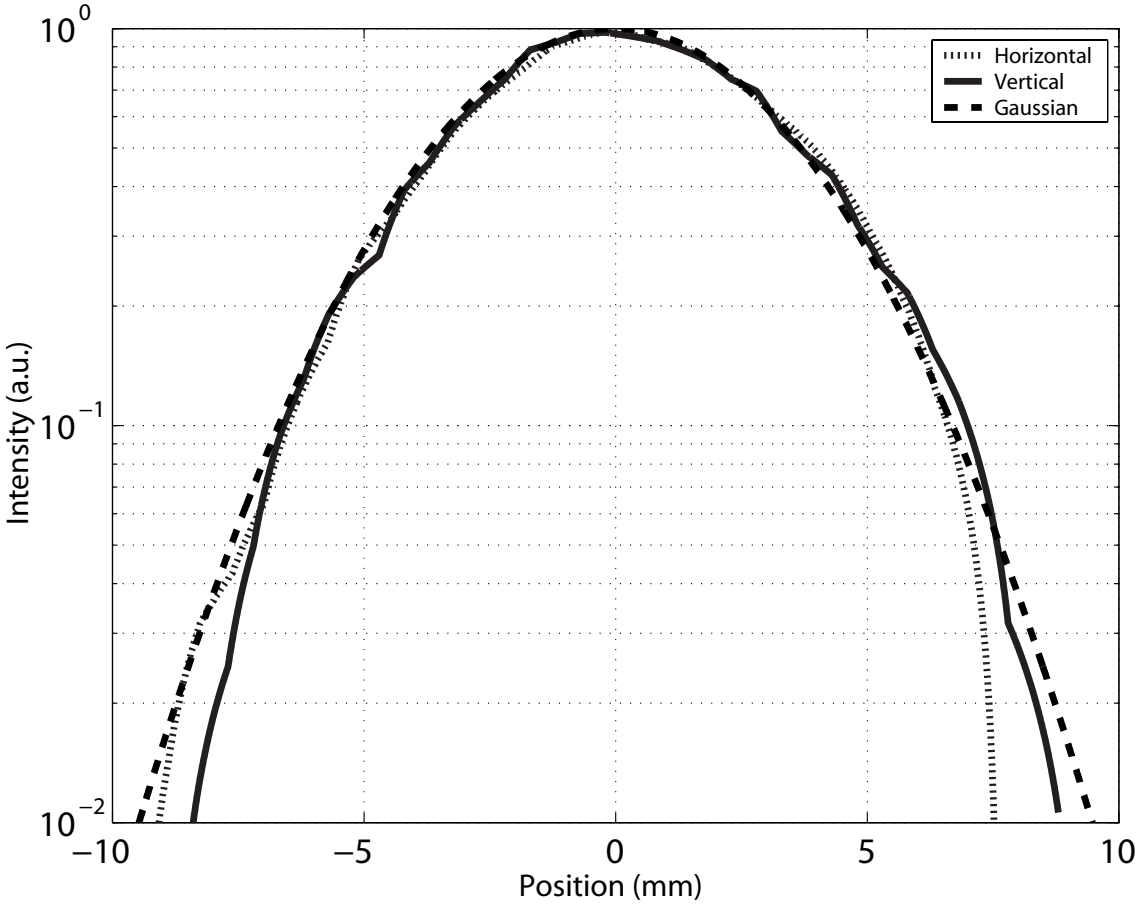

Figure 5.7: Vertical (solid line) and horizontal (dotted line) beam profiles for pulses emitted from the Compressor. A Gaussian (dashed line) with a similar width is shown as comparison.

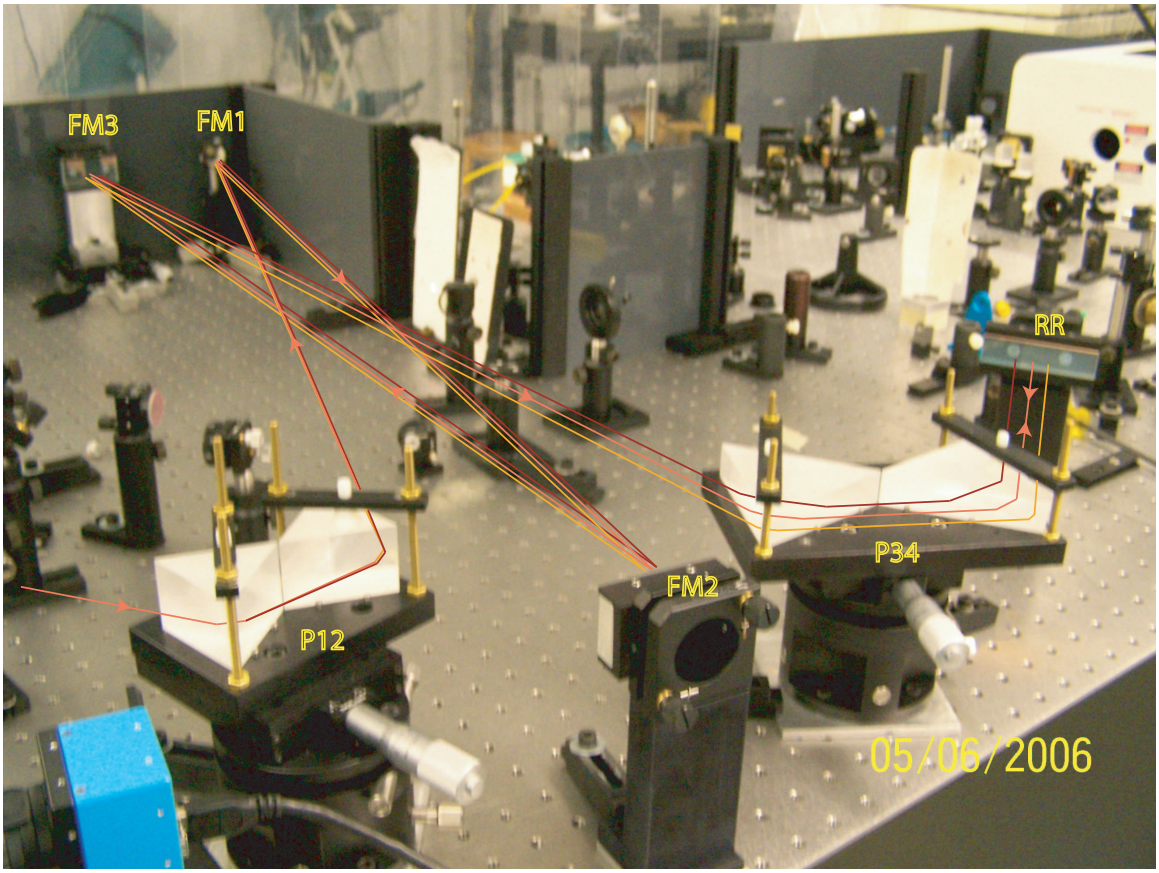

Figure 5.8: The prism compressor setup used in the laboratory, with; folding mirrors FM1, FM2 and FM3, retro reflecting mirror RR, and prism pairs P12 and P34.

5.4 Experimental Procedure

The prism compressor was constructed using two prism pairs purchased on special order from Femtolasers Inc. The prisms were made from LakN16 glass (see appendix A) and Brewster cut for an incident angle of 800 nm (60.32^o). LakN16 glass was chosen because it provides a large amount of negative GVD and relatively small amount of negative TOD, compared to other glasses [15], when set up as a prism compressor.

The prisms pairs (P12 and P34 in the diagram) were mounted on specially designed plates built in the UW machine shop. In order to ensure that the prisms were mounted with the correct geometry a number of pins were mounted on the plate such that when the prism faces were pressed against the pins there was an angle of $\gamma = 2\alpha$ between the prisms. The prism plates were mounted on translation stages such that translation was made towards the prism apex thus maintaining

the angle between an incoming pulse and prism face. The translation stages were also mounted on stable rotation mounts that provided two axes of tilt and an axis of rotation perpendicular to the base of the mount. The tilt controls on the rotation stages allowed the prisms to be leveled such that an incoming pulse would experience minimal spatial chirp in the vertical plane. The axis of rotation was used to arrange the prisms for Brewster angle incidence. This condition was maintained by rotating a prism pair such that the reflection off of a prism face was seen to be minimal when viewed with an IR viewer. The importance of maintaining the Brewster angle alignment is discussed in more detail later.

Three folding mirrors (1 - Thorlabs BB1-E03, 2 - FemtoLasers VO111,) and a retro reflection mirror (FemtoLasers VO032) were used to steer pulses through the prism compressor system (FM1,FM2,FM3 and RR in the diagram, respectively). The mirrors were coated with a broad band high reflection coating centered at 790nm and were designed for reflection near 0^0. The folding mirrors were used in order to reduce the amount of space required by the compressor system on the optical table while maintaining large prism separation distances.

In order to facilitate control over the prism separation folding mirror FM3 was mounted on a translation stage as shown in figure 5.8. The retro-reflecting mirror, RR, was used to steer the beam back through the prism compressor, directly overtop of the incoming beam. In order to spatially separate the returning pulse from incoming pulses after exiting the prism compressor a small vertical adjustment was applied to the retro-reflecting mirror. The spatial chirp of pulses emerging from the prism compressor was monitored by scanning a spectrometer transversely across the beam profile. Minimization of the spatial chirp was determined to be a critical factor in compressing pulses and is discussed in further detail later.

Three irises separated by $\sim$1m each were centered on pulses exiting the prism compressor to ensure that the same part of each compressed pulse could be measured for different arrangements of the prism compressor. This was done to ensure that any spatial chirp effects would be negligible in the part of the beam being sampled for autocorrelation.

Before introducing the results of the compression experiments the theory behind the devices used to characterize the compressed pulse widths, and their operation in the laboratory, is first explained.

Chapter 6

Pulse Characterization

6.1 Introduction

Pulse characterization is an essential part of ultrafast laser science. For most experiments it is desirable at least to know and vary the intensity of pulses. A complete characterization of the pulse being used however is ultimately more useful so that the effect of different pulse shapes on the physics to be studied can be quantified. For cases in which maximum pulse intensity is desired knowing the pulse shape is crucial information in order to better compress the pulse.

To completely reconstruct the electric field of an optical signal either knowledge of the temporal intensity and phase or the spectral intensity and phase is required as illustrated in sections 2.1.2 and 2.1.3 respectively.

6.2 Temporal Measurement

The rate of oscillation of the pulses considered here extends from approximately $\mathbf{300 \cdot 10^{12}}$ to $\mathbf{400 \cdot 10^{12}}$ cycles per second. In order to temporally resolve this signal a detector bandwidth at twice this frequency ($\sim \mathbf{10^{15} Hz}$) is required by the Nyquist theorem. Unfortunately the current state-of-the-art in detector technology doesn't provide enough bandwidth to resolve these signals. On the time scale of the carrier envelope of an ultrafast pulse ($\sim \mathbf{100 fs}$), linear detectors such as photo-diodes and photo-multipliers can be considered to have infinitely slow response times ($\sim \mathbf{1ns - 1ps}$). Therefore, not only is it impossible to make a direct measurement of phase with a linear detector, it is also impossible to measure the temporal width of an ultrafast pulse by the same method.

Instead of a measure of pulse intensity, for an ultrafast pulse, a slow linear detector returns a measure of the average intensity (the energy) over the response time of the detector. To obtain a measure of the pulse intensity for an ultrafast pulse, a detector with a response that varies non-linearly with the intensity of the

pulse can be used.

$$Signal_{nonlinear} \propto I^2 \tag{6.1}$$

Although no pulse shape or temporal width can be implied from a single one dimensional measurement of I^2, a relative indication of pulse width can be obtained by comparing I^2 and energy measurements. It is noted that a nonlinear detector is also a slow detector, and hence no resolution of the phase is possible.

6.3 Measurement in the Frequency Domain

Frequency domain measurements are performed with a spectrometer. A spectrometer provides spectral intensity information by spatially dispersing the frequency content of a signal and measuring the intensity of the dispersed frequencies separately. Similarly to time domain measurements a spectrometer is incapable of returning spectral phase information.

6.4 Methods of Pulse Characterization

The most crude way of characterizing a pulse is with a combination of a linear and non-linear detector, as described above. In order to obtain a quantifiable value for pulse duration more sophisticated methods of pulse characterization are required. The simplest pulse duration diagnostic to implement is the cross correlation. Cross correlations involve gradually delaying (in time) a well known 'probe' pulse with respect to a 'test' pulse, to be characterized, and overlapping the two on a detector that is sensitive to I^2. A disadvantage of this techniques is that it requires a shorter pulse than the pulse to be characterized. To overcome this, self-referencing variations on the cross correlation, such intensity and interferometric autocorrelation (IAC) [32] and single shot autocorrelation [18], have been developed and are widely used to diagnose pulse shapes. Although easy to implement a disadvantage of autocorrelation techniques is their inherent symmetry, which wipes out any information about the pulse asymmetry. Furthermore pulse shapes retrieved from an autocorrelation can be ambiguous as it has been shown that many different pulse shapes may reproduce the same autocorrelation trace [33]. Third order autocorrelations (TOAD) [18] (measuring I^3) are sensitive to pulse asymmetries. However a TOAD requires a detection schemes with greater sensitivity, than the schemes that measure I^2, and materials that are transparent to the third-harmonic of the fundamental.

In order to completely characterize a pulse, diagnostic techniques that can reconstruct the temporal or spectral phase of a pulse are needed. Currently the two

most popular techniques that provide this ability are Frequency Resolved Optical Gating (FROG) [13] and Spectral Phase Interferometry for Direct Electric Field Reconstruction (SPIDER) [34].

In the FROG technique the spectrum of the test pulse is measured as a function of delay between the test pulse and a 'gating' pulse. By manipulating the polarization of the gating and test pulses the spectral content due to the overlap between the two pulses in a non-linear medium can be isolated. The FROG produces a 2 dimensional plot of time and frequency versus intensity from which the test pulse phase can be retrieved by an iterative Fourier-transform algorithm. One disadvantage of the FROG technique is that it requires the use of an iterative algorithm to recover a pulse shape from the experimental results. The iterative pulse retrieval algorithm used in FROG gives slower pulse shape retrieval times compared to other pulse characterization techniques such as SPIDER. However, great advances have recently been made with techniques based on the FROG concept such as the GRENOUILLE technique [35], reinforcing the importance of FROG in ultrafast laser pulse characterization.

The SPIDER technique, in contrast to the FROG technique, uses an algebraic algorithm to retrieve the pulse shape from measured results, allowing for real time data analysis [36]. The SPIDER technique is a variation on spectral interferometry that involves the spectral interference of a test pulse and a spectrally shifted, or sheared, pulse replica. The phase of the test pulse is retrieved from the spectral interference pattern between the test and replica pulses through a non-iterative Fourier transform inversion and filtering routine. The SPIDER technique has gained wide acceptance and many variations on the technique have been developed for specific applications. Some of these applications include the measurement of ultra-weak pulses (HOT-SPIDER) [37], few-cycle pulses [38], ultra-violet pulses (ZAP-SPIDER) [39], single pulses [40] and complete spatio-temporal profiling of a pulse [41].

The pulse characterization techniques used in this thesis include non-linear detection, interferometric autocorrelation and SPIDER. A further description of the theory behind these techniques and the use of the devices is presented next.

6.4.1 Non-linear Detection Schemes

In order to obtain a measurement of the temporal width of an ultrafast pulse, a detection scheme that is sensitive to I^2 is necessary, as discussed above. Two simple techniques exist to perform this measurement.

Non-linear Crystal and Detector Scheme

This technique involves the use of a negative uni-axial nonlinear crystal coupled with a filter to remove the fundamental frequency and a linear photodiode to mea-

sure the intensity of the SHG (see section 2.5.1) produced in the nonlinear crystal.

The amount of SHG generated is proportional to the thickness of the crystal whereas the phase matching bandwidth is inversely proportional to crystal thickness. This relationship makes the use of very thin ($\sim 100\mu$m) crystals necessary in order to obtain an accurate measurement of the I^2 of short pulses ($\sim 20fs$). Phase matching is discussed in further detail in section 2.5.1.

2-photon Diode

A 2-photon diode is a semiconductor photodiode with a bandgap of energies centered at the second harmonic of the signal to be measured. Hence a 2-photon diode is in fact a linear diode that is used outside of it's linear response range. A 2-photon diode gives a signal proportional to I^2 by requiring two photons at of frequency $\omega_0/2$, (where ω_0 is within the linear range of the photodiode) to be incident simultaneously on the photodiode surface in order to bridge the bandgap, of the semiconductor in the photodiode, as shown in figure 6.1.

With the addition of a low-noise signal amplifier a 2-photon diode can be used to measure pulse widths as short as 6 fs using an autocorrelation technique [42].

A 2-photon diode was built using a GaAsP semiconductor photodiode (Hammamatsu G1115) and a low-noise amplification circuit (see appendix C) with a bandgap of energies centered near the second harmonic of the pulse to be measured. Figure 6.1 indicates that the G1115 diode has a linear response in the spectral region 300nm to 680nm. The frequency doubled spectrum of the oscillator is shown overlayed with the linear response of the photodiode in figure 6.1, indicating that the photodiode is capable of giving a measurement of I^2 across the entire bandwidth of the oscillator and amplified pulses.

The response of the 2-photon diode against incident intensity was measured by focusing pulses from the oscillator ($\sim 15fs$ FWHM) onto the diode surface using an off-axis parabolic mirror (Femtolasers OA175, f=5cm). The energy in the oscillator pulses was gradually attenuated with a neutral density filter and measurements made with both, a power meter(Ophir AN/2), to obtain a measurement of the pulse energy, and the 2-photon diode, to obtain a measurement of I^2. A plot of average power vs 2-photon diode response was generated and is shown in figure 6.2, where the quadratic response of the 2-photon diode against average power (energy) can be seen.

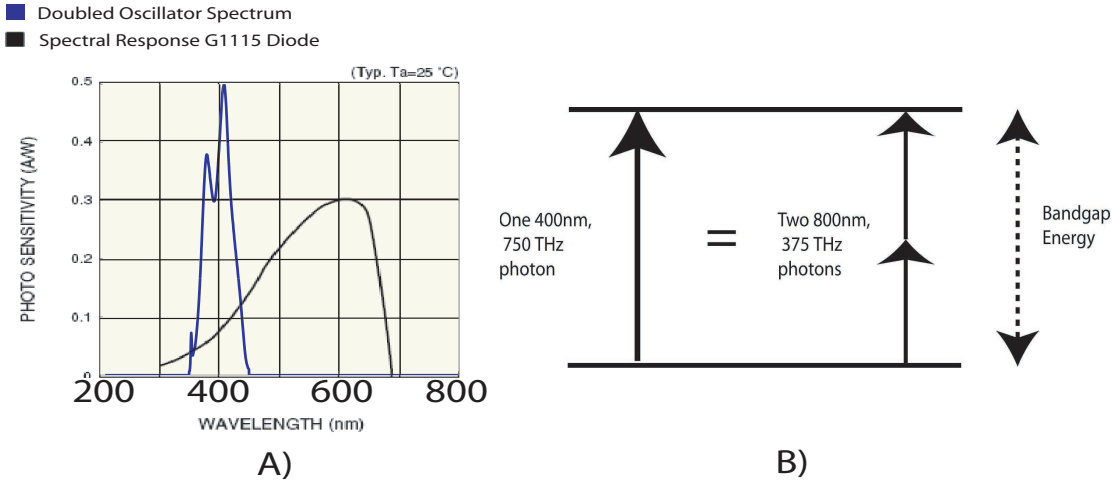

Figure 6.1: A) The quoted spectral response of the Hammamatsu G1115 photodiode overlayed with the theoretical doubled spectrum of the oscillator pulses. B) A toy model of the bandgap of a semiconductor. Two photons at 800nm that are incident on the semiconductor can combine simultaneously on the diode surface to overcome a bandgap energy equal to the energy of a single photon at 400nm

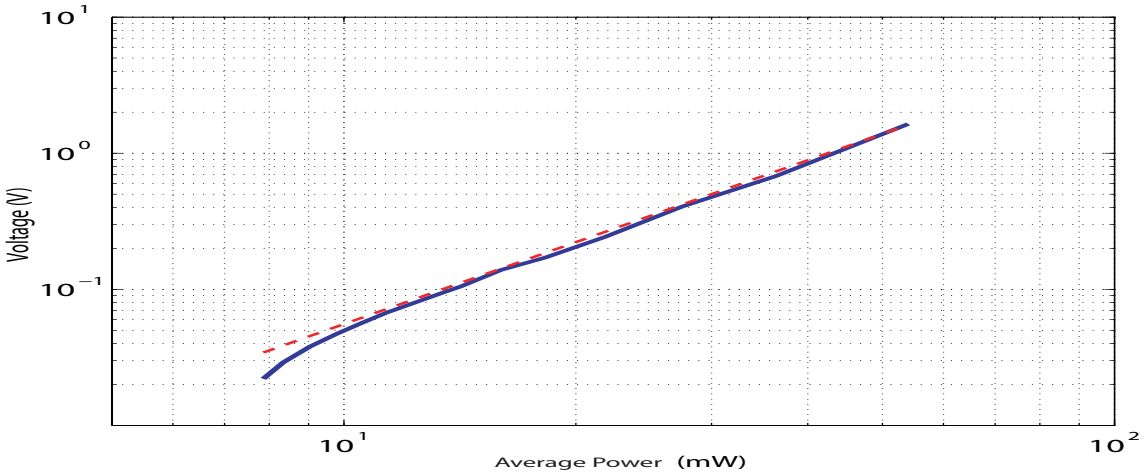

Figure 6.2: The quadratic response of the 2-photon diode plotted against average power for pulses from the oscillator (solid line). A curve of $Energy^2$ vs $Energy$ (dashed line), where the average power is divided by the repetition rate of the oscillator and multiplied by a linear calibration factor, is shown for comparison.

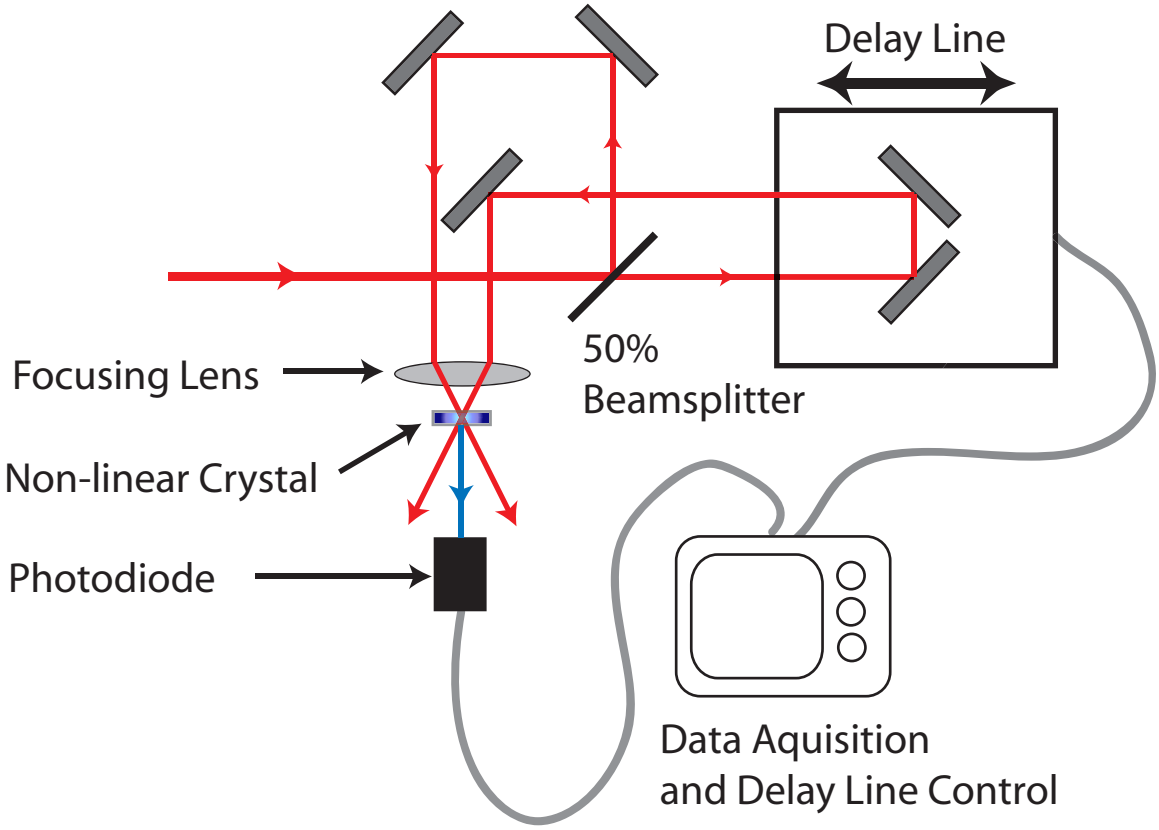

Figure 6.3: The general arrangement for an intensity autocorrelator. The pulse replicas enter into a non-linear crystal, producing SHG, non-collinearly so that a background free signal is produced at the detector

6.4.2 Autocorrelation

In an intensity autocorrelation the test pulse is split into two pulse replicas. One of the replicas is gradually delayed in time and the I^2 produced by overlapping the pulse replicas in a non-linear crystal is measured as shown in figure 6.3. Mathematically an intensity autocorrelation is given by:

$$AC^{(2)}_{intensity}(\tau) = \int_{-\infty}^{\infty} I(t)I(t-\tau)dt \tag{6.2}$$

Where τ is the time delay between the pulse replicas. Due to it's self-referencing nature an intensity autocorrelation always produces a symmetric trace, as described above. The intensity autocorrelation filters out any background signal (produced by a single pulse replica) by using a non-collinear geometry as shown in the figure.

A variation of this technique is called an interferometric autocorrelation (IAC). In an IAC the two pulses are sent collinearly into a nonlinear detector as shown in

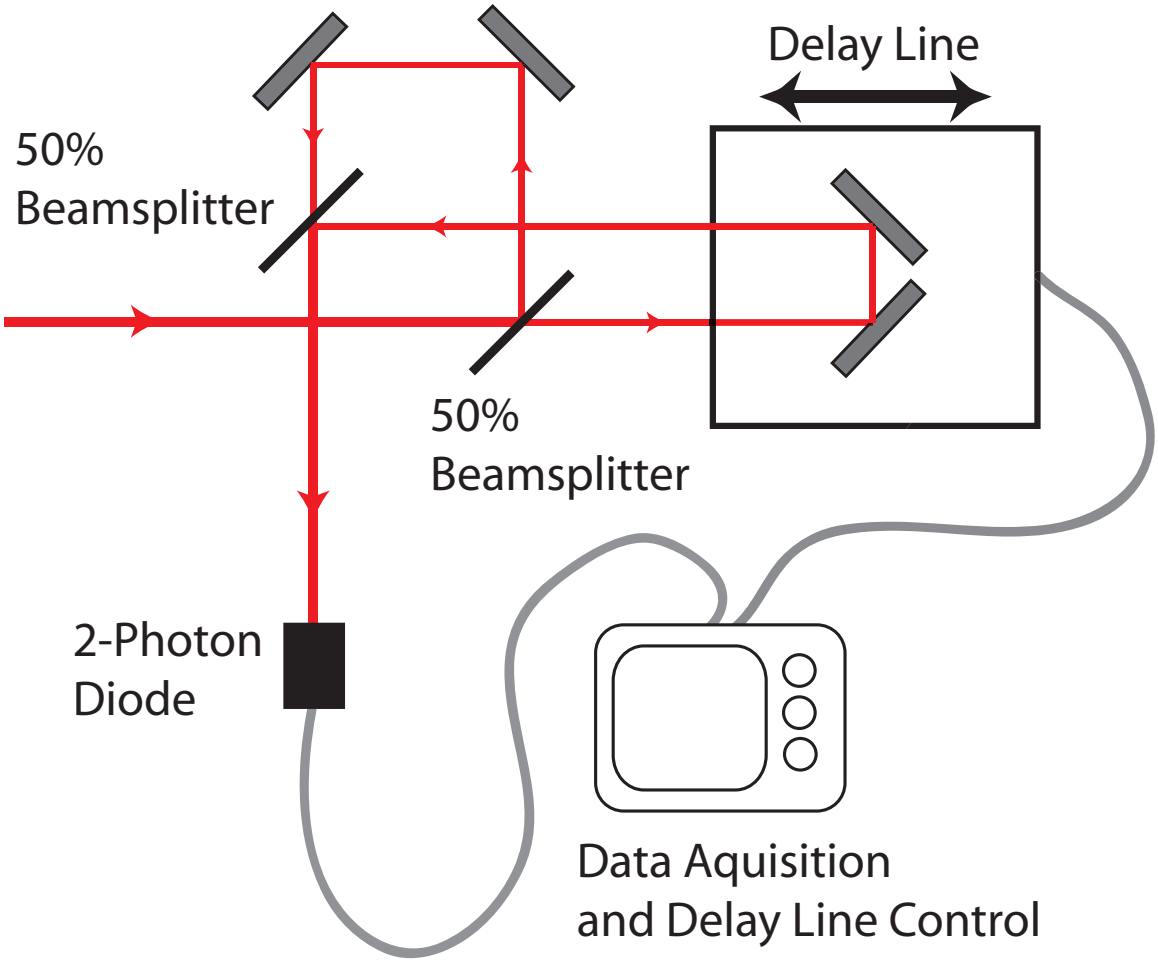

Figure 6.4: The general arrangement for an interferometric autocorrelator. The pulse replicas are aligned collinearly so that interference, as well as the generation of SHG, takes place when the pulses temporally overlap at the detector (a 2-photon diode in this case).

figure 6.4. Mathematically, the signal produced by interferometric autocorrelation is given by:

$$AC^{(2)}_{interferometric}(\tau) = \int_{-\infty}^{\infty} |[E(t) + E(t-\tau)]^2|^2 dt \tag{6.3}$$

multiplying this out gives:

$$
\begin{aligned}
AC^{(2)}_{interferometric}(\tau) = \\
\int_{-\infty}^{\infty} I^2(t) + I^2(t-\tau)dt \quad \textbf{Constant Background} \\
+4\int_{-\infty}^{\infty} I(t)I(t-\tau)dt \quad \textbf{Intensity Autocorrelation} \\
+2\int_{-\infty}^{\infty} [I(t)+I(t-\tau)]E(t)E^*(t-\tau)dt + c.c. \quad \textbf{Oscillates at } \omega \\
+\int_{-\infty}^{\infty} E^2(t)E^*(t-\tau)dt + c.c. \quad \textbf{Oscillates at } 2\omega
\end{aligned}
\tag{6.4}
$$

In addition to the autocorrelation signal, given by equation 6.2, two interference terms, one oscillating at the fundamental, ω, the other at 2ω, as well as a constant background signal are observed as shown in equation 6.10. A result of equation 6.10 is that an interferometric autocorrelation trace should have a peak to background ratio of 8:1. As with all autocorrelation signals the interferometric autocorrelation should also be symmetric.

Simulated IAC Traces

In order to gain the ability to interpret IAC traces correctly an IAC trace simulation, 'ACIntf.m' was written in the MatLab programming language as an extension of the pulse width simulation described in section 3. The effects on an IAC trace due to both GVD and TOD were simulated and the results are illustrated in figures 6.5, 6.6, 6.7 and 6.8.

By looking at the wings of the IAC trace an indication of deviation of the pulse from transform limit and the relative amount of GVD and TOD inherent in the pulse spectral phase determined. It is noted however that the sign of the GVD and TOD can not be determined by analysis of an IAC trace due to the symmetric nature of the IAC.

Experimental Procedure

An IAC was designed and built (figure 6.9) for the purpose of determining the widths of pulses emerging from both the CPA system and the oscillator and, in future experiments, few-cycle pulses from a hollow fibre setup. The IAC was designed using all reflective optics in order to minimize dispersion with the exception of a beamsplitter used to produce the pulse replicas. To equalize the dispersion in each arm of the IAC a 'dispersion compensating' beamsplitter designed for autocorrelation of very short pulses was used (Femtolasers FO002).

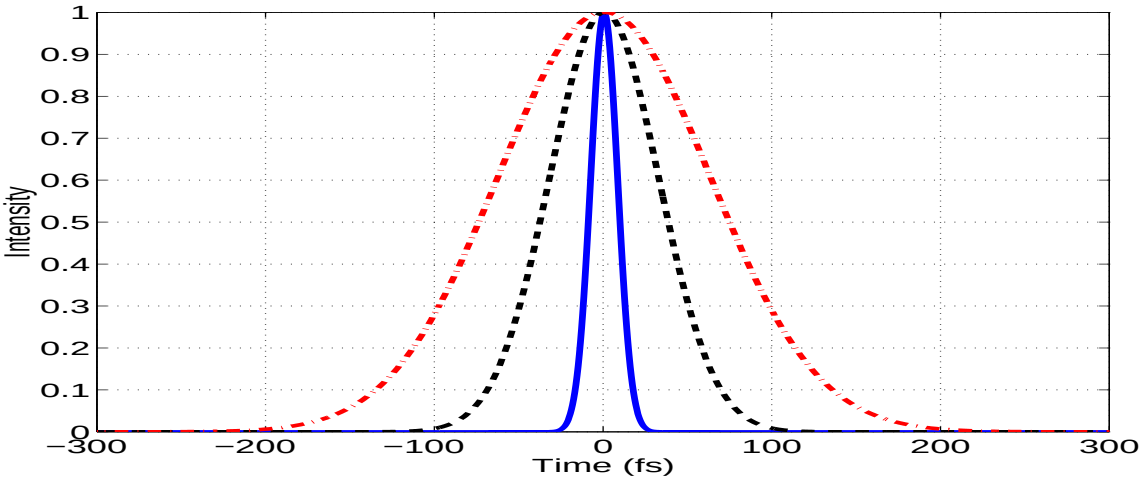

Figure 6.5: Simulated pulse shapes using a 50nm FWHM Gaussian spectrum for a transform limited pulse (solid line), a GVD of 500 fs^2 (dashed line) and 1000 fs^2 (dash-dot line)

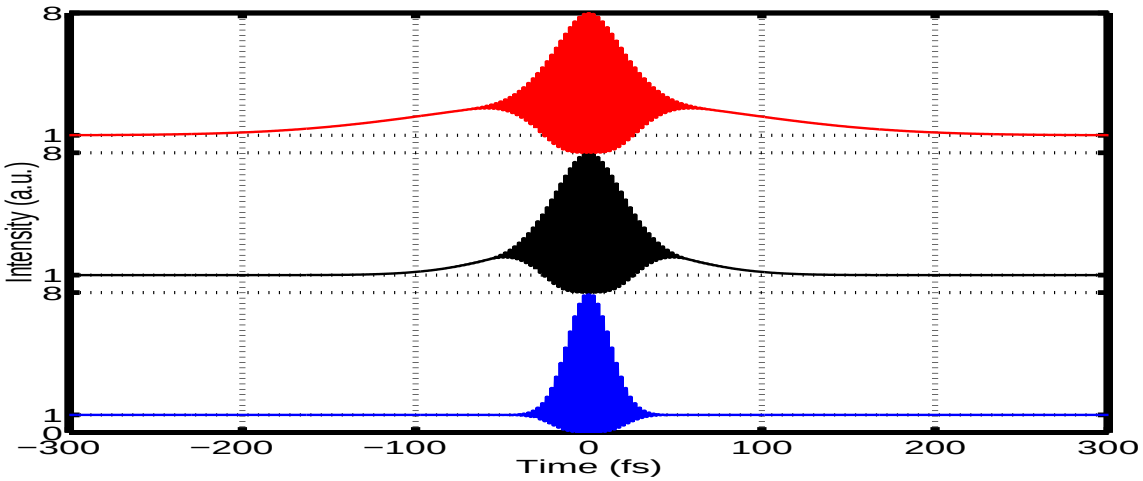

Figure 6.6: Simulated IAC traces using a 50nm FWHM Gaussian spectrum for a transform limited pulse (bottom), a GVD of 500 fs^2 (middle) and 1000 fs^2 (top). The rising 'wings' in the IAC trace give an indication of the second order dispersion

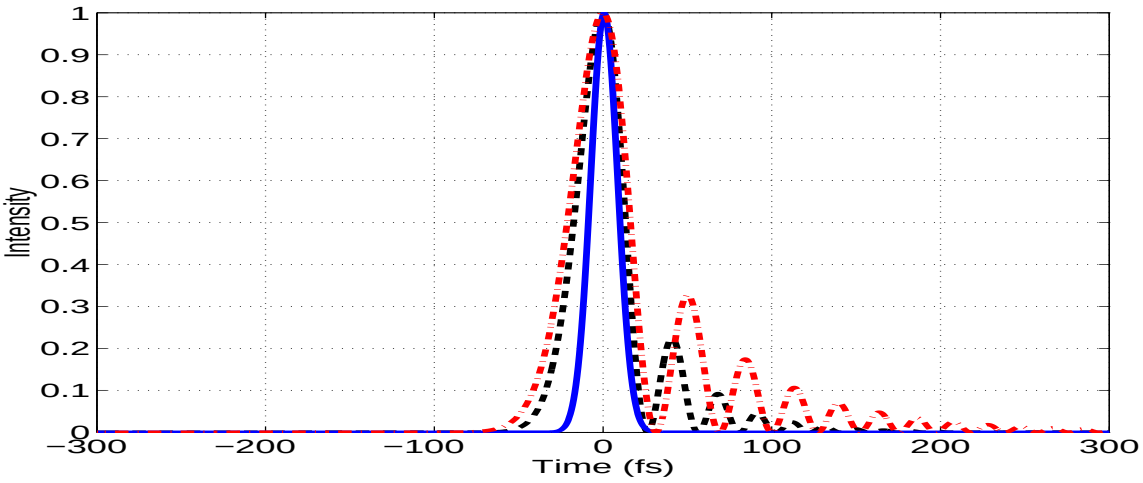

Figure 6.7: Simulated pulse shapes using a 50nm FWHM Gaussian spectrum for a transform limited pulse (solid line), a TOD of $10^4 fs^3$ (dashed line) and $2X10^4 fs^3$

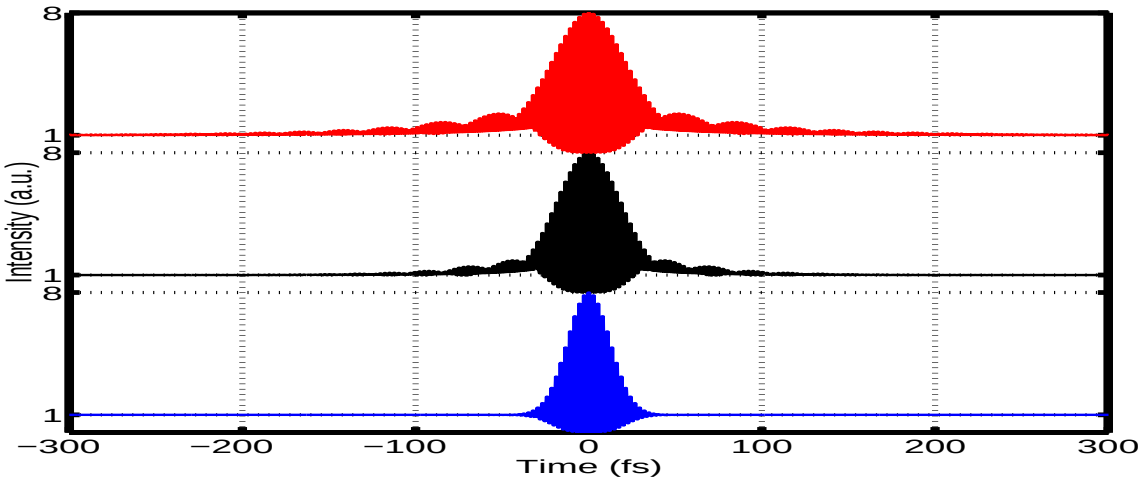

Figure 6.8: Simulated IAC traces using a 50nm FWHM Gaussian spectrum for a transform limited pulse (bottom), a TOD of $10^4 fs^3$ (middle) and $2X10^4 fs^3$ (top). The oscillation in the 'wings' of the IAC trace give an indication of third order dispersion across a pulse

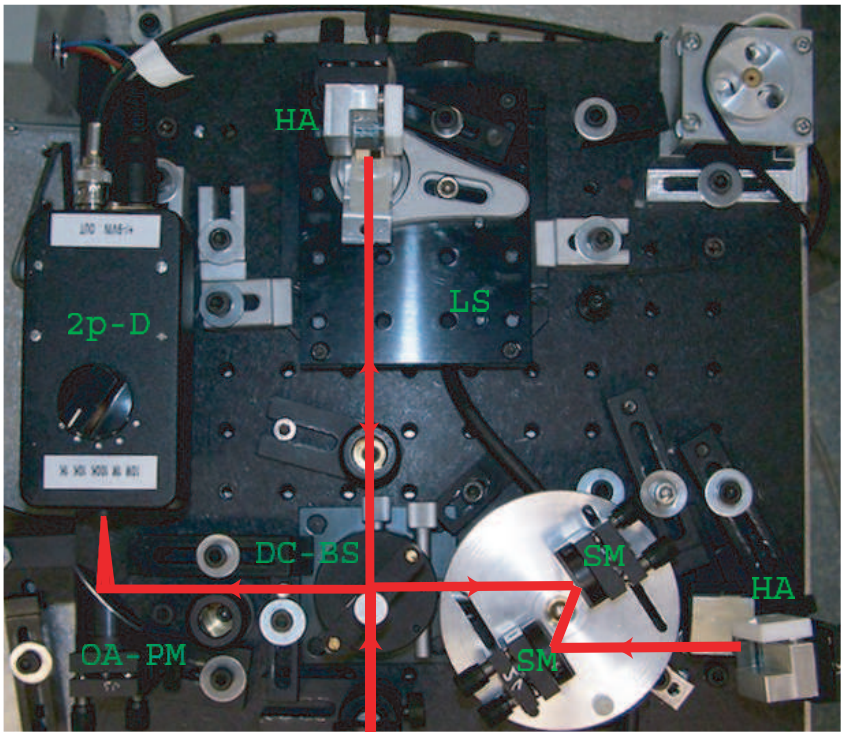

Figure 6.9: The interferometric autocorrelator built for characterizing compressed pulses from the CPA system. With labeled components: DC-BS) dispersion compensated beam splitter, HA) height adjusting periscopes built with low dispersion silver coated mirrors, LS) Newport linear translation stage, OA-PM) silver coated off-axis parabolic mirror, SM) low dispersion silver coated mirrors, 2p-D) two photon diode with variable termination resistance

The 'dispersion compensating' beamsplitter is essentially two beamsplitters fused together in such a way that the dielectric coating of one of the beamsplitters is on the opposite side from the other beamsplitter. The beamsplitter is built in this way so that by spatially shifting pulses in the arms of the the autocorrelator each pulse can be dispersed in the same way on recombination. To facilitate this the IAC was designed with height adjusting periscopes in each arm.

The recombined pulse replicas were made to travel collinearly onto the center of an off-axis parabolic mirror (Femtolasers OA175 f = 5cm) that focused the pulses onto a 2-photon diode (described above), with a nominal rise time of $\sim 1\mu s$.

To facilitate the variable delay required for autocorrelation a Newport linear translation stage controlled by a Newport ESP300 universal motion controller was used in the autocorrelator. The motion controller provided for near-constant stage velocity via an encoder and feedback control loop.

Alternatively to the Newport linear translation stage the autocorrelator could be run in 'spinning disc' mode [25]. In this mode of operation a machined disc on which two parallel mirrors were mounted and positioned facing each other was made to spin (see figure 6.9. Due to the parallel orientation of the mirrors on the disc pulses were transmitted parallel to, although laterally displaced from, the optical axis into the system. A transmitted pulse could be retroreflected back through the spinning disc system using a plane mirror therefore returning along the same line that it entered the system. As the disc was made to rotate the path length of the disc system varied smoothly hence providing the continuous delay required of an autocorrelator system. A DC motor and belt from a turntable was used to facilitate the spinning motion of the disc. By adjusting the voltage to the DC motor the speed of rotation could be adjusted.

Because of the difference in pulse repetition rate between the oscillator and CPA systems data acquisition was handled differently for each case.

Oscillator Trace Acquisition

In the case of the oscillator the pulse repetition rate was many times greater than the bandwidth of the detector resulting in a constant signal, for a given delay position, from the 2-photon diode.

IAC traces were performed by moving the linear stage at a constant velocity and continuously recording the two-photon diode signal. In this case IAC traces could be recorded by any device that plotted input signal vs time and had a large enough sample rate to provide legible traces for a given scanning speed. For most applications the linear stage was moved at a velocity of $20\mu m/s$ which translates to $\sim 15fs/s$ of stage travel. At this speed ~70 thousand samples could be recorded for every fs of stage delay, given a detector with a rise time of $\sim 1\mu s$. A Techtronics digital oscilloscope with a bandwidth of 1 GHz was used to record autocorrelation traces. Data was analyzed with the program, 'ReadACOsc.m', written in the

MatLab programming language.

Autocorrelations of oscillator pulses obtained in spinning disc mode had a high level of ambiguity as small variations in the stage speed could lead to large errors in pulse width determination. In addition to which the rate of rotation of the spinning disc ($\sim$1Hz) in combination with the geometry of the system produced $\sim$1 sample every fs of stage delay. Data was recorded using a Techtronics digital oscilloscope, similarly to what was described above. However, pulses traveling in the rotating arm of the autocorrelator were incident on the detector for brief windows of time (twice per rotation of the disc) due to the geometry of the system. The edges of these events were used as a trigger signal in order to provide a continuously updated autocorrelation trace. The updated traces were observed to have acceptable levels of temporal jitter. Data obtained in spinning disc mode was analyzed with the program ,'ReadACSpinDisc' written in the MatLab programming language.

The limited sampling speed of the 2-photon detector used for the spinning disc system resulted in the interference fringes of the autocorrelation trace being washed out resulting in less accurate autocorrelation traces. However,due to the relatively fast update times of the spinning disc it was possible to make changes to the laser system and see the effect immediately.

CPA System Trace Acquisition

Pulses from the CPA system repeated at a rate of 1kHz. At this repetition rate the two-photon diode was able to resolve individual pulses giving a non-constant signal for a given delay position. To facilitate IAC traces data acquisition was handled by a Gage-scope data acquisition card (up to $1Gs/s$) on a personal computer running a LabView program, called 'ACScan.vi', designed to analyze the data and provide a real-time display. The LabView program operated by using a 1kHz square wave signal fed to the Gage-scope card from the Pockels cell as a trigger signal. With each trigger the LabView program acquired a sample set from the 2-photon diode, read the peak value and wrote the result, along with a time acquired from an internal clock with *ms* accuracy, to a data file. A screen shot of the program in operation is shown in figure 6.10.

System Verification

To determine the accuracy of traces returned by the IAC a controlled experiment was performed. Pulses from the oscillator were first measured with the IAC. The dispersion of pulses from the oscillator was then estimated by matching a simulated IAC trace, using a measured oscillator spectrum, to the recorded IAC trace.

It is noted that an iterative algorithm presented by [43] is claimed to be able to deduce the phase profile of pulses given their spectrum and IAC trace, however a

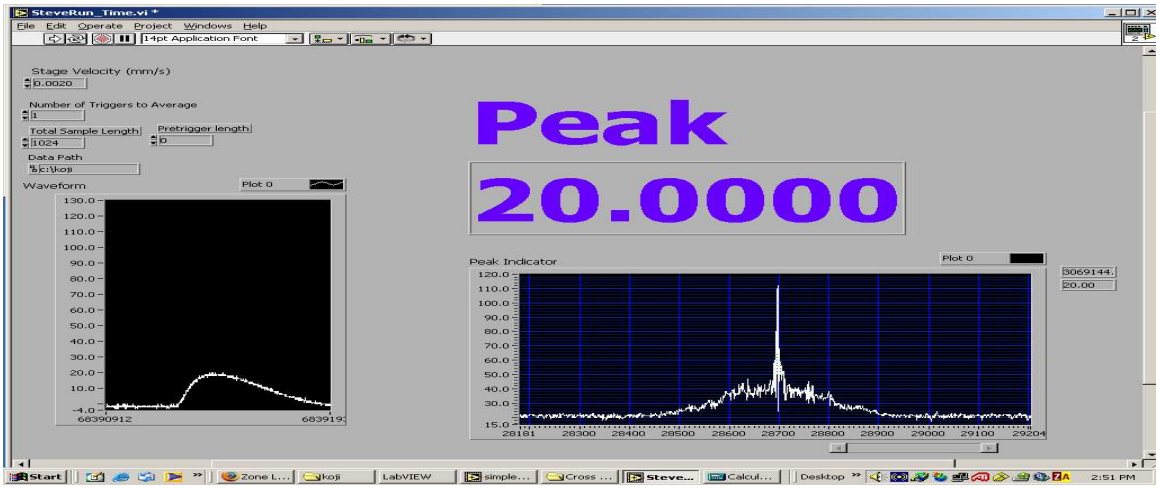

Figure 6.10: A screen shot from the acquisition control software, 'ACScan.vi', used to record autocorrelation traces from the IAC. The box on the left displays the instantaneous photo-diode signal triggered by the Pockels cell. A numeric display, labeled 'Peak', gives the current maximum peak height read from the photo-diode. The window at the right of the screen gives a display of the peak signal versus time, here an autocorrelation of a highly dispersed pulse out of the compressor can be seen.

later claim was made that pulse shapes retrieved using this method were highly ambiguous [33].

A sufficient match between a measured oscillator pulse IAC and a simulated IAC trace was obtained for the phase profile shown in figure 6.11. The corresponding measured and simulated IAC traces are shown in figure 6.12A). It is noted that the measured IAC shows the 1:8 ratio that is expected from an IAC trace.

In a second step the oscillator pulses were passed through $\sim 6mm$ of BK7 glass and the IAC was measured. An IAC trace was then simulated using the dispersion profile determined in the first step summed with the theoretical dispersion due to the extra material. The resulting measured and simulated IAC trace is shown in figure 6.13.

Variations between the simulated and measured IAC traces are most likely due to errors in the estimated phase profile determined in the first step. However, the measured and simulated IAC traces correspond well in terms of the slope of the 'wings' in each trace which indicates that the IAC is a good tool for determining the pulses relative deviation from transform limit. The 8:1 ratio of the measured autocorrelations is also a good indication of the devices correct operation.

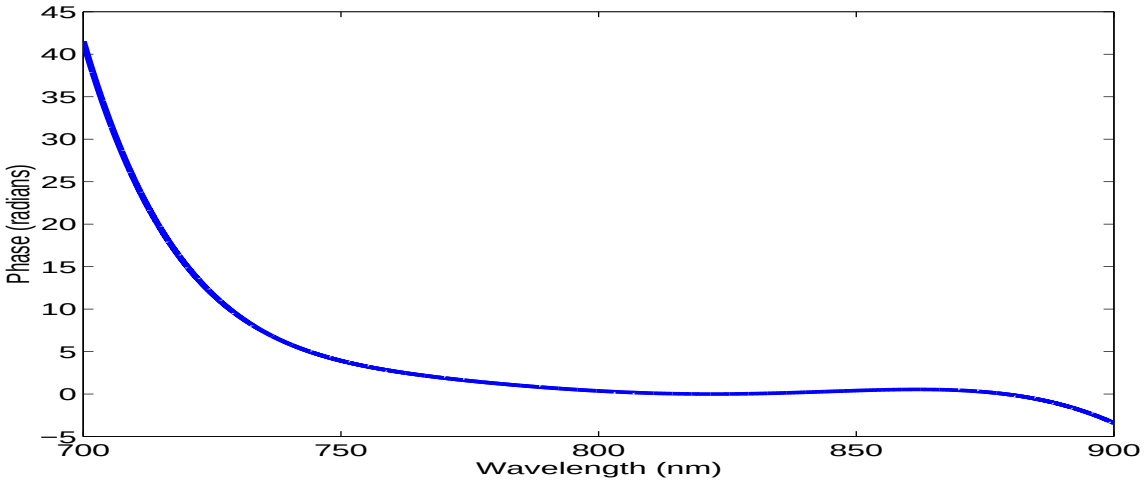

Figure 6.11: Phase profile corresponding to the simulated IAC trace matched to a measured IAC trace for an oscillator pulse

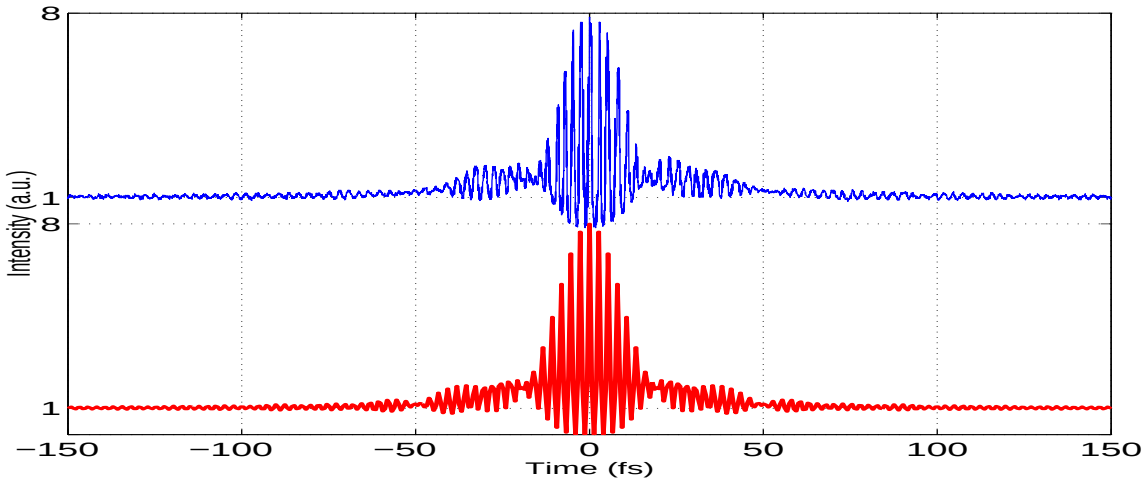

Figure 6.12: Measured (top) and simulated (bottom) IAC traces for pulses from the oscillator

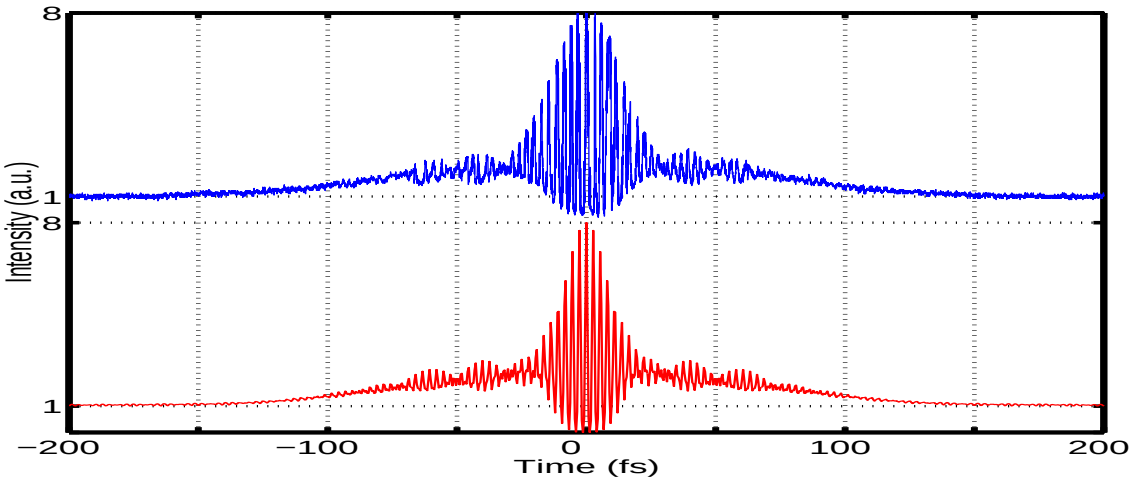

Figure 6.13: Measured (top) and simulated (bottom) IAC traces for pulses from the oscillator after traveling through $\sim 6mm$ of BK7 glass

6.4.3 Spectral Phase Interferometry for Direct Electric Field Reconstruction (SPIDER)

SPIDER is an optical device based on the technique of spectral shearing interferometry. In the SPIDER technique the phase of a test pulse is reconstructed by performing a series of Fourier transformations and filtering processes on a spectral interference pattern produced by the test pulse and a spectrally 'sheared'(linearly shifted in frequency) replica.

The spectral interference pattern is generated as the result of a temporal delay, of length τ, that is produced between the test and replica pulses. The temporal delay between the two pulses produces a linear shift in spectral phase, $e^{i\omega\tau}$ which is manifested as an oscillation in the frequency domain signal with a period $\Delta\omega$ where:

$$\Delta\omega = \frac{2\pi}{\tau} \tag{6.5}$$

By spectrally shearing the pulse replica the spectral phase and amplitude information is made to shift in frequency.

$$\phi_\omega(\omega) \rightarrow \phi_\omega(\omega + \Omega) \tag{6.6}$$

$$E_\omega(\omega) \rightarrow E_\omega(\omega + \Omega) \tag{6.7}$$

Where Ω is the spectral shear imparted on the pulse replica.

The interference pattern produced by the test pulse and the spectrally sheared pulse replica will be distorted as compared to the spectral interference pattern pro-

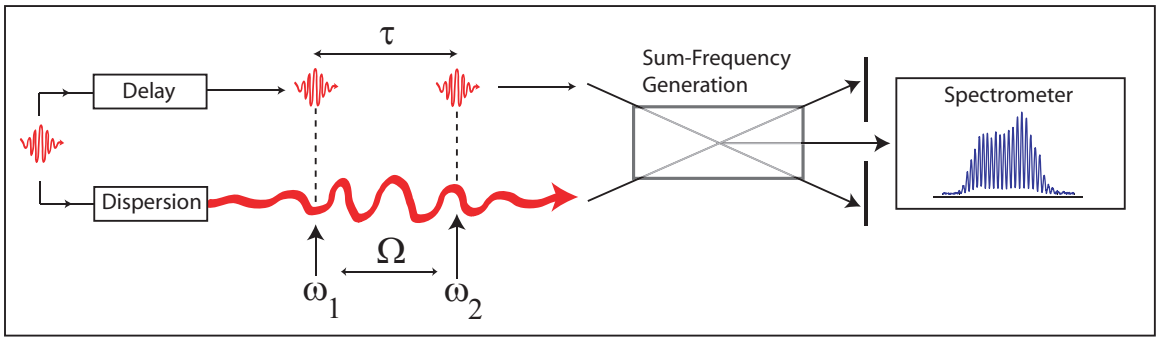

Figure 6.14: A pulse to be measured (left side) is split into a delay arm and a dispersion arm. Two pulse replicas, with temporal separation τ, are generated in the delay arm. The pulse replica in the dispersion arm is stretched in time so that sum-frequency generation with the two pulse replicas in the delay arm generates two pulses spectrally sheared by Ω. The spectrally sheared pulses are allowed to spectrally interfere in a spectrometer giving the necessary data to reconstruct the initial electric field of the pulse.

duced by two non-sheared pulse replicas. The phase difference between the test and replica pulses can be recovered by following the SPIDER inversion routine, as outline in figure 6.15 and described below.

Mathematically the spectral interference pattern produced by the SPIDER technique is given by:

$$\begin{aligned} S(\omega,\tau) &= |E_{test}(\omega)|^2 + |E_{replica}(\omega+\Omega)|^2 \\ +2|E_{test}(\omega)||E_{replica}(\omega+\Omega)| &\cdot \cos(\phi_{test}(\omega) - \phi_{replica}(\omega+\Omega) + \omega\tau) \end{aligned} \tag{6.8}$$

The first two terms in equation 6.8 are the power spectra associated with each of the test and replica pulses respectively. The third term is the interference term and contains the phase difference information for extraction. A Fourier transform of equation 6.8 produces a central 'DC' peak, due to the power spectra of the test and replica pulses, surrounded by two 'AC' terms centered at the delay time, $\boldsymbol{\tau}$. If the 'AC' terms are well separated from the central 'DC' term then one of the 'AC' terms can be isolated with an appropriate filter. An inverse Fourier transform is next performed on the selected 'AC' term and the argument of the transformed signal is taken. The recovered argument is exactly the phase difference between the spectrally sheared pulses plus the phase due to the temporal delay between the pulses.

$$arg[S_{AC}(\omega,\tau)] = \phi_{test}(\omega) - \phi_{replica}(\omega+\Omega) + \omega\tau \tag{6.9}$$

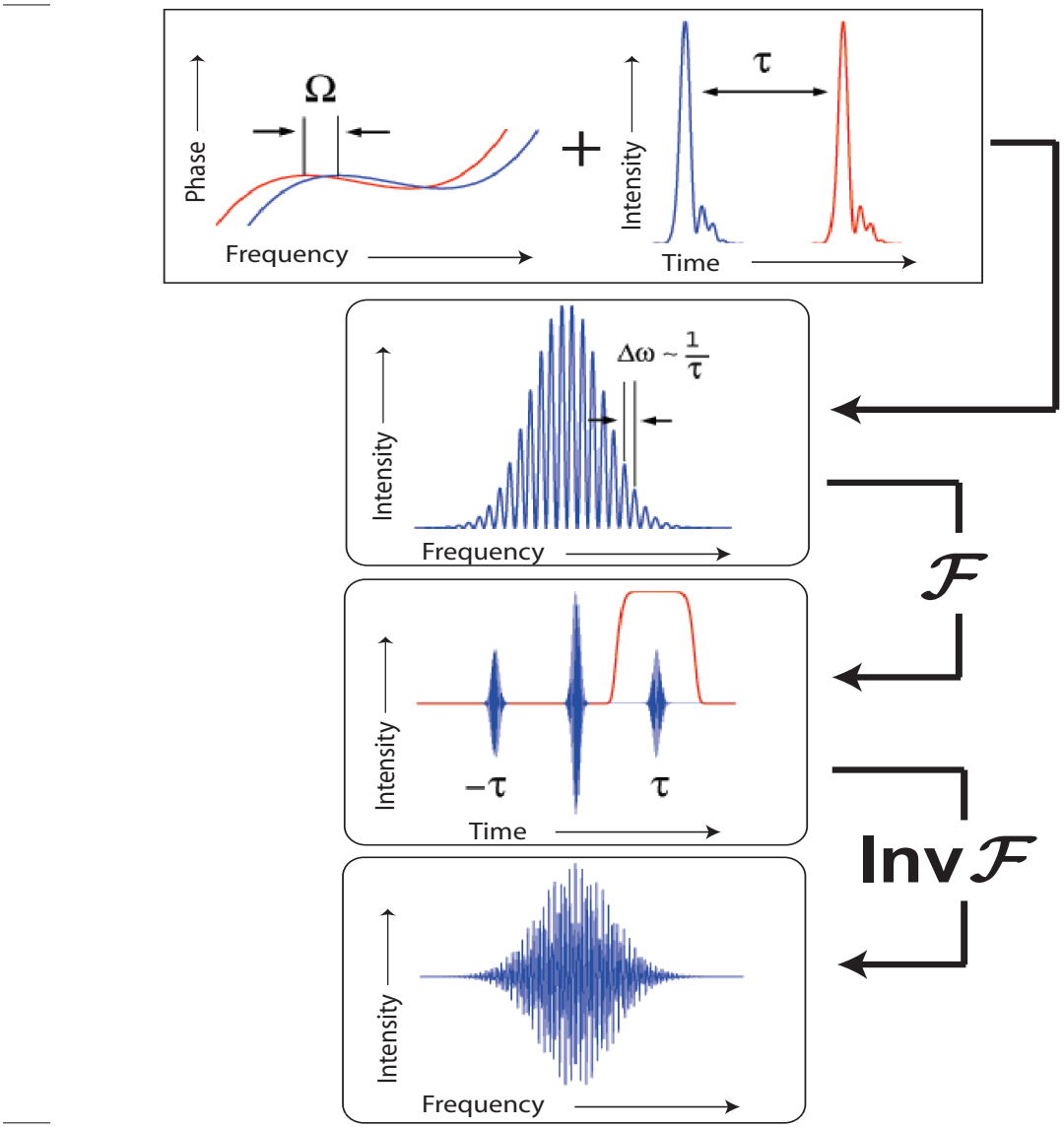

Figure 6.15: The flow of operations in the SPIDER inversion routine. Two pulses with a spectral shear, Ω, and group delay, τ, produce a spectral interference pattern with a fringe separation of $\Delta\omega \sim 1/\tau$. Fourier transformation of the spectral interference pattern produces two AC side bands centered near the group delay τ. An AC side band is selected, using an appropriate filter, and an inverse Fourier transform is performed. The phase difference between the two pulses is the argument of the returned inverse Fourier transform.

Once the temporal separation between the pulses is determined the phase difference between the test pulse and the spectrally sheared replica can be isolated. The phase of the test pulse is recovered by adding up phase differences for frequencies separated by the spectral shear with a concatenation routine.

$$\begin{aligned}\phi(\omega_0 - 2\Omega) &= -\theta(\omega_0 - \Omega) - \theta(\omega_0) \\ \phi(\omega_0 - \Omega) &= -\theta(\omega_0) \\ \phi(\omega_0) &= 0 \\ \phi(\omega_0 + \Omega) &= \theta(\omega_0 + \Omega) \\ \phi(\omega_0 + 2\Omega) &= \theta(\omega_0 + 2\Omega) + \theta(\omega_0 + \Omega)\end{aligned} \tag{6.10}$$

Conveniently this is the requirement set by the Shannon-Whitacker sampling theorem [44] in order to be able to fully reconstruct a signal with compact support (finite width) in the time domain.

Alternatively to the concatenation routine the phase difference between the test and replica pulses can be integrated to reproduce the spectral phase of the test pulse.

$$\phi_{test}(\omega) = \frac{1}{\Omega} \int d\omega \phi(\omega) \tag{6.11}$$

Once the spectral phase of a pulse has been retrieved the pulse shape can be reconstructed by combining the spectral phase with a separate measurement of the pulse spectrum.

SPIDER Simulation

A simulation of the SPIDER system, 'SPIDERSim.m', was written in order to gain insight into the subtleties involved in the technique. The effects of finite spectrometer resolution, noise and calibration errors on the ability of the SPIDER to recover a given phase profile were studied.

Finite Resolution of the Spectrometer

To determine the effects of the spectrometer finite resolution on SPIDER accuracy the residual error between initial and recovered phase profiles with a GVD of $100 fs^2$ was determined as a function of fringe separation in the SPIDER trace (determined by the group delay) for a given spectrometer resolution. It was found that a minimum in the returned error occurred for a fringe sampling rate of between 5 and 10 as shown in figure 6.16 for a spectrometer resolution of 0.5THz. Below 5 samples per fringe the errors in the returned phase increased slowly until

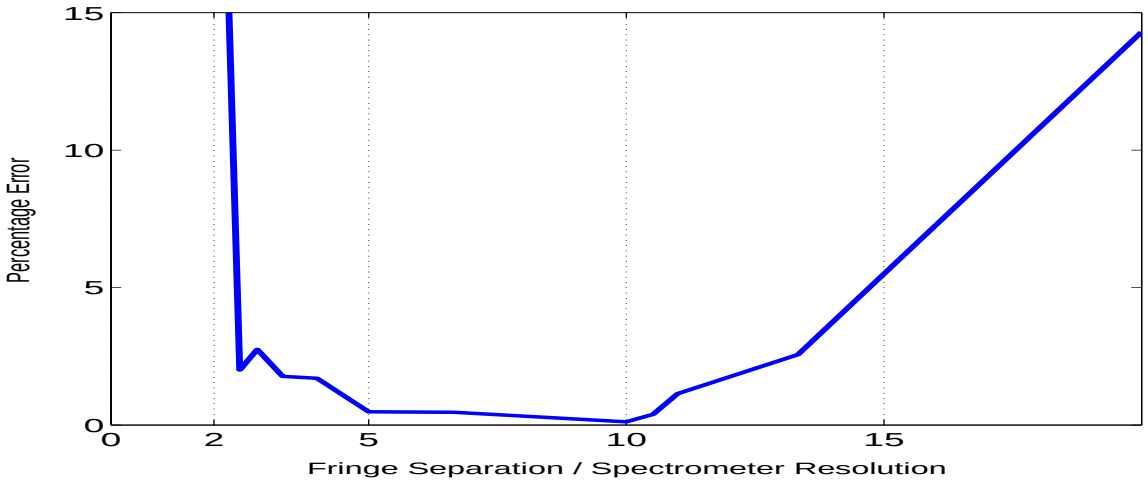

Figure 6.16: The effects of finite spectrometer resolution on returned phase values for SPIDER)

the Nyquist sampling limit was reached at 2 points per fringe. Above 10 points per fringe the errors in the returned phase were seen to rise steeply which can be explained by the merging of the AC side bands in the Fourier transform of the SPIDER trace with the central DC portion as the group delay is decreased.

The results of this simulation indicate that at least 4 samples per fringe in the SPIDER trace should be maintained.

The Effects of Noise

The effects of noise on the ability to recover phase profiles from the SPIDER were explored by introducing an additive noise to simulated SPIDER traces before proceeding with the SPIDER inversion routine. The results indicated that the SPIDER inversion routine is extremely robust, capable of recovering extreme phase profiles, to reasonable degree, even in the presence of high noise levels as shown in figures 6.17, 6.18 and 6.19

Calibration Error

The effects of error in the group delay calibration were explored through simulation and are summarized in figure 6.20. The results indicate that errors in the group delay calibration result in a linear error in the recovered GVD as expected.

An interesting subtlety of the SPIDER system lies in the Fourier transform of the SPIDER interference pattern. Because the phase profile, locked in the AC sidebands after the first Fourier transform, is in fact the phase difference between the test pulse and spectrally sheared replica, the GVD of the pulse effects the side band

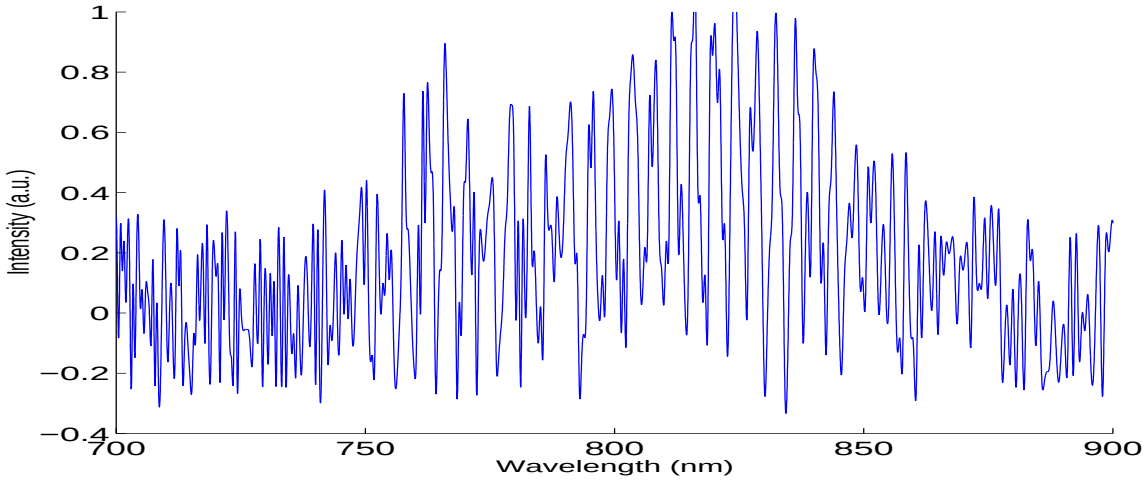

Figure 6.17: A simulated SPIDER trace using a spectrometer resolution of 0.22THz @400nm and a 30% additive noise with a group delay of $0.5ps$ (fringe separation of 2THz)

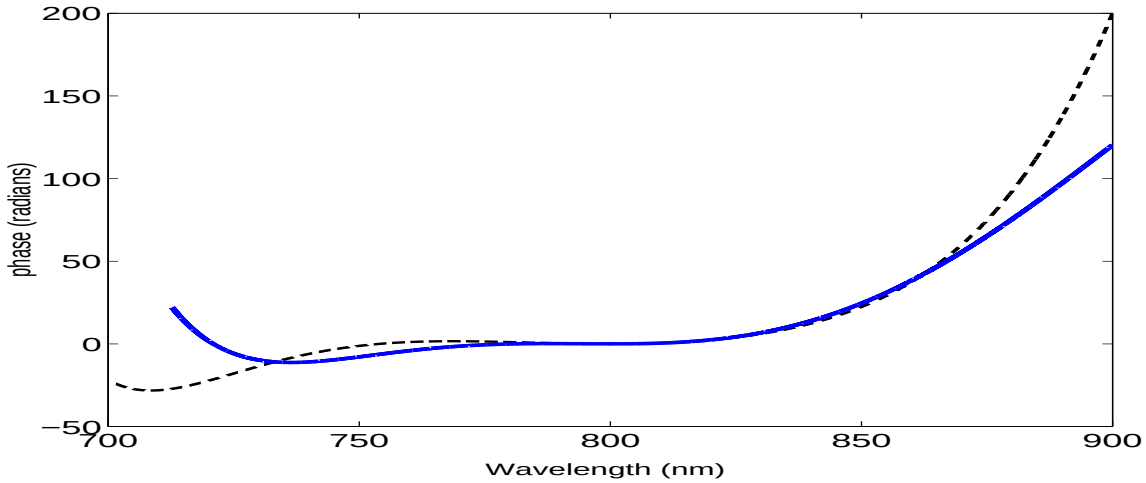

Figure 6.18: The simulated initial (dashed line) and recovered (solid line) phase profiles for the SPIDER trace in figure 6.17.

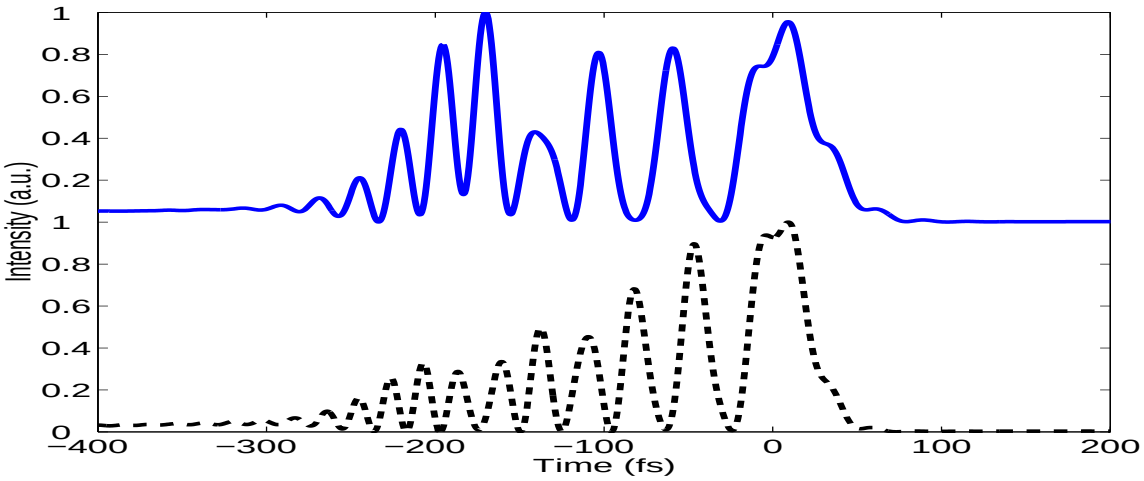

Figure 6.19: The pulse shapes corresponding to the initial (dashed line) and recovered (solid line) phase profiles of figure 6.17 for a simulated SPIDER trace with a 30% additive noise.

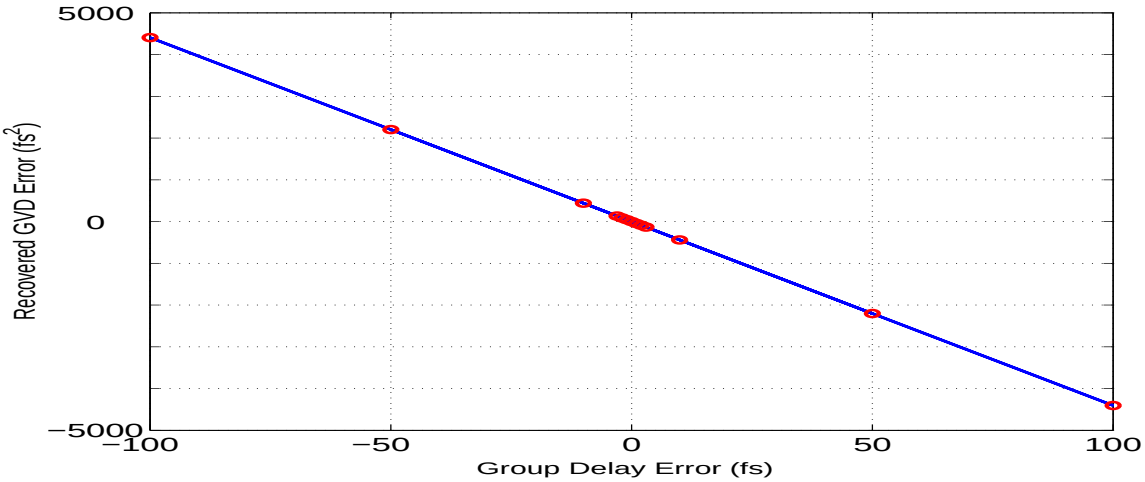

Figure 6.20: The simulated residual GVD in the recovered phase profile for given errors in the group delay. All simulations were run with a spectral shear, Ω, of 3.6THz

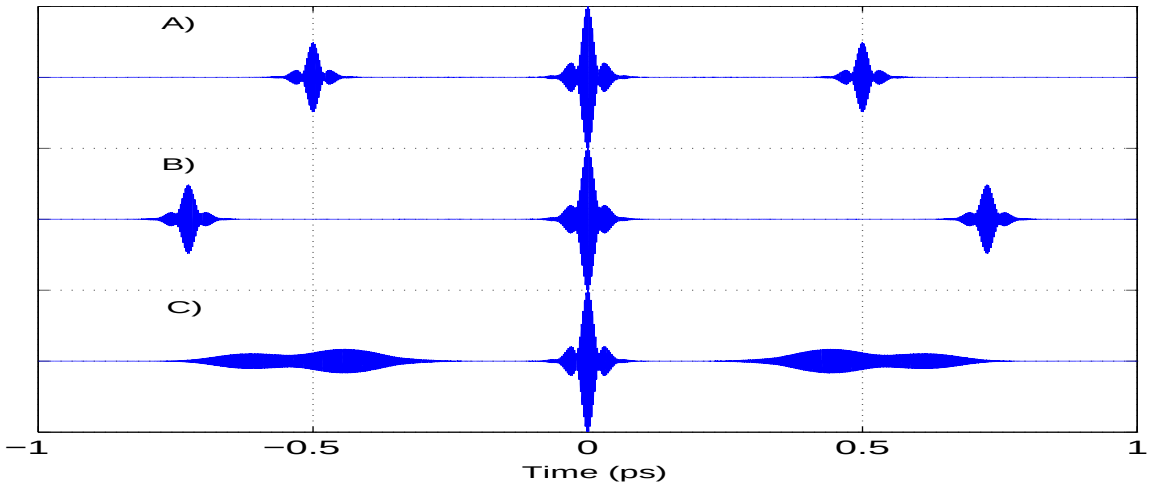

Figure 6.21: The Fourier transform of three different SPIDER traces simulated with A) transform limited pulses, B) linearly chirped pulses and C) pulses with third order dispersion only. In each simulation a group delay of 0.5ps and a shear of 3.6THz was used.

as GD effects the pulse, the TOD of the pulse effects the side band as GVD effects the pulse shape, and so on. Hence some features of a pulse can be determined just from looking at the Fourier transform of the SPIDER spectral interference pattern as shown in figure 6.21.

Design Considerations

Choosing optimum values for the group delay and spectral shear are most important when setting up a SPIDER system. The fringe separation of the spectral interference pattern is inversely proportional to the group delay and hence the group delay must be chosen to be small enough so that an acceptable number of fringes can be produced over the spectral bandwidth of the up-converted pulses. However the group delay must also be small enough so that the spectrometer is able to resolve at least two points per fringe as dictated by the Nyquist sampling theorem B.2 and discussed above.

The spectral shear must be chosen such that the Shannon-Whittaker sampling theorem is obeyed. Specifically, for the SPIDER algorithm this means that the shear should be:

$$\Omega \leq \frac{2\pi}{T} \tag{6.12}$$

Where $\boldsymbol{T}$ is the maximum width of a pulse that can be fully characterized given a spectral shear $\boldsymbol{\Omega}$ (in angular frequency). In practice the shear is chosen so that

the pulse duration is much smaller than the envelope T. The shear must also be resolvable by the spectrometer, which set a lower bound of $\Omega = 0.22THz$ for the Ocean Optics HR4000 spectrometer that was used.

The authors of reference [45] give a convenient formulation for the the choice of optimum parameters of SPIDER based on their simulated results. For the group delay they give a suggested value of $\tau = (2\pi/\Delta\omega)(N_s/N_f)$ where N_s is the number of spectrometer pixels across the FWHM of the input pulse spectrum, N_f is the number of spectrometer pixels per fringe and $\Delta\omega$ is the FWHM of the input pulse spectrum. For the spectral shear, a suggested value of $\Omega = \Delta\omega/d$ is presented, where d is the degree above transform limit of the pulse to be measured.

The dispersive arm of the SPIDER must also be carefully considered as the SPIDER technique requires that the replica pulses be up-converted with a quasi-cw field. The authors of [46] indicate that for a stretching factor of $10^4 fs^2$ their SPIDER is capable of measuring pulses up to 40 times the transform limit, $5.3fs$, of their measured spectrum, $\sim 140THz$ FW. In light of equation 3.3 the quoted stretching factor gives a value for $\frac{d\omega}{d\tau}$ of $\sim 1.6X10^{-2}\ THz/fs$. Multiplying by a value of 40 times the quoted transform limited pulse width gives a frequency width of $\sim 3.4THz$ or $\sim 1/40th$ of the input spectral bandwidth. Therefore, it can be reasoned that the test pulse to be up-converted should cover no more than $\sim 1/40th$ of it's input spectrum.

System Design

The SPIDER system was built (figure 6.22) using a similar design to that presented in reference [46] capable of reconstructing pulse widths as short as $5fs$. In this design the front surface reflection off of a glass blank (BK7 6.35mm, FR in the figure) is used to separate the pulse to be reconstructed (reflected) from the pulse to be stretched (transmitted). The transmitted pulse is stretched by the glass blank as well as transmission through 10cm of SF57 glass (MD in the figure), cut at Brewster angle to minimize loss, in order to provide the quasi-CW frequency for up-conversion. The stretched pulse experiences a total GVD of $2.2X10^4 fs^2$. The polarization of the stretched pulse is rotated by 90^o using a $1/2\lambda$ plate (Special Optics 8R-9012) in order to facilitate up-conversion with a, type-II (Kaston Optronics, BBO $\theta = 42.4^o$, 20μm) or ,type-I (Kaston Optronics, BBO $\theta = 30^o$, $1mm$) non-linear crystal (NC in the figure). A delay stage (DA2 in the figure) is used to match the path lengths of the short pulse replicas with the stretched pulse.

The pulse to be reconstructed is split into two replica pulses by a Michelson interferometer type setup. Similarly to the IAC a 'dispersion compensating' beamsplitter arrangement is used in order that each pulse replica sees the same amount of dispersion in the interferometer. The group delay, τ, between the pulse replicas is generated by moving a delay stage in one of the arms of the interferometer (DA1 in the figure).

Both pulse replicas and the stretched pulse are made to be incident on an off-axis parabolic mirror (Femtolasers OA175 f=5cm, OP in the figure). The pulse replicas and stretched pulse are sent to the focusing mirror, parallel to, but spatially separated from each other in order that the pulses are focused at the same spot in space but in a non-collinear arrangement. In this way the generated up-converted light is spatially separated from the pulse replicas and stretched pulses oscillating at the fundamental frequency.

The generated up-converted light is passed through a low pass filter (blue glass) in order to remove any stray infrared light from the pulse replicas and stretched pulse. An iris provides further spatial filtering of the up-converted and fundamental light. A focusing lens (f=5cm, FL in the diagram) and silver mirror (CVI PS-PM-1037-C) are used to couple the up-converted light to the spectrometer input (FC in the diagram).

The spectrometer used (Ocean Optics HR4000) has a spectral resolution of 0.115nm (0.21THz) centered at 400nm (700THz) and a bandwidth of $\sim$ $200nm$ (300nm-500nm) making it an ideal choice for recording SPIDER traces for very broad band pulses.

Calibration

The group delay, τ, was calibrated by inserting a mirror at position A), as shown in the figure, and measuring the spectral interference pattern produced by the pulse

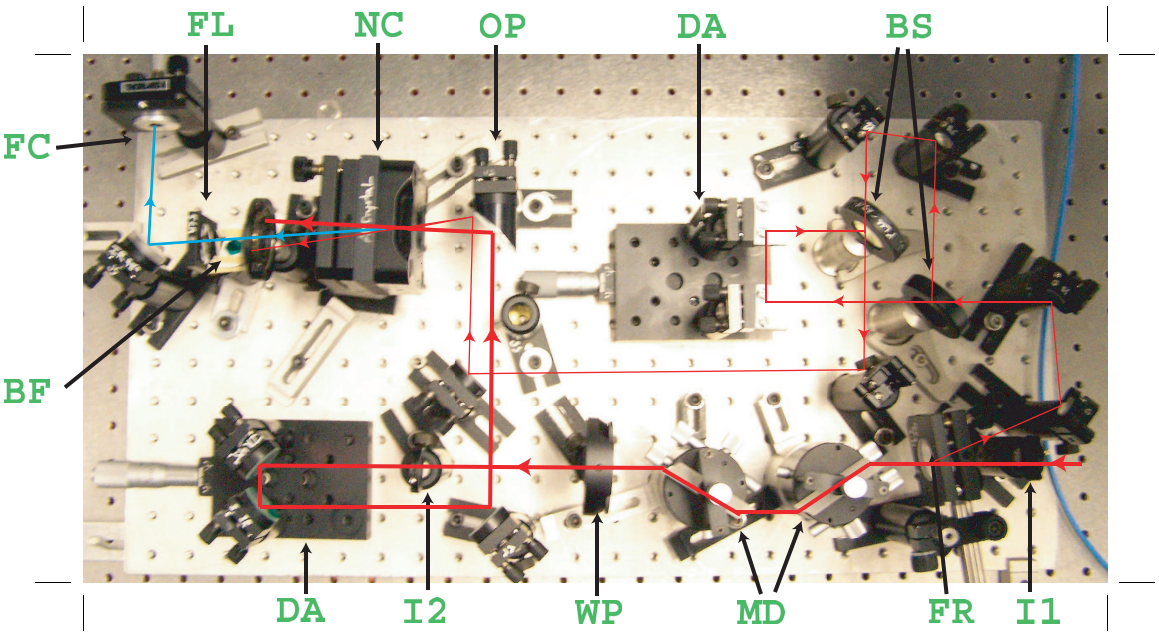

Figure 6.22: The SPIDER built for characterizing ultrafast pulses. With labeled components: I1 and I2) alignment irises, FR) front surface reflector for splitting the pulse, MD) material dispersion stage for stretching the 'long' pulse, WP) 1/2 wave plate for rotating the polarization of the 'long' pulse, DA1) delay arm used to set the group delay, DA2) delay arm used to set the up-conversion frequency, BS) two beam splitters arranged create two equally dispersed pulse replicas, OP) off-axis parabolic focusing mirror (f=5cm), NC) non-linear crystal (both Type-I 1mm thick and Type-II 20μm thick crystals were used), BF) blue filter and iris, FL) focusing lens (f=5cm), FC) fibre coupler to spectrometer, A) position for inserting a mirror to measure the group delay

replicas at the fundamental frequency using a broad band spectrometer (Special Order, Lighting Sciences Canada). A value for the group delay was determined by Fourier transforming the interference pattern and measuring the position, on a time abscissae, of the AC side bands. This method may have introduced systematic errors in the determination of the group delay, as discussed later.

The spectral shear, Ω, was calibrated by either, measuring the shift in frequency between two separately measured up-converted spectra, or by dividing the calibrated group delay by the stretching factor ($2.2X10^4 fs^2$).

The up-conversion frequency was calibrated by determining the central frequency of the up-converted spectrum, for the un-sheared pulse replica (measured with the Ocean Optics HR4000 spectrometer), and subtracting the central fundamental frequency of the pulse being measured (measured with the Lighting Sciences Canada spectrometer).

SPIDER Verification

In an attempt to verify the SPIDER system, SPIDER traces were taken with oscillator pulses, using different values for the group delay, and compared. In order to verify that the recovered phase from the SPIDER responded as expected three SPIDER traces, at each group delay setting, were taken where for each trace the oscillator pulses were made to pass through a different amount of material before entering the SPIDER.

In order to obtain an acceptable signal level for the spectrometer, a 1mm thick BBO crystal was used to facilitate the up-conversion. The thickness of the BBO crystal used acted as a frequency filter, limiting the bandwidth of the up-converted pulses. As a result of this, identifying the central frequency up-conversion and the spectral shear proved problematic. In order to estimate the frequency of up-conversion, the delay stage in the arm controlling the stretched pulse was adjusted until a maximum signal was obtained in the spectrometer, indicating that the pulses were being up-converted with the most intense part of the oscillator spectrum. As a secondary check the non-linear crystal was rotated so that the edges of the up-converted spectrum could be seen, thus providing a measure of the central frequency of the SPIDER trace. From these measurements it was determined that the up-conversion frequency was 367THz (817nm).

The results of the verification test, and a measured SPIDER trace, are shown in figure 6.23. The recovered phase profiles, for different values of the group delay, were not found to correlate given a specified amount of material to disperse the pulses. Attempts to determine if a correlation existed between the recovered phase profiles for different values of the group delay proved inconclusive. However, it is noted that the recovered phase profiles, for different amounts of material dispersion, within each group delay setting, were seen to move in the appropriate direction. The discrepancy between each trace may be due to the thick-crystal used

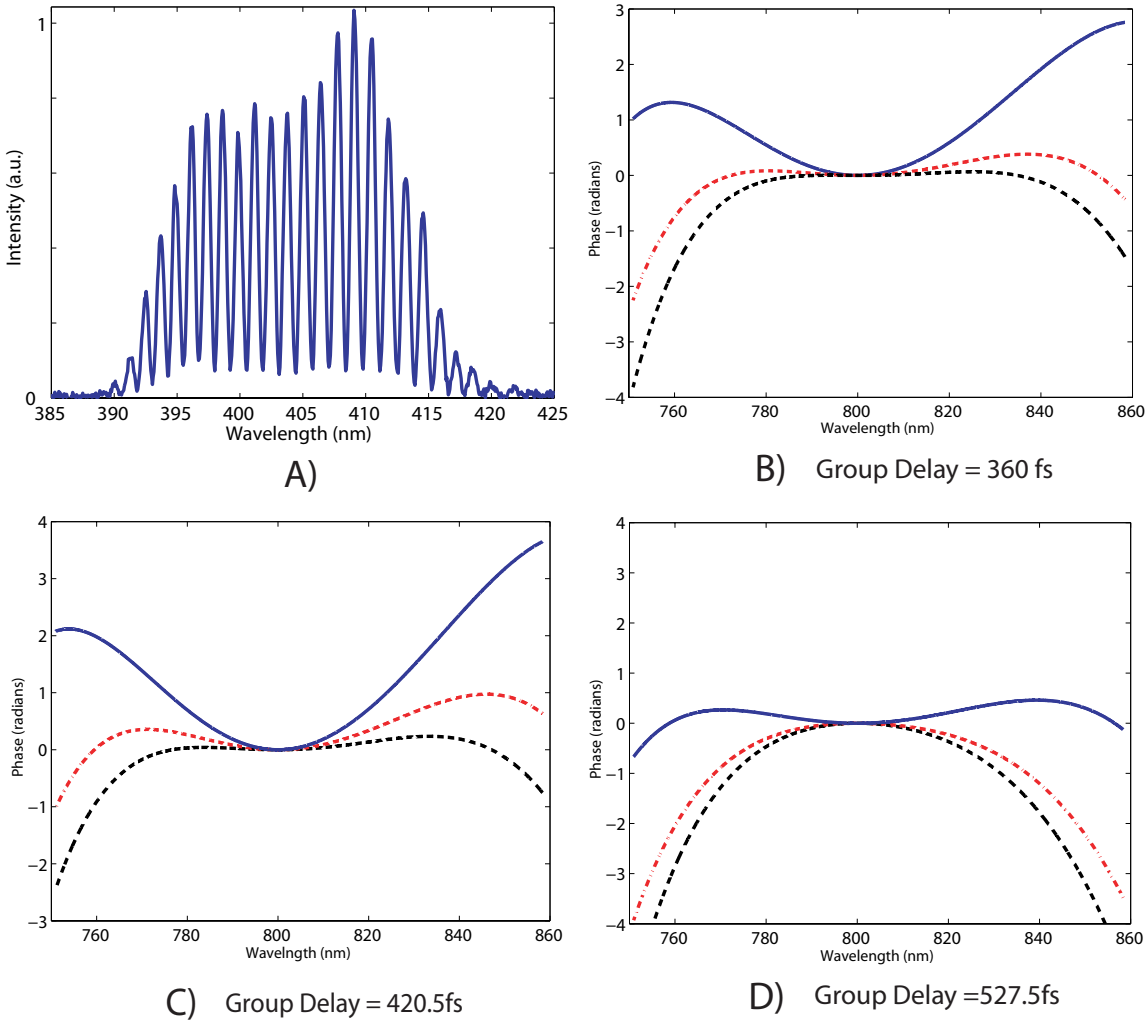

Figure 6.23: A) a measured SPIDER trace of pulses from the oscillator using a $1mm$ thick BBO crystal to facilitate up-conversion. Recovered phase profiles for oscillator pulses traveling through, no extra material (dashed line), 1.6mm of fused silica (dash-dot line), 6mm of BK7 (solid line) for measured group delays of B) $360fs$, C) $420.5fs$ and D) $527.5fs$.

for this experiment or a slight systematic error in determination of the group delay

Chapter 7

Pulse Compression Experiments

7.1 Comparison with Simulation

The prism compressor was arranged as closely as possible to the position determined through simulation (section 5.3.1). An IAC trace of pulses out of the compressor was measured and is shown in figure 7.1.

The discrepancy between the simulated IAC and the measured IAC for the given compressor configuration indicates that some dispersion had been unaccounted for in either the simulation of the regenerative amplifier or the simulation of the compressor. The discrepancy in dispersion between simulated and measured results was estimated by roughly fitting a simulated IAC to the mea-

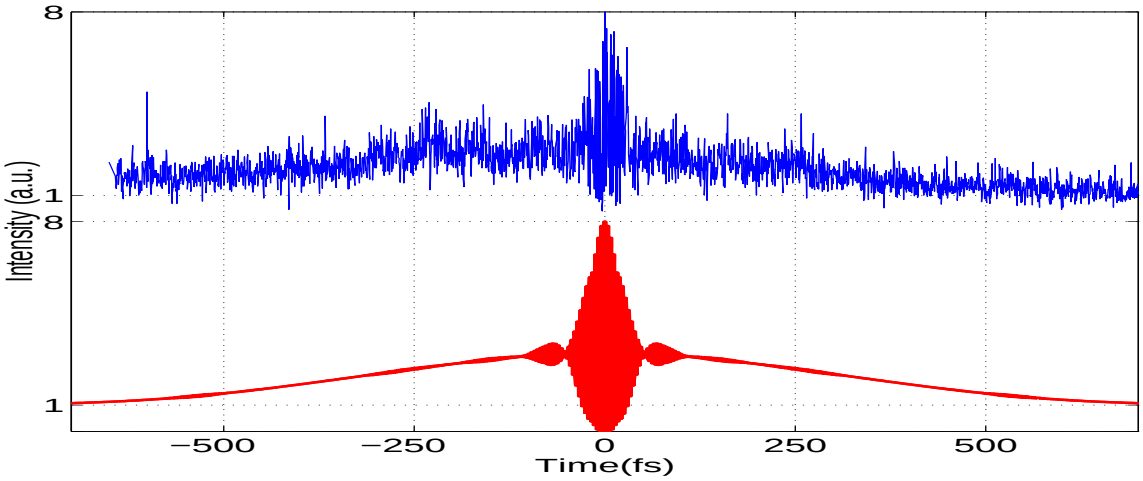

Figure 7.1: Measured IAC using the simulated results to configure the prism compressor compared with a simulated IAC using the compressor simulation result with an additional GVD of $3750 fs^2$

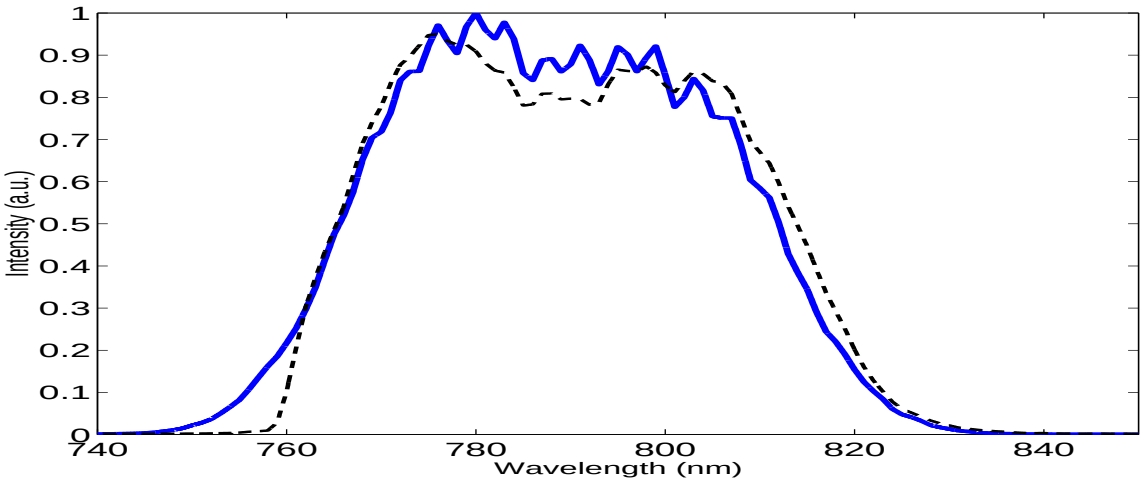

Figure 7.2: Measured spectrum from the regen (solid line) of ∼45nm FWHM and the measured spectrum exiting the compressor (dashed line) showing that the minimum wavelength exiting the compressor is ∼760nm

sured IAC in figure 7.1. The simulated results indicated that an additional GVD of $\pm 3750 fs^2$ provided a near fit to the IAC. This corresponded to a length change of the prism compressor of $\pm 150 mm$.

7.2 IAC vs Compressor Distance

In a first step towards compressing the pulses an experiment was performed in which, the prism separation was changed by different amounts and subsequent IAC traces were taken and compared. During this experiment the insertion parameter λ_{min} was held constant by adjusting the insertion of prism pair P34 (see figure 7.6) such that the minimum wavelength passed by the prism compressor overlapped with the spectrum of pulses out of the regen. The edge in the measured spectra (emitted from the compressor) shown in figure 7.2 confirms that the minimum wavelength passed by the compressor was $\lambda_{min} = 760 nm$.

The results of the experiment are summarized in figure 7.3 and highlight the ability to compress pulses from the regen by adjusting the prism separation distance. The results also indicated the presence of a secondary pulse displaced by $\sim 550 fs$ from the central pulse. Fourier transformation of the spectrum emitted from the regen revealed that the modulations, apparent in the spectrum, corresponded to a secondary pulse $\sim 550 fs$ from the central pulse. This indicatied that a reflection due to an optic of thickness $\sim 80 \mu$m might be taking place inside the regen. Efforts to find the source of the reflection proved inconclusive.

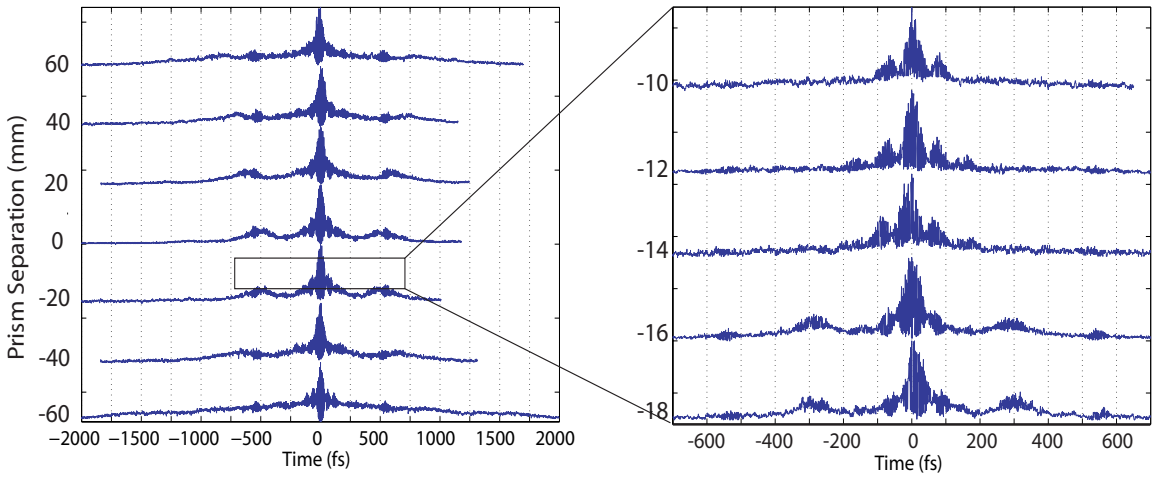

Figure 7.3: Measured autocorrelations vs prism compressor separation

7.2.1 Correction of Spatial Chirp

Work done, after the above experiment was performed, revealed that there was a significant amount of spatial chirp across the beam profile.

Spatial chirp was qualitatively examined by mounting a spectrometer on a rail and sliding it across the beam profile (∼10mm diameter). 'Good' spatial chirp was determined to be the condition in which the spectrometer could be scanned across the beam profile and a near-uniform drop in intensity across the spectrum observed. An example of 'good' and 'bad' spatial chirp is shown in figure 7.4. For the case of bad spatial chirp, P34 has been rotated by $\sim 10^o$ from Brewster angle.

It was found that a rotation of prism pair, P34 by $\sim 5^o$ rotation CCW, and P12 by $\sim 2^o$ CW, from that used in the above experiments eliminated the spatial chirp across the beam to an acceptable level. An IAC trace, taken after compensation of the spatial chirp was performed, is shown in figure 7.5. For the given trace, the configuration of the prism compressor was the same as that of the 'most compressed' IAC trace of figure 7.3 with the exception of the rotation of prism pair P34 by $\sim 5^o$. This illustrates the sensitivity of the alignment of the prism compressor.

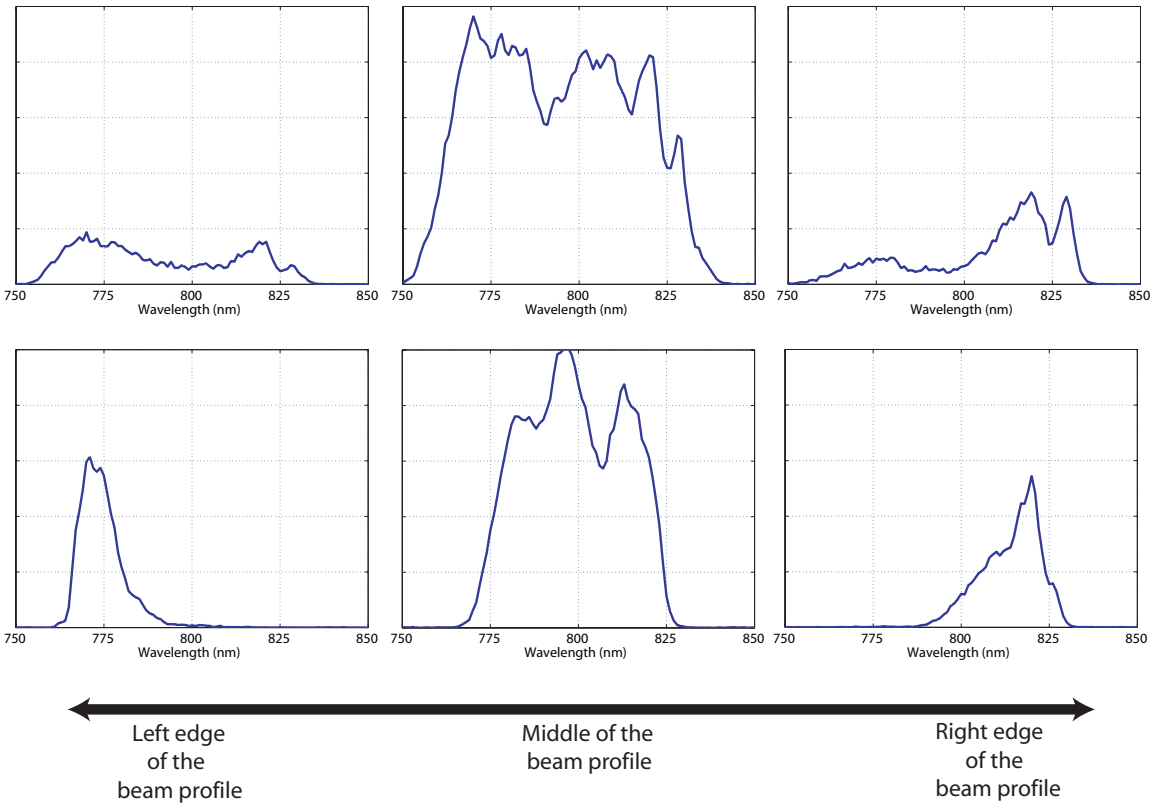

Figure 7.4: An example of; Top) 'good' spatial chirp and Bottom) 'bad' spatial chirp

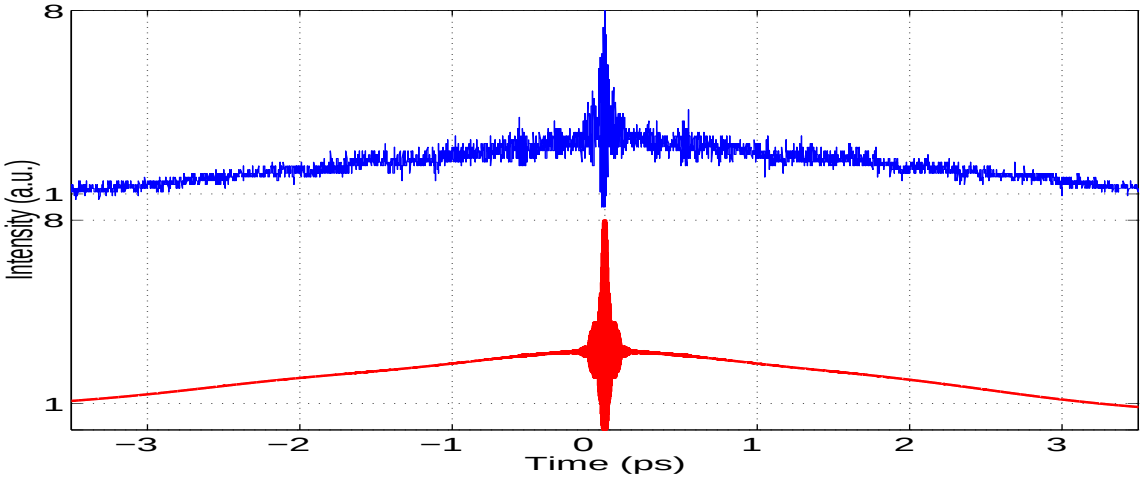

Figure 7.5: Measured autocorrelation after adjusting for spatial chirp. The measured autocorrelation is shown with a simulated autocorrelation using the measured spectrum from figure 7.2 and GVD of $2.4X10^4 fs^2$ $@800nm$.

7.3 GVD Profile Mapping by Spectrum Sampling and Autocorrelation

As the results of the prism compressor simulation suggest, for a given configuration, the GVD profile may change by large values over the spectrum of a pulse but maintains a smooth profile with no discontinuities. As described in section 2.3, linear changes in the GVD profile are described by the TOD coefficient while higher order dispersion terms appear as a curvature or oscillation in the GVD profile. In light of the results presented in chapter 3, dispersion is seen to have a diminishing effect on pulse shape as the spectrum of a pulse is decreased in width. Therefore, as the spectrum of a pulse is decreased, local changes in the GVD across the spectral width should have a small effect on the returned pulse shape.

In an effort to try and map out the GVD profile of pulses emerging from the compressor an experiment was performed in which the spectrum of compressed pulses was sampled in discrete intervals using spatial filters placed in front of the retro-reflecting mirror, RR, in the compressor, approximately corresponding to a Fourier plane (see figure 7.6. IAC traces were taken for each spectrum interval and a GVD, at the central wavelength of the sampled spectrum, was determined by fitting a simulated IAC to the measured IAC.

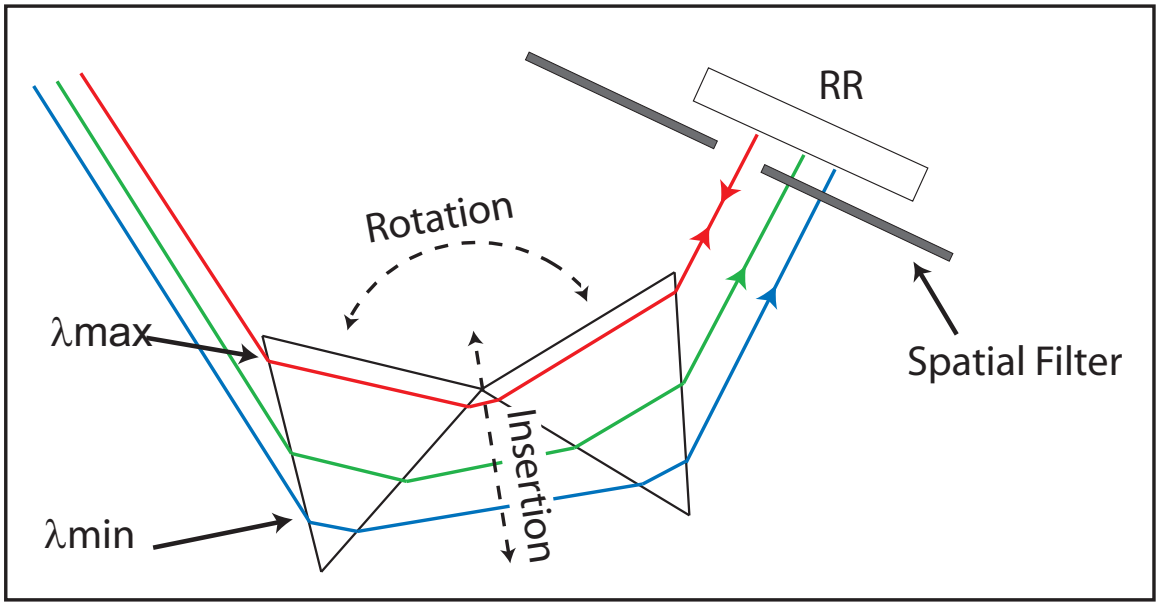

Figure 7.6: A schematic of prism pair P34 showing, the minimum wavelength passed λ_{min}, the maximum wavelength passed λ_{max}, the directions of insertion and rotation, the placement of a spatial filter for the GVD mapping experiments and the retro-reflecting mirror RR

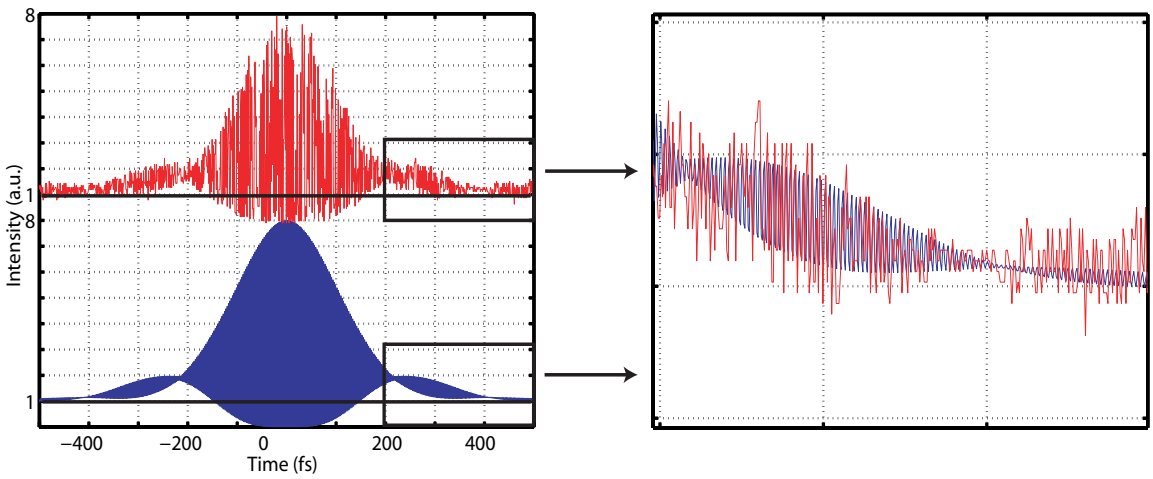

Figure 7.7: Left side; an experimental (top) and simulated (bottom) IAC trace from the experiment corresponding. Right side; in order to match the wings in the IAC traces, as closely as possible, simulated and measured IAC traces were superimposed

Figure 7.7 shows a standard IAC trace during the experiment and a matched simulated IAC with a GVD of $11X10^4 fs^2$ at a center wavelength of 790nm. Generally, matches to experimental traces were performed by superimposing the simulated and experimentally measured IAC traces such that their background signals and centers matched. A sufficiently good match was made when the slope of the wings of each IAC were seen to overlap.

In light of equation 3.3 for GVD values of $\frac{\sqrt{3}\tau_p}{\delta\omega}$, where τ_p is the transform limited pulse width, a pulse width of $2\tau_p$ is expected. for a 10nm bandwidth pulse centered at $800nm$ a GVD of $\sim 5000 fs^2$ would lead to a doubling of the pulse width. A reasonable estimate for the accuracy of the experiment would then be $\sim \pm 2500 fs^2$ for each IAC trace.

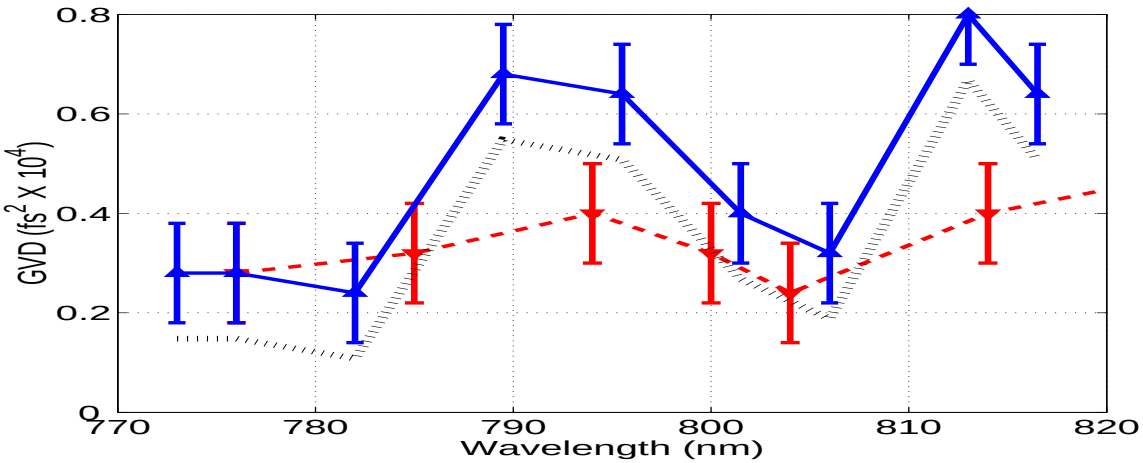

Figure 7.8: The mapped GVD profile for pulses taking 23 (solid line) and 20 (dashed line) trips in the regen compared to the expected result for 20 round trips (dotted line).

7.3.1 First GVD Mapping

A GVD profile was mapped first for pulses taking 23 round trips in the regen and then for pulses taking 20 round trips in the regen. This was done in order to see how the mapped GVD profiles changed with a decrease in the overall positive system dispersion. For this experiment IAC traces, for spectral slices of up to $25nm$ wide, were taken. This width was subsequently reduced to $\sim 10nm$ in future experiments. The results of the experiment are shown in figure 7.8 including the expected result, based on in the first mapped GVD profile minus the simulated dispersion for 3 less round trips in the regen.

The results of this experiment suggest that the GVD profile changes by large amounts over the spectrum of the compressed pulse. Specifically, a maximum in the GVD was seen between 790 nm and 800 nm and between 810 nm and 815nm.

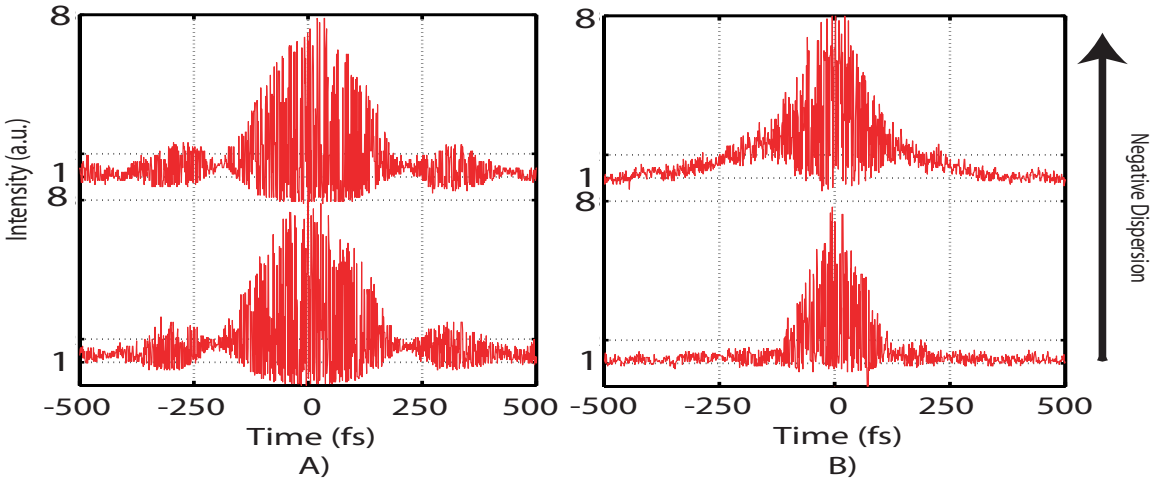

Figure 7.9: IAC traces for different numbers of round trips in the regen where the central wavelength is, A) 800nm and the pulse is positively chirped, and B) 775nm and the pulse is negatively chirped.

7.3.2 Ambiguity of the sign of the GVD

In a next step the total positive dispersion was increased by inserting prism pair P34 by 3mm (for more positive dispersion) and adding a round trip in the regen (for a total of 21). The GVD profile was then mapped similarly to the previous experiment. However, at this point the width of the spectral slices used was reduced to $10nm$ in order to provide a higher resolution.

In an effort to determine the sign of the GVD, for a given spectral slice, IAC traces for different numbers of round trips in the regen were compared to determine whether increasing positive, or increasing negative, dispersion brought the phase over the spectral slice closer to transform limit (note that this method is best used for pulses with GVD profiles not within the error limitations of the experiment away from transform limit).

For the given setup, checks of the sign of the GVD were performed at, 775nm and 800nm, and the results of each check for 19 and 21 round trips are shown in figure 7.9. As a result of this, it was determined that the value of the GVD at 775nm was $\sim -10^4 fs^2$ and $\sim \pm 3X10^3 fs^2$ for 19 and 21 round trips in the regen, respectively. For 800nm it was determined that the value of the GVD was $\sim 6X10^3 fs^2$ and $\sim 8X10^3 fs^2$ for 19 and 21 round trips in the regen, respectively.

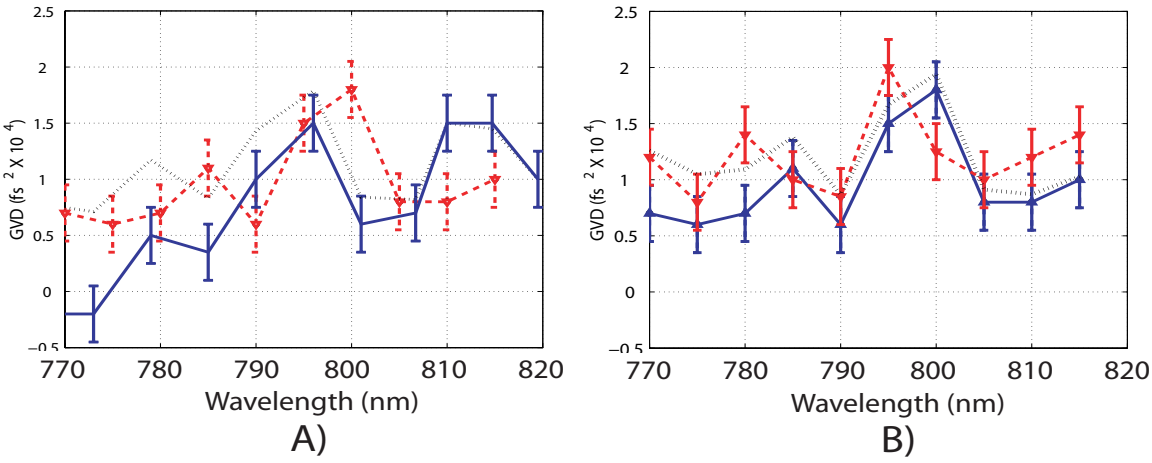

Figure 7.10: Comparison of mapped GVD data sets for; A) 40 (solid line), 64 (dashed line), The expected result for 64 (dotted line), reflections off TOD mirrors, and B) 64 (solid line), 78 (dashed line), The expected result for 78 (dotted line), reflections off TOD mirrors

7.3.3 Addition of TOD Mirror Reflections

In order to correct for an observed positive slope in the GVD from 775 to 800nm (as shown in figure 7.8, dashed line) TOD mirror reflections were added. First, 24 reflections off TOD mirrors were added (for a total of 64) and the effects determined by mapping the GVD profile. After adding the TOD mirror reflections the sign of the GVD at both 775nm and 800nm was checked and determined to be positive in both cases. The results of the GVD mapping experiment are shown in figure 7.10A and compared to the results of the previous experiment in which 40 reflections off TOD mirrors took place.

The results of this experiment indicated that $\sim$ 14 more TOD reflections were required to level the slope of the GVD curve. The sign of the GVD was checked both at 775 and 800 nm and was determined to be positive in both cases. This was done and the GVD curve was mapped as shown in figure 7.10B.

It is noted that the GVD at 790nm changed oppositely to what was expected for the first case (40 to 64 TOD reflections). Whereas the GVD at 790nm changed nearly as expected in the second case (64 to 78 TOD reflections). This was investigated further in the next set of experiments.

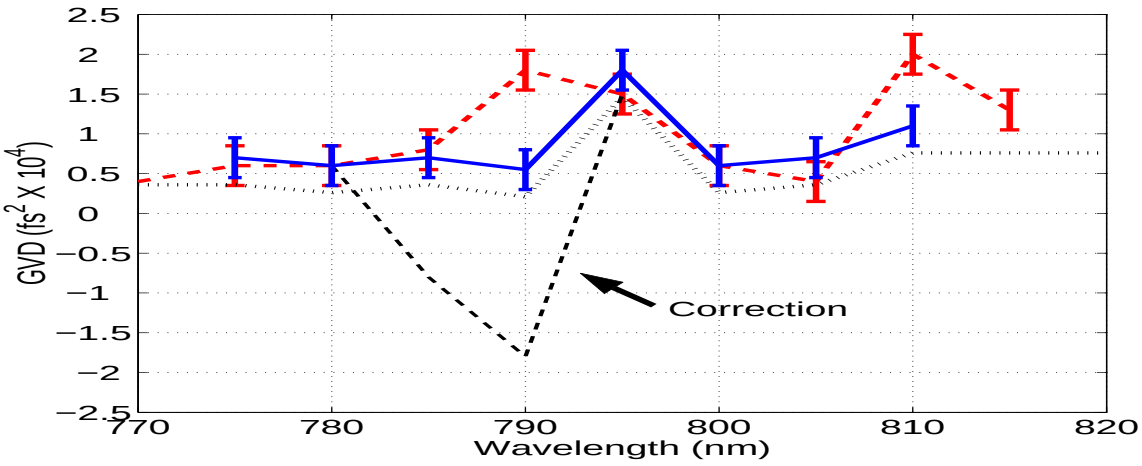

Figure 7.11: Comparison of mapped GVD data for 20 round trips in the regen (solid line) and 18 (dashed line) round trips in the regen (with an addition of $\sim 4mm$ of insertion of prism pair P34 to increase the positive GVD). The expected change using the results of the first case (thin dotted line) presents a reasonable match with the measured value except at $790nm$ and $810nm$. A correction to the sign of the GVD ,centered at 790nm, is indicated by the arrow.

7.3.4 Correction of Positive Dispersion

Moving towards compressing the pulses, some of the positive dispersion apparent in figure 7.10 was corrected for by inserting prism pair P34 by $3mm$ to increase the negative dispersion of the prism compressor system. A GVD profile for the compressed pulses under these conditions indicated that a mean positive dispersion of $\sim 7X10^3 fs^2$ remained. This was partially compensated for by reducing the number of round trips in the regen by 2 (simulated change of $-6X10^3 fs^2$) such that the remaining negative dispersion could be compensated for by subsequent insertion of prism pair P34. The results for mapped GVD profile for a change of 2 round trips in the regen are shown in figure 7.11.

As the expected results varied by a significant amount, at central wavelengths of 790nm and 810nm, the sign of the GVD was next checked at 780nm, 790nm and 815nm. The results indicated that the sign of the dispersion at 790nm was negative while positive at both 780nm and 815nm. IAC traces against round trips in the regen for 780nm, 790nm and 815nm are shown in figures 7.12A, 7.12B and 7.12C, respectively. A proposed correction to the measured GVD profile, using the negative sign of the dispersion at 790nm, is show in figure 7.11. The results indicated the presence of significant higher order phase, or oscillations in the GVD profile.

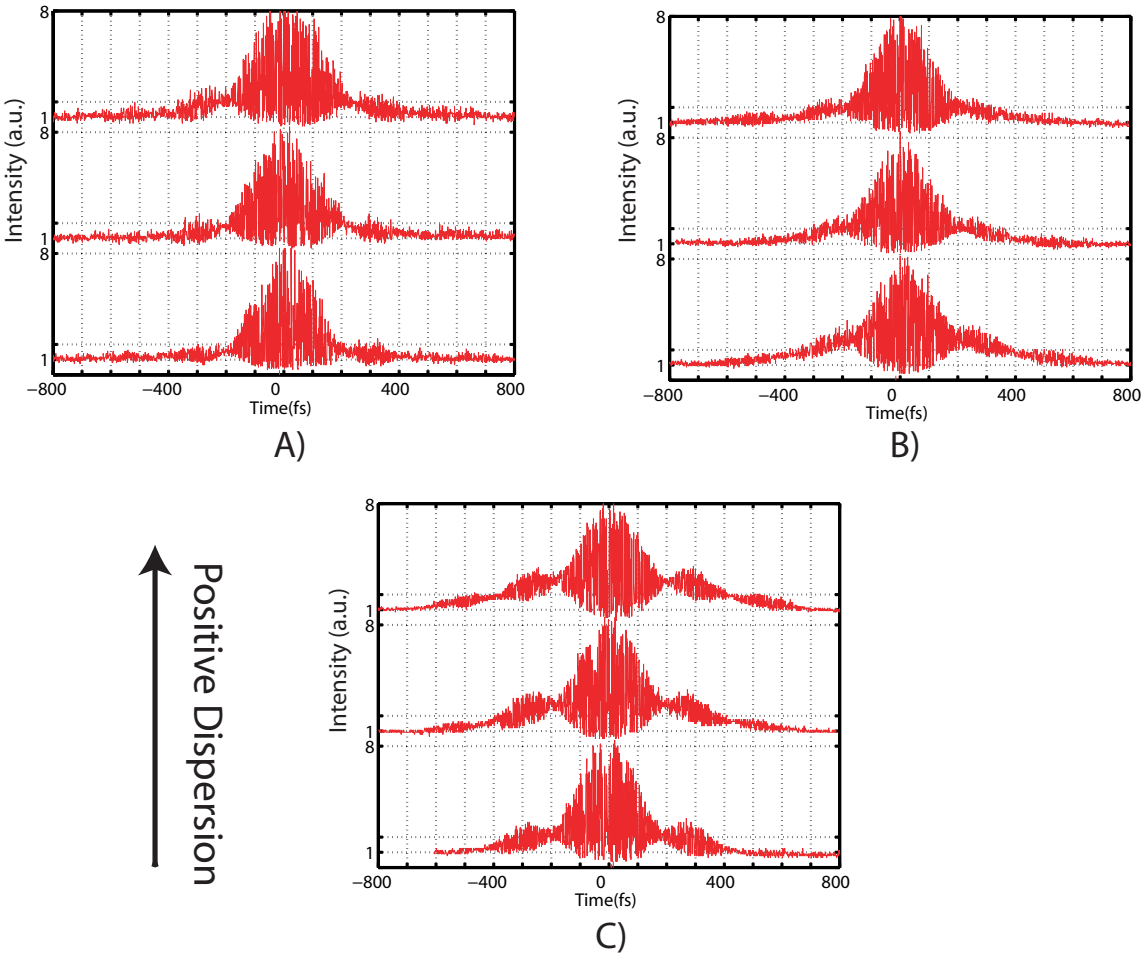

Figure 7.12: IAC traces for spectral slices at a central wavelength of; A) 780nm, B) 790nm and C) 815nm. Where in each case the pulse makes 18 (bottom), 19 (middle) and 20 (top) round trips in the regen. The IAC traces show that for the sign of the GVD at central wavelengths of 780nm and 815nm is positive and negative at a central wavelength of 790nm

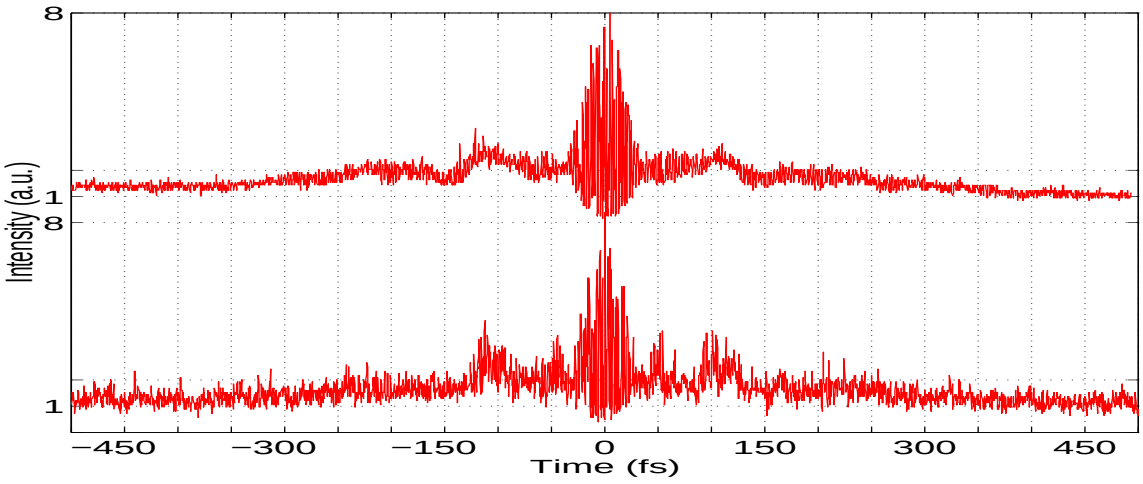

Figure 7.13: Measured IAC traces for pulses taking 19 round trips in the regen with output powers of $330\mu J$ (top) and $60\mu J$ (bottom). The similarities between the traces suggests that changes in the GVD profile with increases in the peak intensity inside the amplifier are negligible.

7.3.5 Investigation of Non-linear Effects

At this point, in order to determine if subsequent reductions in the number of round trips in the regen was causing the GVD profile to be altered, two IAC traces were taken at different pump powers. For each IAC trace the pulses made 18 trips in the regen. The average energy of the pulses out of the regen was measured to be $330\mu J$ and $60\mu J$ for the two different pump powers. With an output energy of $60\mu J$ the B-integral is well below 1 which suggests that non-linear effects due to the intensity of the pulse in the amplifier would not take place.

The IAC trace for the case of low pump power was seen to have a higher noise level than that of the case of higher pump power. This can be understood in terms of the level of amplification for each case. For the higher pump power, the pulses are switched out of the regen at peak gain and hence exhibit minimal shot to shot power fluctuations. For the case of lower pump power, many more round trips in the regen would be required to reach optimal gain, thus for a low number of round trips in the regen peak gain is not reached and shot to shot power fluctuations are expected as the gain achieved by the pulses on a shot to shot basis varies.

The results of the experiment are shown in figure 7.13. The similarities between the IAC traces suggest that non-linear effects due to the intensity of the pulse in the amplifier, with an output energy of $330\mu J$, are negligible.

In light of the results of the test for non-linear effects in the regen and the GVD mappings it was thought that a localized anomaly such as damage or surface deformation on an optic in the prism compressor may be responsible for the unex-

pected oscillations in the GVD profile. This was thought possible because of the spatial separation between frequencies that exist in the compressor. However inspection of the optics in the prism compressor revealed no obvious damage, and cleaning and laterally shifting the the optics had no noticeable effect on the IAC traces of pulses out of the compressor.

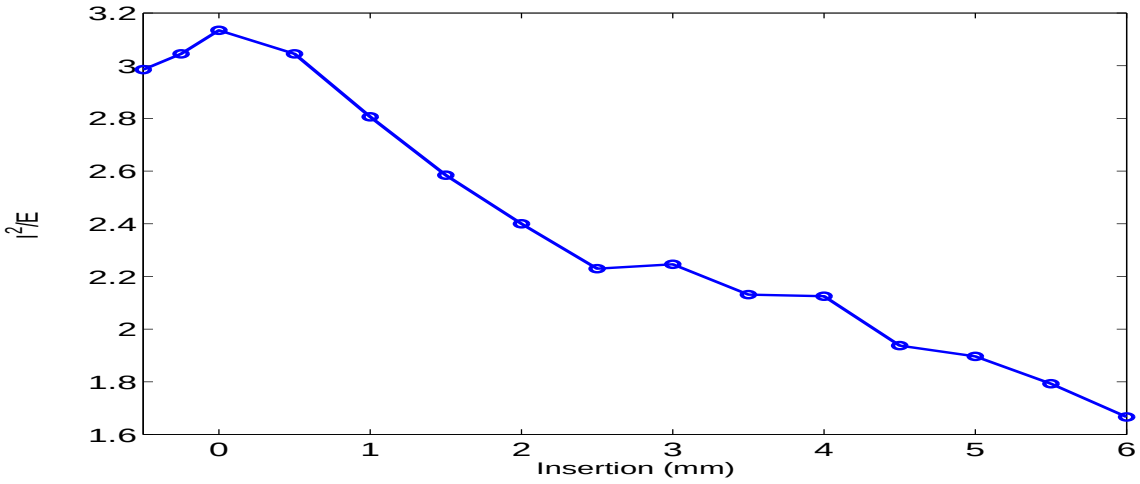

Figure 7.14: Ratio of I^2 to pulse energy, E, against prism pair insertion. The peak at position 0 indicates a region of maximum compression.

7.3.6 Compression Optimization

By maximizing the ratio between intensity squared and pulse energy the overall pulse intensity can be maximized, as discussed in section 6.4. Figure 7.14 shows the change in the ratio of intensity squared to pulse energy as a function of prism pair insertion.

In an attempt to optimize compression the intensity of pulses out of the compressor were optimized by adjusting the prism insertion while monitoring the signal from the 2-photon diode using the 'ACScan.vi' program. With compression optimized the GVD profile was mapped and checks of the sign of the GVD at each center wavelength were performed. The mapped GVD profile is shown in figure 7.15.

A 12th order polynomial (shown in figure 7.15 was then fit to the mapped GVD profile in order to simulate the expected IAC trace for a pulse with the given GVD profile. The simulated pulse shape for such a GVD profile and measured spectrum is shown in figure 7.16. The simulated IAC trace based on the pulse shape is compared to the measured IAC trace in figure 7.17.

The closeness of the two IAC traces suggests that the measured GVD profile is close to the actual profile of the compressed pulses. It is noted that the discrepancy between the exact placement of the features in the IAC trace may be due to discrepancies between the fit GVD profile and the actual GVD profile. A dc offset of the central GVD results in a broadening of the pulse which results in the features in the IAC to spread out from the center. For example, the IAC trace in figure 7.13, where the pulse is more dispersed, shows similar features to that of the IAC trace in figure 7.17 with the exception of their placement from the central peak.

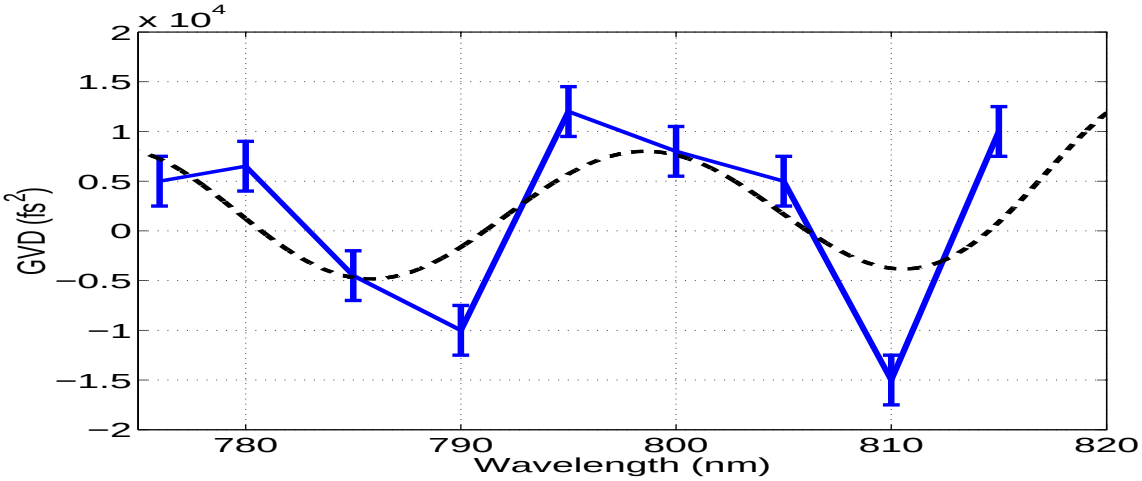

Figure 7.15: The mapped GVD profile after optimizing I^2 (solid line), and a 12th order polynomial fit to the GVD curve (dashed line).

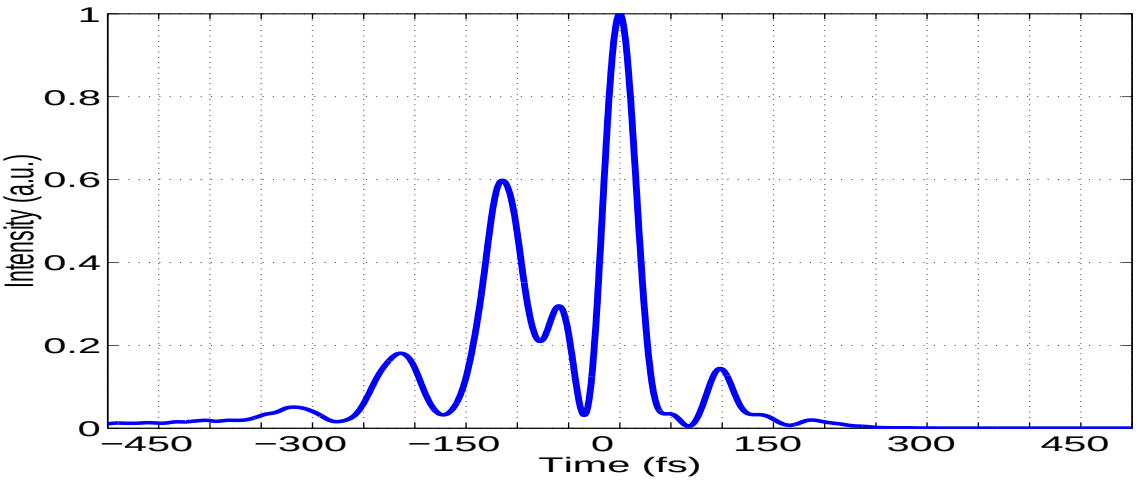

Figure 7.16: Simulated pulse shape using a 12th order polynomial fit to the GVD mapped in figure 7.15

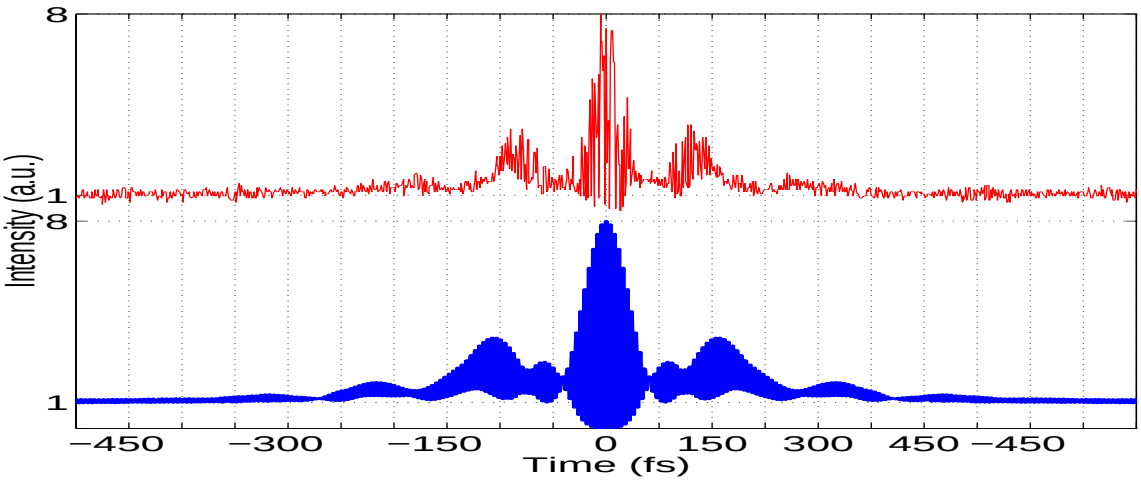

Figure 7.17: A measured IAC trace performed after optimizing the compression (top) and a simulated IAC trace using the 12th order polynomial fit to the mapped GVD profile in figure 7.15(bottom)

7.4 SPIDER Results

In an attempt to fully characterize the pulses out of the compressor, the SPIDER system described in section 6.4.3 was next utilized.

For this experiment the spectrum of the compressed pulses was made to be as broad as possible by optimizing the etalons in the amplifier and is shown in figure 7.18. Before performing the SPIDER trace the intensity of the compressed pulses was optimized as described in the previous section.

To provide enough phase-matching bandwidth a 20μm Type-II BBO crystal cut at an angle of 42.4^o was used in the SPIDER.

The up-converted spectrum for the sheared and non-sheared pulses was measured sequentially in order to measure the spectral shear, shown in figure 7.18. Each up-converted spectrum contained unexpected oscillations. The features in each up-converted spectrum matched fairly well, with the exception of a few anomalies (as indicated in the figure). A subsequent Fourier transform of each up-converted spectrum did not reveal any temporal features.

The frequency of up-conversion was determined to be 364THz (824nm), by matching the central frequency of the non-sheared up-converted spectrum with the central frequency of the pulses into the SPIDER, determined in a separate measurement. Rotation of the non-linear crystal to change the phase-matching angle did not result in any other frequencies being up-converted. This shows that essentially the entire spectrum of the pulses into the SPIDER were up-converted.

A SPIDER trace was taken by averaging 200 spectrometer shots with an inte-

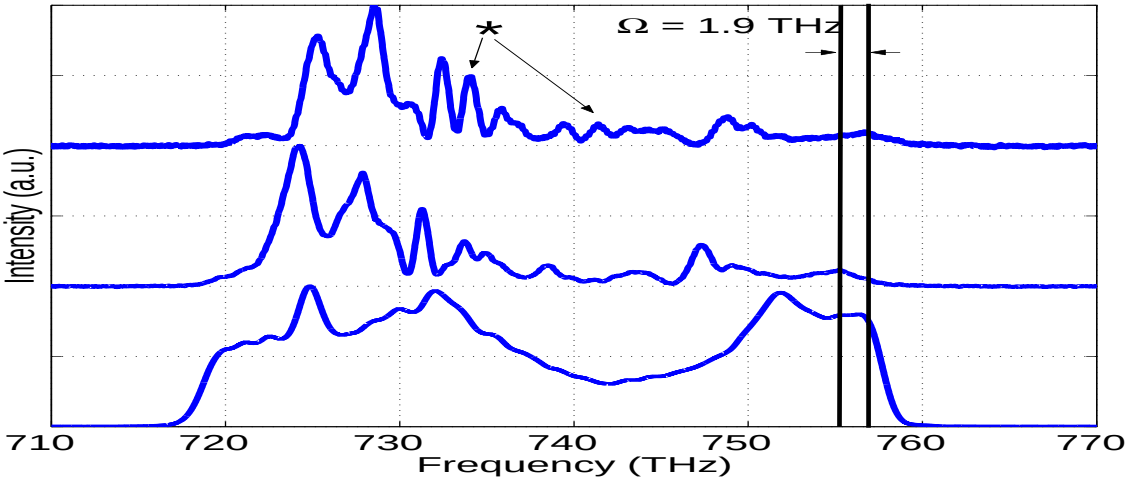

Figure 7.18: The up-converted spectra from the SPIDER (top and middle) showing a frequency difference of Ω. The spectrum of the compressed pulses at the up-conversion frequency of 364THz is also shown (bottom) and fits well to the middle trace. Features that do not match between the up-converted spectra are signified by a $*$.

gration time of $300ms$ each. The recorded SPIDER trace is shown in figure 7.19. The group delay was calibrated by recording the spectrum of the remaining unconverted light of the pulse replicas with an IR spectrometer, after the pulses had passed through the BBO crystal. In this way, systematic errors accrued during the group delay calibration due to turning the pulse replicas before the BBO crystal, as described in section 6.4.3, could be avoided. The calibrated value for the group delay was determined to be $268fs$ by examining a Fourier transform of the calibration trace, similarly to the procedure described in section 6.4.3.

The SPIDER trace was analyzed using a program written in the MatLab programming language called $SPIDER.m$. In order to remove any effects that the oscillations in the up-converted spectra might have on the ability of SPIDER to reconstruct the phase of the pulse, the Fourier transform of each up-converted spectrum was removed from the Fourier transform of the SPIDER trace. This was seen to have little effect on the recovered phase, indicating that the observed oscillation in the up-converted spectra may not have significantly effected the SPIDER interferogram.

The recovered phase difference from the SPIDER inversion and filtering algorithm was concatenated to return the phase of the compressed pulses (explained in section 6.4.3). The phase profile retrieved from the concatonation routine is shown in figure 7.20

The pulse shape corresponding to the phase retrieved by SPIDER and the mea-

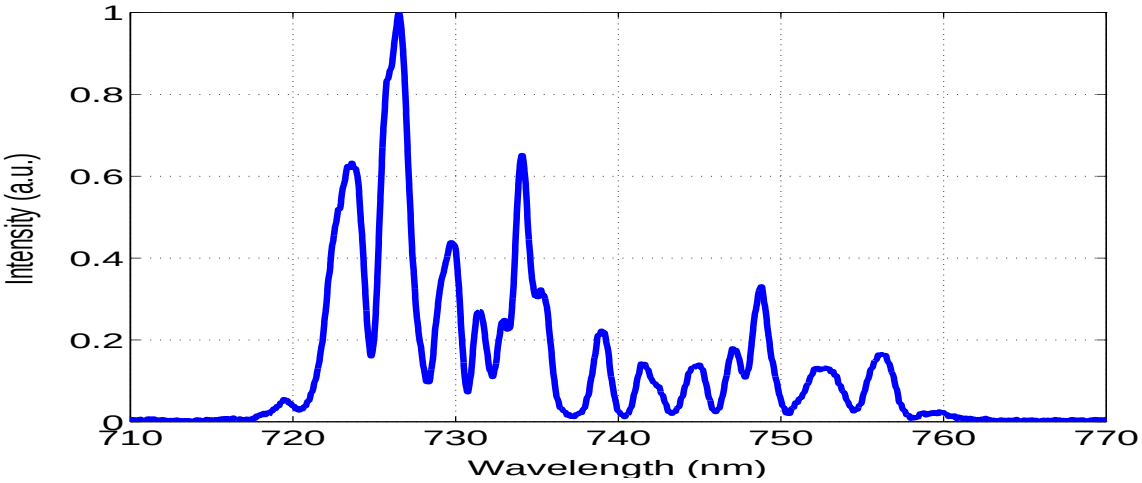

Figure 7.19: The SPIDER trace taken of the compressed pulses

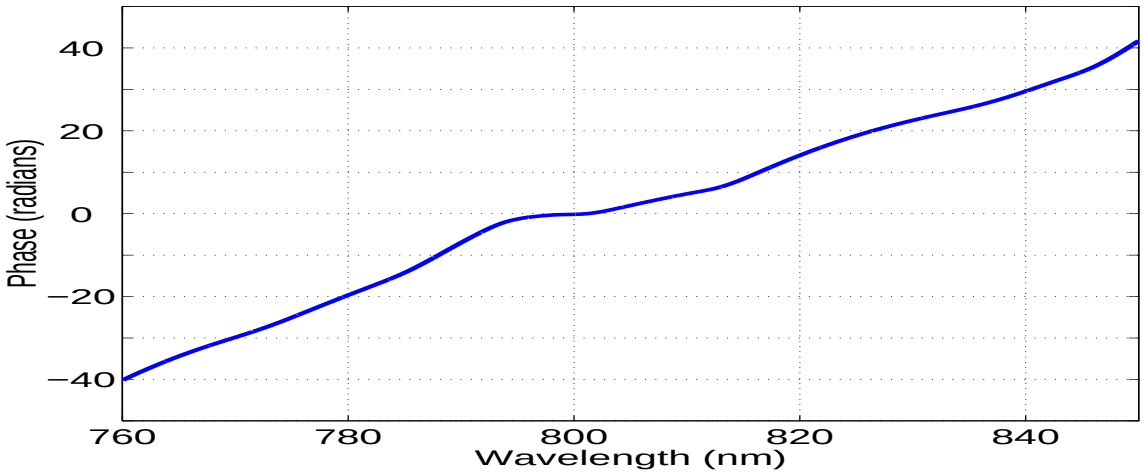

Figure 7.20: The phase of the pulse recovered from the SPIDER trace

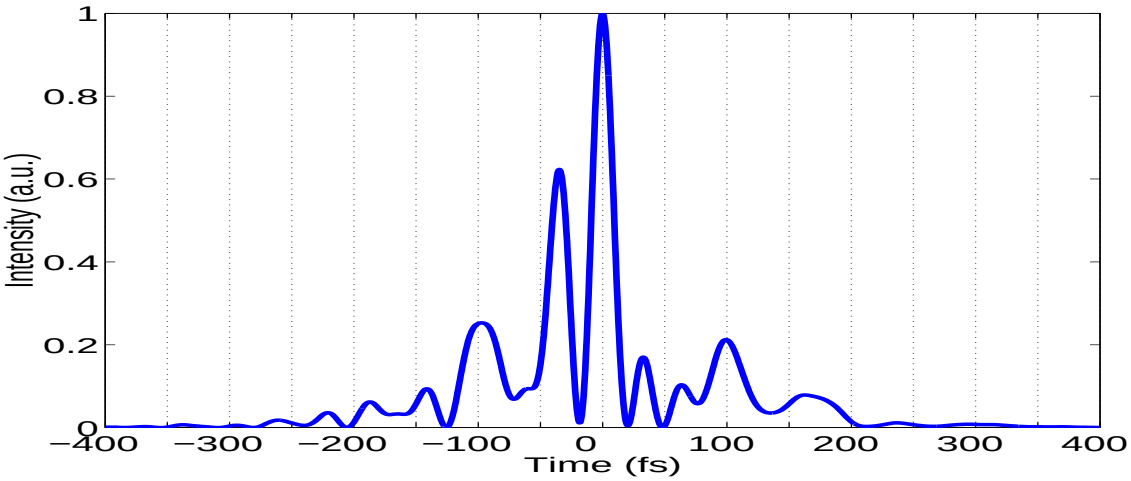

Figure 7.21: The corresponding pulse shape using the measured spectrum and recovered phase from the SPIDER.

sured spectrum is shown in figure 7.21. Using the simulated pulse shape, an IAC trace was simulated in order that it could be compared with a measured IAC trace, taken with pulses experiencing the same compression conditions as the pulses measured with SPIDER. The results are shown in figure 7.22. The right hand side of the measured IAC trace matches well with the simulated IAC trace. A peak on the left hand side of the measured IAC trace has been wiped out, it is thought, due to shot to shot fluctuations in the laser.

7.4.1 Discrepancy With Simulation

The discrepancy in the system simulation was determined by subtracting the GVD profile calculated using the recovered phase by SPIDER and subtracting the simulated dispersion for the regen and compressor given the setup of both systems when the SPIDER trace was taken. The GVD profiles for each case is shown in figure 7.23.

The difference between the two traces indicates a difference of $\sim 2.2X10^4 fs^2$ at $800nm$.

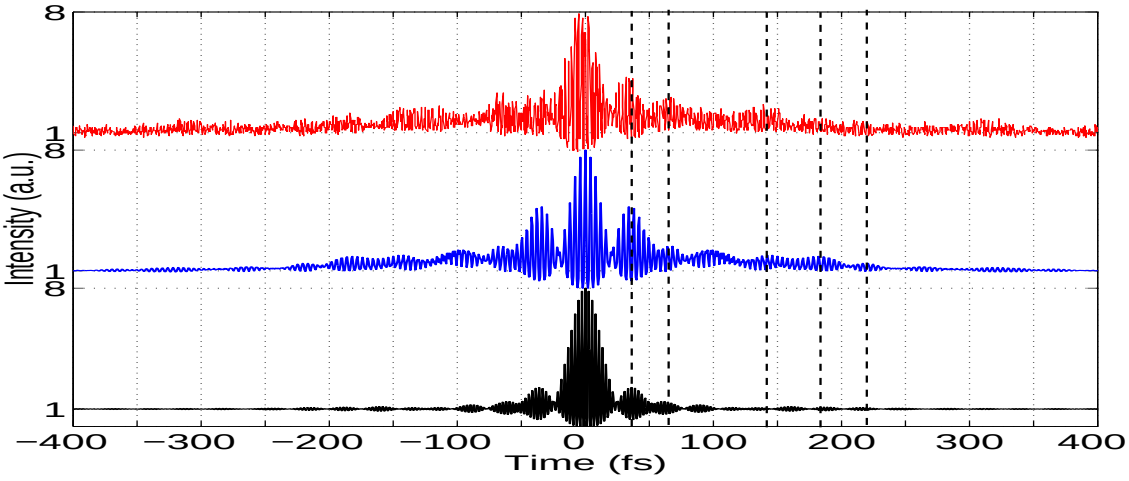

Figure 7.22: Comparison of; a measured IAC trace (top), a simulated IAC trace using the SPIDER result of figure 7.21 (middle), and a simulated IAC trace for a bandwidth limited pulse using the measured spectrum (bottom). Vertical guidelines have been added, where appropriate to point out significant matches between the simulated and measured IAC traces.

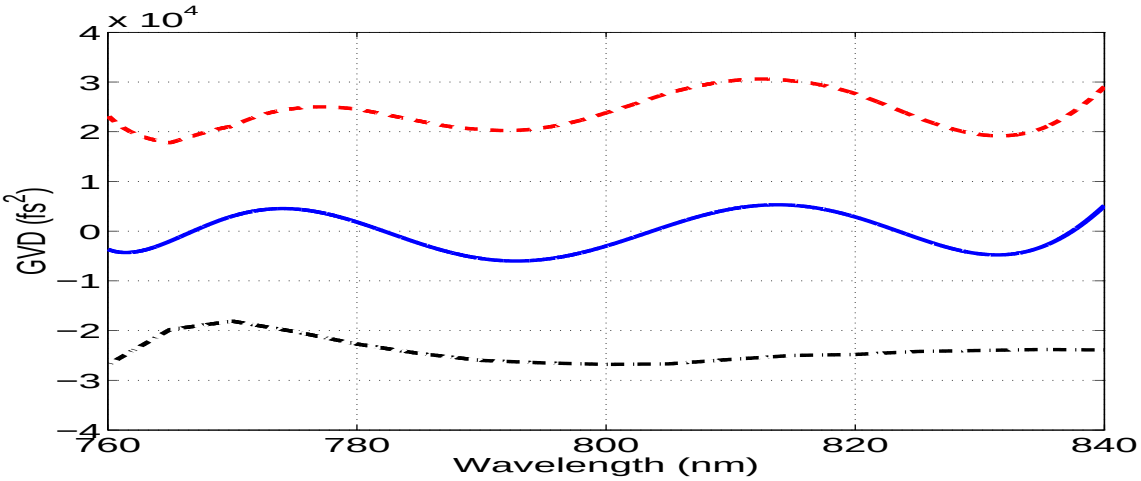

Figure 7.23: The GVD profile using the phase recovered by SPIDER (solid line) shown with the system simulation based on the regen and compressor setup at the time the SPIDER trace was taken (dash-dot line) and the difference between the two (dashed line).

Chapter 8

Conclusions and Discussion

8.1 System Modeling

Several computer models were used to simulate the design and arrangement of the laser system. Firstly, Winlase provided the regen geometry necessary to provide stability and mode size in the amplification medium. Further modeling of the laser cavity could include the effects of thermal lensing by adding an appropriate intra-cavity lens to the cavity model.

Using the laser cavity model, the laser system was shown to be capable of amplifying seed pulses by a factor of $\sim 3X10^6$. The beam-profile of amplified pulses emitted from the regen was measured and shown to be near Gaussian.

'SimTrans.m' was used to successfully model the spectral transfer function, including the effects of gain narrowing and spectral filtering on the bandwidth of amplified pulses produced by the regen. By modeling the technique of regenerative pulse shaping [29] it was shown that the regen was capable of generating enough amplified bandwidth to produce $\sim 16fs$ FWHM transform limited pulses.

The pulse width simulation, 'PulseSim.m', was used in combination with the 'DispRegenElements.m' simulation, of the dispersion of the amplifier system, to model the width of pulses inside the regen cavity. The intensity of amplified pulses within the regen cavity was estimated by measuring the energy of pulses emitted from the amplifier system and accounting for losses induced during emission from the regen. These results were used to calculate the B-integral of the amplifier system which was determined to be 2.3, below the maximum suggested value of 3 suggested in [16].

By integrating the model of the amplifier system dispersion into a model, 'PrismComp.xmcd', of the dispersive properties of a double prism compressor, the configuration of the system producing optimal dispersion compensation was determined. It was determined, from the model, in combination with the pulse width simulation, 'PulseSim.m', that for 50 reflections on TOD mirrors, 23 round trips in the regen and a prism compressor separation of 2 meters, that $< 30fs$ pulses could

be produced when a bandwidth of $62nm$ FWHM was supplied by the amplifier.

The performance of these programs has been very satisfactory. The discrepancy between predicted compressor geometry and the experimentally determined value is likely to be due to a combination of factors. For example, the lack of availability of detailed refractive index data for some of the proprietary system components, such as the Pockels cell and Faraday rotator. In future experiments the ability of the simulations used to determine the width of pulses in the regen could be estimated by performing a cross correlation on pulses emerging from the regen.

8.2 Pulse Characterization

An IAC, including a 2-photon diode, was built, with the capability of measuring pulses as short as $5fs$. The IAC was used to measure short ($\sim 15fs$), low energy ($\sim 3nJ$) pulses out of the oscillator system. The operation of the device was verified by measuring IAC traces for oscillator pulses dispersed in different material and showing that simulated IAC traces, using the 'ACIntf.m' simulation, based on an initial guess for the phase of the pulse, with the addition of theoretical dispersions, agreed with the measured results to an acceptable level.

The effects of noise, the finite resolution of the detection system and errors in the calibration of the group delay were investigated using the 'SPIDERSim.m' simulation. It was found that SPIDER is very robust in the presence of noise, capable of returning the phase of a pulse accurately even with the addition of a 30% additive noise. The simulation suggested that sampling above 5 points per SPIDER fringe gave best results and that errors in the determination of the group delay resulted in a shift in the recovered GVD that was directly proportional to the error.

Using the results of the model a SPIDER system was built with the capability to fully characterize the electric field of pulses as short as $5fs$. An attempt to verify the operation of the device was made by measuring the phase of pulses out of the oscillator with different values of the group delay and for different amounts of dispersion. For each value of the group delay a slight trend in the phase of the pulses, dispersed by different material, was observed. However the exact value of the returned phase differed with each value of the group delay. The discrepancy between each trace may be due to the thick-crystal used for this experiment or a slight systematic error in determination of the group delay. This error could be eliminated by measuring the interference pattern between the pulse replicas after passing through the doubling crystal in order to remove any effects that turning the beam before the focusing mirror might have when calibrating the group delay (see section 6.4.3). In addition to this, the spectrum of up-converted pulses using the thin crystal was not perfect. Further work is required to determine the source of the oscillations.

8.3 Compression Experiments

A measure of success was achieved by attempting to map the GVD profile of the compressed pulses. It was found, that near transform limit, the sign of the GVD for a given spectral slice was difficult to determine. The experiments showed there was an oscillation in the GVD profile of the measured pulses. Subsequent simulation of IAC traces based on the mapped GVD profile and measured spectrum showed a similarity to the measured traces. Future experiments to map the GVD profile of compressed pulses should include a measured IAC for at least ± 2 round trips in the regen, for each spectral slice, in order to determine the sign of the GVD.

Characterization of the compressed pulses using the SPIDER technique revealed an oscillation in the GVD profile, similar to, although not exactly the same, as that determined by the GVD mapping experiments. A simulated IAC trace using the phase recovered from SPIDER and the measured spectrum, fit well with the measured IAC. The SPIDER result gives a fairly good idea of the shape of the compressed pulse and provides a phase profile with which to work. Successful operation of the SPIDER should be verified by stretching the compressed pulses with known dispersions and comparing the returned phases with theoretical values.

The results of both the GVD mapping and SPIDER experiments indicated the presence of higher order phase and, based on the model of the prism compressor ('PrismComp.xmcd'), more overall positive system dispersion than was determined by the model of the stretching components ('DispRegenElements.m'). Using the results of the SPIDER trace a discrepancy between the dispersion of the compressed pulses, for the given setup, and the modeled dispersion of the CPA system was determined to be $\sim 2.2X10^4 fs^2@800nm$.

IAC traces taken with low pump power, where the intensity inside the regen would be well below that required for SPM, showed very little difference from IAC traces taken with higher pump powers. As a result of this, non-linear phase shifts do not appear to be the cause of the residual higher order phase.

With successful operation of the SPIDER the source of the higher order phase should be determined. Specifically, it is suggested that the dispersion due to the TOD mirrors and intra-cavity etalons be determined by changing the number of reflections on the TOD mirrors, or the angles of the intra-etalons, and measuring the change in phase with SPIDER.

In order to correct for any residual higher order phase in the compressed pulses a deformable mirror could be introduced as suggested in [47]. In order to optimize the compressed pulse intensity a genetic algorithm, in conjunction with an appropriate feedback signal, could be used to control the deformable mirror.

In order to reduce the B-integral and the possibility of non-linear effects it is proposed that additional prisms could be inserted in the prism compressor to increase it's practical compression range.

Appendix A

Component Dispersions

A.1 Material Index Fits

Most transparent materials exhibit a concave index of refraction versus wavelength over the visible region of the spectrum suggesting that polynomials in $\lambda^{-}1$ are a superior choice when constructing mathematical fits to given index of refraction data. Where necessary different techniques were used to fit the index of refraction data with consideration being given to reference [48] where descriptions of multiple fitting techniques to index of refraction data is presented.

Reference [48] indicates that the introduction of artificial oscillations in the index of refraction fit are more likely to occur the larger the order of the fit. In addition, on reviewing the classical Lorentz-Lorenz dispersion equation, it would appear that oscillations in the index of refraction with wavelength would indicate a necessarily complicated structure. It is assumed therefore that index of refraction data should vary smoothly from one data point to the next and that any observed oscillatory behavior of the index of refraction against wavelength has indeed been introduced artificially. This was important to consider when fitting index of refraction data for the purpose of determining system dispersions as any artificial curvature of the index of refraction will introduce increasingly inaccurate values for material dispersion.

Coefficient –	Faraday Rotator M-18	Pockels Cell QX 1020	Faraday Rotator Polarizers (Calcite)	Fused Silica Windows	Ti:Sapp	SF57	Polarizing BS BK7
A	2.661529E-3	3.430182E-3	2.69705	6.961663E-1		3.2578496	2.2718929
B	-1.1005749E-2	-2.891340E-2	1.92064E-2	0.0684043		-1.4544868E-2	-1.010807E-2
C	4.158559E-2	9.919006E-2	1.820E-2	0.4079426		4.2028938E-2	1.0592509E-2
D	1.631705	-1.710058E-1	1.51624E-2	0.1162414		5.2295853E-3	2.08169E-4
E	-	1.605437E-1	-	8.974794E-1		-4.6931979E-4	-7.647253E-6
F	-	1.431263	-	9.896161		4.4359036E-5	4.92409E-7
Fit Type –	Polynomial ($\lambda^{-}3$)	Polynomial ($\lambda^{-}5$)	Sellmeier Type I	Sellmeier Type II	none	Schott	Schott

Table A.1: refractive index fits used for simulations

GVD (fs^2)	TOD (fs^3)	FOD (fs^4)
-1.92	70.65	-671.8

Table A.2: Dispersion per reflection from a HDTC mirror at normal incidence.

A.2 Reflective Component Dispersion

A.2.1 High Damage Threshold Cavity Mirrors

High damage threshold cavity (HDTC) mirrors were purchased from FemtoLasers inc. for use in the regen cavity. Femtolasers provided a plot of the HDTC mirror dispersion profile for normal incidence. The provided graph was digitized and fit to a 3th order polynomial for use in the dispersion simulations.

A.2.2 Extra-Cavity Beam Steering Mirrors

The majority of the extra-cavity beam steering mirrors used in the laser system before compression were Thorlabs BB1-E03 mirrors. The BB1-E03 mirror is a broadband dielectric coated mirror with high reflectance over the spectral region 700-900nm. The TOD imparted by the coating on these mirrors was quoted at approximately $\mathbf{48}fs^{\mathbf{3}}$ per reflection and the GVD negligible.

A.3 Other System Dispersion

The seed pulse goes through a small amount of material, other than the major system components that are described above, on it's way from the oscillator to the regen cavity. This includes the output coupler of the oscillator (5mm thick), the compensating wedge after the output coupler (5mm thick), the 1/2 wave plate just before the regen cavity ($5mm$ thick, 2 passes), 48 reflections off of dielectric mirrors (depending on configuration) and transmission through approximately 46 meters of air. The glass materials were assumed to be comprised of BK7 while the dispersion due to reflections from the mirrors was approximated from data given by Femtolasers inc. The dispersion due to air was obtained from [**?**].

Component	Length(mm)/ Num. Reflections	GVD (fs^2)	TOD (fs^3)	FOD (fs^4)
Material (BK7)	20	8.89E+02	6.46E+02	-1.97E+02
Mirrors	48	0	480	unknown
Totals		2.173E+03	1.126E+03	-1.97E+02

Table A.3: Other dispersion experienced by an amplified pulse

Appendix B

Mathematical Relationships

B.1 Whittaker-Shannon Sampling Theorem

The Whittaker-Shannon sampling theorem states that a continuous function which is non-zero over a finite span may be exactly reproduced, over that span, by any discrete counterpart function having a sampling rate equaling or exceeding the inverse width of the span.

B.2 Nyquist Sampling Theorem

Any bandlimited signal is limited by how fast it can change it's amplitude. In other words, an oscillating signal is limited in terms of how much information it can convey over a discrete moment of time. Sampling theory dictates that a complete representation of a bandlimited signal can be obtained if it is sampled at twice the rate that it has the ability to oscillate at. The necessary sampling rate is commonly referred to as the Nyquist frequency.

B.3 Jacobian Transformation

When transforming a function from one metric to another where the spacing is non constant a constant of proportionality needs to be introduced. The underlying reason for this is that under both metrics the integral of the function must necessarily be the same. Mathematically the transformation of a spectral amplitude, A_λ, from wavelength space to frequency space (A_f) can be represented as follows:

$$\int A_f d_f = \int A_\lambda d_\lambda \tag{B.1}$$

$$A_f = A_\lambda \frac{d_\lambda}{d_f} \tag{B.2}$$

where $\lambda = \frac{c}{f}$ and $\frac{d_\lambda}{d_f} = \frac{-c}{f^2} = \frac{-\lambda^2}{c}$ so that

$$A_f = \frac{-\lambda^2}{c} A_\lambda \tag{B.3}$$

B.4 The Fourier Transform

The Fourier transform maps a given function into a reciprocal space. A common Fourier transform performed in ultrafast optics is the mapping of a function of frequency $f_\omega(\omega)$ to a function of time $f_t(t)$. The symbol $\mathcal{F}$ denotes that a Fourier transform is to be performed.

$$\mathcal{F}[f_t(t)] = \frac{1}{\sqrt{2\pi}} \int_{-\infty}^{\infty} f_t(t) e^{-i\omega t} dt \tag{B.4}$$

The inverse Fourier transform is denoted by $\mathcal{F}^{-1}$.

$$\mathcal{F}^{-1}[f_\omega(\omega)] = \frac{1}{\sqrt{2\pi}} \int_{-\infty}^{\infty} f_\omega(\omega) e^{+i\omega t} d\omega = f_t(t) \tag{B.5}$$

$$\mathcal{F}[E(t)] = E(\omega) e^{i\phi(\omega)} \tag{B.6}$$

$\boldsymbol{\phi(\omega)}$ = spectral phase
$\boldsymbol{E}$ = field amplitude

The inverse transform can be applied to a transformed function to return it to the original basis. A Fourier transform induces no loss of information to a function and gives an exact description of a given function in reciprocal spaces. Often it is mathematically easier to work with a function in one space as opposed to the other making the Fourier transform a very powerful tool.

Appendix C

2-Photon Diode Circuit

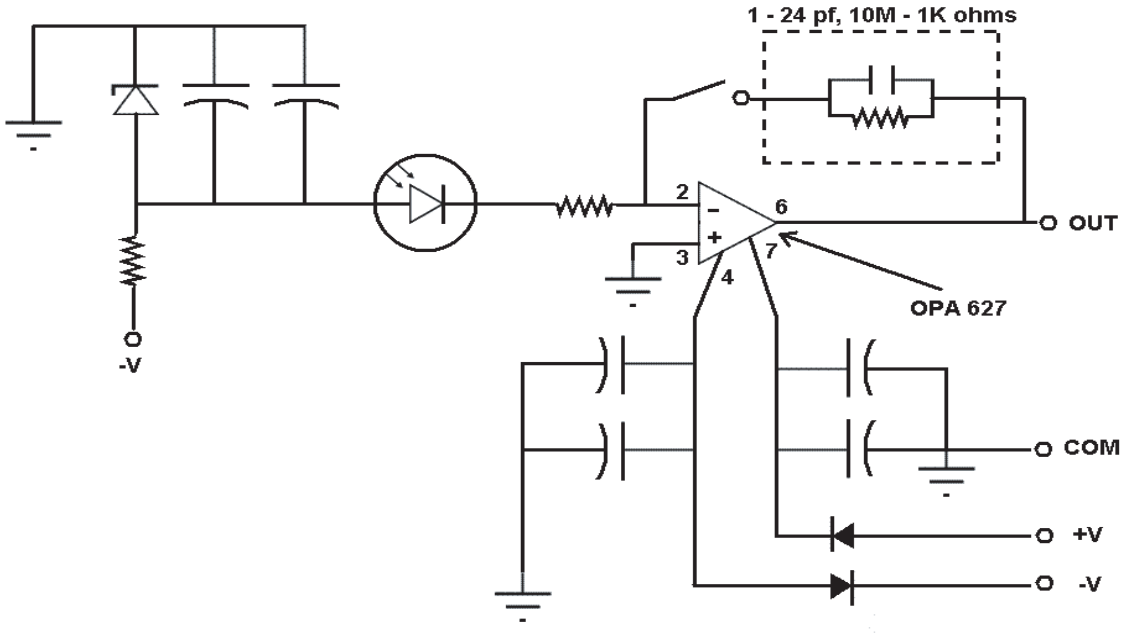

Figure C.1: The low noise amplification circuit used for the 2-photon diode. Because the gain affected the response time of the photodiode, a switch to provide variable gain was added in order that an optimal tradeoff between response time and gain could be determined.

References

[1] O. Svelto M. Nisoli, S. De Silvestri. *Appl. Phys. Lett.*, 68:2793, 1996.

[2] P. W. Dooly F. Quere A. D. Bandrauk D. M. Villeneuve P. B. Corkum F. Legare, I. V. Litvinjuk. *Phys. Rev. Lett.*, 91:093002–1, 2003.

[3] I. V. Litvinyuk P. W. Dooley S. S. Wesolowski P. R. Bunker P. Dombi F. Krausz A. D. Bandrauk D. M. Villeneuve P. B. Corkum F. Legare, K. F. Lee. *Phys. Rev. A*, 71:013415–1, 2005.

[4] U. Keller C. Vozzi M. Nisoli G. Sansone S. Stagira S. De Silvestri O. Svelto B. Shenkel, J. Biegert. *Optics Letters*, 28:1987–1989, 2003.

[5] G. Mourou D. Strickland. *Opt. Comm.*, 56:219–221, 1985.

[6] P. F. Moulton. *J. Opt. Soc. Am. B*, 3:125–133, 1986.

[7] A. Poppe M. Lenzner Ch. Spielmann F. Krausz A. Stingl K. Ferencz L. Xu, G. Tempea. *Applied Phys. B.*, 65:151, 1997.

[8] E. Riedle P. Baum, S. Lochbrunner. *Optics Letters*, 29:201, 2004.

[9] C. Le Blanc F. Raksi C. Rose-Petruck J. Squier K.R. Wilson V.V. Yakovlev K. Yamakawa C.P.J. Barty, T.Guo. *Optics Letters*, 21:219, 1996.

[10] S. Backus U. Russek M. Murnane-G. Mourou H. Kapteyn G. Vdovin E. Zeek, K. Maginnis. *Optics Letters*, 24:493, 1999.

[11] C. Spielmann Karpat Ferencz G. Tempea, F. Krausz. *IEEE J. Quantum. Electron.*, 4:193, 1998.

[12] I. A. Walmsley C. Iaconis. *IEEE J. Quantum. Electron.*, 35:501, 1999.

[13] D. J. Kane R. Trebino. *J. Opt. Soc. Am. A*, 10, 1993.

[14] M. Lenzner G. Tempea Ch. Spielmann-F. Krausz K. Ferencz S. Sartania, Z. Cheng. *Optics Letters*, 22:1562, 1997.

[15] F. Grasbon A. Dreischuh H. Walther F. Lindner, G. G. Paulus. *IEEE J. Quantum. Electron.*, page 1465, 2002.

[16] B. C. Stuart M. D. Perry, T. Ditmire. *Optics Letters*, 19:2149–2151, 1994.

[17] R. Trebino. *Frequency-Resolved Optical Gating: The Measurement of Ultrashort Laser Pulses*. Kluwer Academic, 2000.

[18] W. Rudolph J. C. Diels. *Ultrashort Laser Pulse Phenomena: Fundmentals, Techniques and applications on a fs Time Scale*. Academic Press, 1996.

[19] M. M. Murnane H. C. Kapteyn S. Backus, C. G. Durfee III. *Rev. of Sci. Insrum.*, 69:1207–1223, 1997.

[20] J. P. Gordon R. L. Fork, O. E. Martinez. *Optics Letters*, 9:150, 1984.

[21] R. E. Sherriff. *J. Opt. Soc. Am. B*, 15:1224, 1998.

[22] C. Speilmann F. Krausz R. Szipocs, K. Ferencz. *Optics Letters*, 19:201, 1994.

[23] O. Svelto. *Principles of Lasers, fourth edition*. Plenum Press, 1998.

[24] Yamakawa Matsuoka. *Jpn. J. Appl. Phys.*, 37:5997, 1998.

[25] A. J. Sabbah D. M. Riffe. *Rev. of Sci. Insrum.*, 69:3099–3102, 1998.

[26] C. Le Blanc F. Raksi C. Rose-Petruck J. Squier K.R. Wilson V.V. Yakovlev K. Yamakawa C.P.J. Barty, T.Guo. *Optics Letters*, 21:668, 1996.

[27] Y. Mimura Y. Iida H. Matsuura-D. Yoon O. Aso T. Yamamoto T. Toratani Y. Ono A. Yo K. Mizuno, Y. Nishi. *Furukawa Review*, 19, 2000.

[28] J-Y. Gau L. Sun J. Yu, S. Yuan. *J. Opt. Soc. Am. A*, 18:2153, 2001.

[29] S. Matsuoka H. Takuma C.P.J. Barty-D. Fittinghoff K. Yamakawa, M. Aoyama. *Optics Letters*, 23:525, 1998.

[30] M. J. Weber. *Handbook of Optical Materials*. CRC Press, 2003.

[31] Ch. Spielmann Z. Cheng, F. Krausz. *Opt. Comm.*, 201:145–155, 2002.

[32] I. C. McMichael F. Simoni J. C. Diels, J. J. Fontaine. *Applied Optics*, 24:1270, 1985.

[33] A. M. Weiner J-H. Chung. *IEEE J. Quantum. Electron.*, 7:656, 2001.

[34] I. A. Walmsley C. Iaconis. *Optics Letters*, 23:792–794, 1998.

[35] S.L. Cunha I.A. Heisler, R.R. Correia. *Applied Optics*, 44, 2005.

[36] J. Bromage C. Iaconis L. Waxer I. A. Walmsley T.M. Shuman, M.E. Anderson. *Optics Express*, 5:134–143, 1999.

[37] I.A. Walmsley C. Dorrer, P. Londero. *Optics Letters*, 26:1510, 2001.

[38] N. Karawa R. Morita H. Shigekawa M. Yamashita L. Li, S. Kusaka. *Jpn. J. Applied Phys.*, 40:L684, 2001.

[39] E. Riedle P. Baum, S. Lochbrunner. *Optics Letters*, 29:210, 2004.

[40] C. Le Blanc J.P. Rousseau S. Ranc P. Rousseau J.P. Chambaret F. Salin C. Dorrer, B. de Beauvoir. *Optics Letters*, 24:1644, 1999.

[41] I. A. Walmsley C. Dorrer, E. M. Kosik. *Optics Letters*, 27:548, 2002.

[42] A. Baltuska M. S. Pshenichnikov D. A. Wiersma J. K. Ranka, A. L. Gaeta. *Optics Letters*, 22:1344–1346, 1997.

[43] H. Yamada K. Naganuma, K. Mogi. *IEEE J. Quantum. Electron.*, 25:1225–1233, 1989.

[44] J. W. Goodman. *Introduction to Fourier Optics*. McGraw-Hill, 1988.

[45] E.M. Kosik I.A. Walmsley M.E. Anderson, L.E.E. de Araujo. *Applied Phys. B.*, 70:585, 2000.

[46] N. Matuschek G. Steinmeyer U. Keller L. Gallmann, D.H. Sutter. *Optics Letters*, 24:1314, 1999.

[47] M. M. Murnane H. C. Kapteyn S. Backus G. Vdovin E. Zeek, R. Bartels. *Optics Letters*, 25:587, 2000.

[48] C. J. Powell B. W. Morrissey. *Applied Optics*, 12:1588–1591, 1973.